WISEly Deconstructing the Great Andromeda Galaxy

Priscilla Chauke

May 20, 2014

University of Cape Town

Submitted in partial fulfillment of the degree M.Sc. in the Department of Astronomy

National Astrophysics and Space Science Programme
University of Cape Town

Supervisor: Prof. T.H. Jarrett

Abstract

A global photometric investigation of the M 31 system is presented using the Wide-field Infrared Survey Explorer (WISE), a survey which mapped the entire sky at mid-infrared wavelengths 3.4 μm (W1), 4.6 μm (W2), 12 μm (W3) and 22 μm (W4), as well as previous studies across the electromagnetic spectrum. While numerous surveys of the galaxy exist, very few cover its extended disk and greater halo that incorporates its globular clusters and rich satellite system. WISE observed the entire region of M 31, and with multi-wavelength data and measurements having recently become available for M 31, viz., GALEX in the ultraviolet, *Spitzer* in the mid and far-infrared and Herschel in the far-infrared, WISE plays a complementary role towards the comprehension of the fundamental processes of formation and evolution in galaxies.

A statistical classification scheme is developed to identify (and thereafter remove) the foreground Milky Way population from the WISE images, using WISE and 2MASS fluxes and colors, to obtain a clean measurement of the M 31 system. The scheme is tested using M 33, a smaller yet challenging galaxy, and is found to be an efficient method to trace the Galactic population (the results for this galaxy are, therefore, included). 104762 sources were identified as Milky Way, 70% of the total number of sources in a ~ 11 deg^2 elliptical area around the M31 region.

The WISE 1-σ integrated flux densities were measured to be 276 ± 3 Jy, 146 ± 2 Jy, 180 ± 2 Jy and 128 ± 2 Jy for the W1, W2, W3 and W4 bands, respectively. These measurements are $\sim$10% higher than their *Spitzer* counterparts. This is to be expected because WISE fully covers the M 31 region and extended M 31 emission, thereby allowing for adequate local background calculation. The stellar masses are estimated from the W1 and W2 measurements which efficiently trace most of the stellar host population. The M 31 stellar mass was found to be 8.7×10^{10} M$_\odot$, which compares well with recently published multi-wavelength analyses, and is about twice the stellar mass estimation for the Milky Way, although the considerable uncertainties in stellar mass estimates are comparable to the difference.

The WISE star-formation rates are derived using the W3 band, which is sensitive to polycyclic aromatic hydrocarbon emission arising from the more diffuse ISM, and the W4 band, which is sensitive to warm dust emission associated with dust-obscured massive star-formation regions. The star-formation rate estimates range between 0.3 and 0.7 $M_\odot$yr^{-1}, comparable to estimates from various previous studies.The specific star-formation rate estimated for M 31 ranges from 0.003 to 0.008 Gyr^{-1} and confirms its state of quiescence and passive evolution.

M 31 hosts a number of satellite galaxies and globular clusters (GCs). WISE is found to be useful in distinguishing candidate GCs from background galaxies. The W1 luminosity of GCs in the M 31 region ranges from 5.2×10^2 to 3.1×10^5 L$_\odot$, 0.3-150 times larger than the average B luminosity; and a W1-W2 color of -0.04 mag, within the range of extragalactic GCs. The median stellar mass was found to be 3.8×10^5M$_\odot$, about twice the average mass measured for Galactic GCs. Only the very bright (< -14 mag) and

large ($> 0.1^{\circ}$) satellite galaxies are resolved by WISE. Therefore, the photometric and characterization measurements of such satellites, viz., M 32, M110, NGC 0147 and NGC 0185, are presented. The data for these satellites are also cleaned of foreground sources. The integrated flux densities measured are comparable to *Spitzer* measurements that are available for these galaxies.

Acknowledgements

I would like to express my gratitude to my supervisor, Prof. T.H. Jarrett, who allowed me to undertake this investigation. He was extremely helpful and patient throughout and I have learnt a great deal from his supervision and guidance. I thank the SA SKA Project Scholarship Programme administrators for funding my MSc education. They have supported me since my second year of university and I am very grateful. I would also like to thank the National Astrophysics and Space Science Programme administrators for allowing this project to be available. Lastly, I thank my family for their love, support and encouragement.

Plagiarism Declaration

I, Priscilla Chauke, know the meaning of plagiarism and declare that all of the work in this document is my own, unless otherwise stated.

Contents

List of Figures

List of Tables

Chapter 1

Introduction

At a distance of 785 kpc (McConnachie et al., 2005), the Great Andromeda Galaxy (M 31) is the closest spiral galaxy to our own, and is the largest in the Local Group. As a result, it plays a significant role in the studies of extragalactic galaxies. Its similarity to the Milky Way, namely, its spiral structure, interstellar gas and dust, and globular and open clusters, makes it a principal laboratory for understanding spiral galaxies like our own. However, M 31 is more extensive and more luminous than our own galaxy; its halo is thought to be significantly larger and more diverse than that of the Milky Way (Ibata et al., 2001). It has significantly less star formation (Massey et al., 2007; Fuchs et al., 2009), suggesting a state of quiescence; and there is evidence to suggest it may be less massive (Gotteman et al., 2002), which would make the galaxy less dense than our own.

The M 31 system has been intensively studied for decades. The galaxy has been estimated to be a good template for a typical spiral galaxy, more so than the Milky Way, showing evidence of a typical history shaped mainly by recent merging (Hammer et al., 2007). Its proximity makes it the best target for very detailed observations of sources and structures (disk, star forming regions, etc.) present in other spiral galaxies, at high resolution that cannot be achieved for more distant galaxies. Its proximity also allows for global scale investigations of star formation and evolution of the entire galaxy to be made. This makes M 31 an ideal candidate to relate measurements for spiral galaxies at small scales ($\sim$ 1 pc) to those at global scales ($\sim$ 1 Mpc). The link between the scales allows for an inference of properties of more distant (spiral) galaxies and will lead to better understanding of the formation and evolution of spiral galaxies in the universe.

Although there have been numerous studies of the galaxy, due to its large angular extent, very few can address its global properties, map its entire star-forming disk or examine its local environment. This includes recent surveys, such as 2MASS, *Spitzer* and GALEX, that have surveyed the galaxy and subsequently mapped its disk; however, they do not cover the extended disk, or the greater halo that incorporates the Andromeda Group (globular clusters and rich satellite system). The Wide Field Infrared Survey Explorer

(WISE) has recently mapped the entire sky at mid-infrared bands 3.4 μm (W1) and 4.6 μm (W2), which trace the dominant (older) stellar mass content of galaxies, and 12 μm (W3) and 22 μm (W4), which trace the star formation regions. WISE has accordingly mapped the M 31 regions, including the local environment filled with satellite galaxies. Therefore, it is now possible to investigate the global properties of this captivating galaxy.

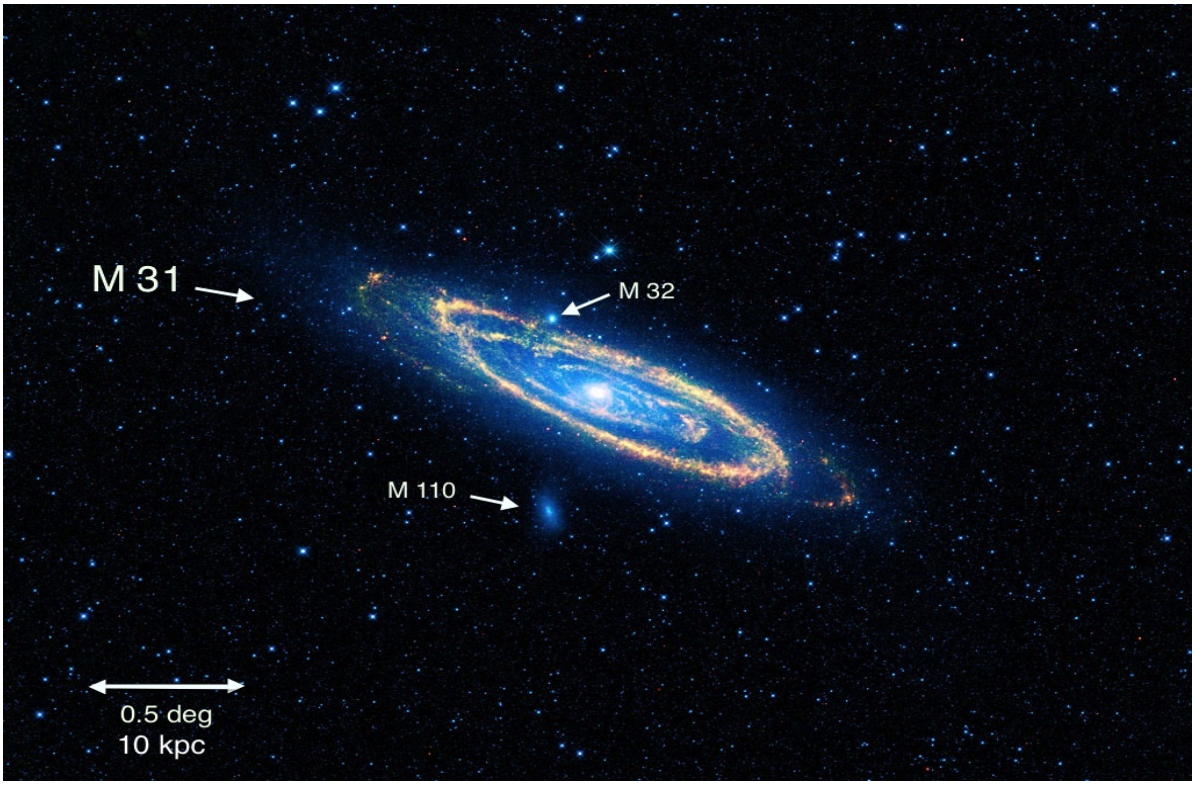

Figure 1.1: Combined WISE W1 (blue), W2 (green), and W3 (red) image of the M 31 region spanning 5°.

1.1 Motivation and Objectives of This Study

WISE imaging of M 31 covers the entire region of M 31, including its rich satellite system. This thesis aims to construct a multi-wavelength (ultraviolet to radio) catalogue of the global properties of M 31; and thus place the galaxy in the context of our understanding of galaxies in the the local universe. There have been other attempts from previous surveys to do so, however, WISE provides more of a complete picture in the mid-infrared.

Galaxies emit radiation across the electromagnetic spectrum. Therefore, to form a complete picture of their fundamental properties, such as the stellar mass, star formation rates, gas and dust content, data from multi-wavelength observations, from X-rays to radio, need to be combined. The main objective is to measure and characterize the

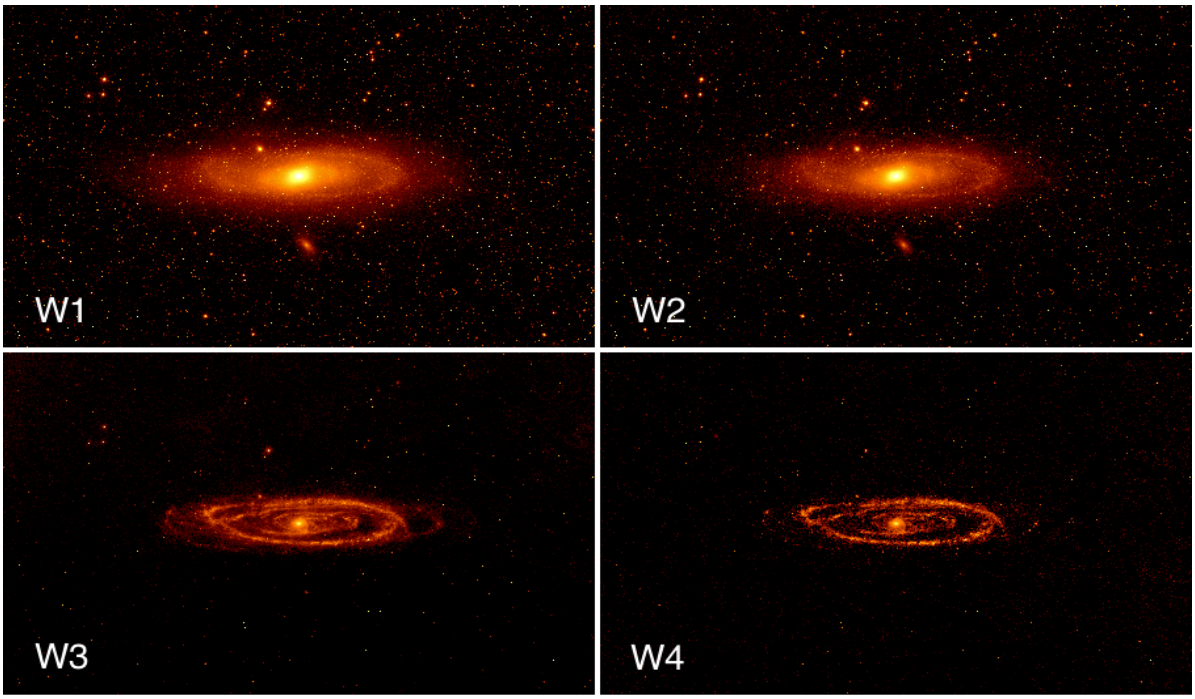

Figure 1.2: WISE W1 (3.4 μm), W2 (4.6 μm), W3 (12 μm) and W4 (22 μm) images of the M 31 region constructed using ICORE (Masci, 2013). Images are 6° across.

global surface brightness and photometric infrared properties of M 31, and its satellites, using high resolution reconstruction of WISE imaging. A multi-wavelength catalogue of the galaxy will then be constructed using the ultraviolet, near-infrared, far-infrared and radio properties obtained from previous studies. M 31's internal structures will also be deconstructed in order to investigate its star forming regions, disk and bulge populations, globular cluster populations and spiral arms.

Infrared emission (IR) from typical galaxies comes primarily from three sources: evolved stars, interstellar gas, and dust. Therefore, the infrared window is ideal for studying the stellar mass content and star formation history in galaxies, as it is sensitive to light from the dominant (evolved) stellar population (near-infrared), as well as star formation regions and the interstellar medium (mid-infrared). WISE allows for both the stellar population, using W1 (3.4 μm) and W2 (4.6 μm), and star-formation history, using W3 (12 μm) and W4 (22 μm), to be investigated. A combination of the W1 and W2 luminosities gives good measurements for the stellar mass distribution in galaxies, because the bands trace the evolved stellar population, that emits mostly in the 1-3 μ range, which constitutes most of the galaxy. The bands are relatively extinction free, with a constant W1-W2 colour independent of the age of the stellar population and mass function (Jarrett et al., 2011). It should be noted that the W2 band may contain excess emission from warm dust, e.g. from active galactic nuclei. This emission is small, therefore, it is assumed that all the emission in this band is photospheric. The stellar mass can be calculated using the WISE mass-to-light ratio (M/L) derived from Jarrett et al. (2013) and Cluver et al. (2014).

$$\log_{10}(M_{stellar}/L_{W1})(M_{\odot}/L_{\odot}) = -1.96(W1 - W2) - 0.03 \tag{1.1}$$

with

$$L_{W1}(L_{\odot}) = 10^{-0.4(M-M_{Sun})}$$

where M is the W1 absolute magnitude of the source, M_{Sun} = 3.24 mag, and W1-W2 reflects the rest-frame colour of the source. Hot young stars emit ultraviolet (UV) photons which are primarily absorbed by dust and re-radiated at longer wavelengths. The 12 μm band is sensitive to polycyclic aromatic hydrocarbon (PAH) emission arising from the photon-dominated regions (PDRs) located at the boundaries of HII regions and molecular clouds. The 22 μm band is sensitive to warm dust emission, excited by star formation, arising in the vicinity of hot HII regions. Therefore, these two bands are used to measure the global star formation rates (SFRs). However, the mid-infrared is sensitive only to the warm tracers of star formation, and thus only presents a lower limit to the total SFR which includes far-infrared emission. The best fit relations for the W3 and W4 SFRs, which were calibrated using *Spitzer* 24 μm photometry, were obtained by Jarrett et al. (2013), for SFRs in the range between 0 and 3, using the Rieke et al. (2009) relation:

$$WISE \quad W3 : SFR_{IR}(\pm 0.28)(M_{\odot}yr^{-1}) = 4.91(\pm 0.39) \times 10^{-10}\nu L_{12}(L_{\odot}), \tag{1.2}$$

$$WISE \quad W4 : SFR_{IR}(\pm 0.04)(M_{\odot}yr^{-1}) = 7.50(\pm 0.07) \times 10^{-10}\nu L_{22}(L_{\odot}) \tag{1.3}$$

where the Rieke relation for 24 μm photometry is

$$SFR_{24\mu m}(M_{\odot}yr^{-1}) = 7.8 \times 10^{-10}\nu L_{24}(L_{\odot}) \tag{1.4}$$

Extinction-corrected H_{α} SFRs were derived by Cluver et al. (2014) for the 12 and 22 μm WISE measurements using the best fits to the Galaxy And Mass Assembly (GAMA) sample distribution.

$$WISE \quad W3 : \log_{10} SFR_{H\alpha}(M_{\odot}yr^{-1}) = 1.13 \log_{10} \nu L_{W3}(L_{\odot}) - 10.24, \tag{1.5}$$

$$WISE \quad W4 : \log_{10} SFR_{H\alpha}(M_{\odot}yr^{-1}) = 0.82 \log_{10} \nu L_{W4}(L_{\odot}) - 7.3. \tag{1.6}$$

The IR SFR estimations trace star formation that is obscured by dust. The UV radiation from hot young stars that escapes absorption by dust allows the far-UV (FUV) and near-UV (NUV) bands also to be quantifiers of unobscured star formation in galaxies. The FUV and NUV SFRs, based on their respective luminosities, were derived by Buat et al. (2008) and Schiminovich et al. (2007). Combining the UV and IR SFR estimations provides a more complete characterization of the star formation that drives the evolution of disk galaxies. The method for combining UV, which contributes about 30% of the total, and IR estimates can be seen in Elbaz et al. (2007) and Buat et al. (2011).

$$FUV : \log_{10} SFR_{FUV}(M_{\odot} yr^{-1}) = \log_{10}(\nu L_{FUV}/L_{\odot}) - 9.69 \tag{1.7}$$

$$NUV : SFR_{NUV}(M_{\odot} yr^{-1}) = 10^{-28.165} L_{NUV}(ergs^{-1} Hz^{-1}). \tag{1.8}$$

Although telescopes like *Spitzer* have observed the galaxy, with better resolution, WISE was designed to map the entire sky, and thereby commands the entire region of the galaxy. The W1, W2, W3 and W4 bands make WISE a crucial instrument as it has the ability to both trace the stellar mass content of the galaxy, as well as its star formation processes. With multi-wavelength data and measurements having recently become available for M 31, in particular, GALEX UV observations (Gil de Paz et al., 2007), optical measurements (Tempel et al. 2010), *Herschel* observations (Fritz et al., 2012; Ford et al., 2013 and Viaene et al., 2014), and *Spitzer* Space Telescope observations (Montalto et al., 2009; Barmby et al., 2006; Gordon et al., 2006; etc.) in the infrared and far infrared, WISE will play a complementary role towards the comprehension of the fundamental processes of formation and evolution in (spiral) galaxies.

1.2 M 31 Surveys

To create a multi-wavelength catalogue for M 31 (see Table 1.1 for its basic parameters), the results obtained from this study will be compared and contrasted across the electromagnetic spectrum using ultraviolet, near-infrared, far-infrared, and radio data from previous studies. This will include photometric and surface brightness properties, as well as star formation rates and stellar mass measurements, in order to investigate the galaxy's past to present star formation history (Jarrett et al., 2013). An overview of previous M 31 surveys at different wavelengths is given below.

Table 1.1: Basic Parameters of M 31.

Parameter	Value
Right ascension (J2000) [a]	$00^h42^m44.4^s$
Declination (J2000) [a]	$+41°16'08''$
Distance (kpc) [b]	785 ± 25
Inclination [c]	77°
Position angle [c]	38°

References. [a] de Vaucouleurs et al. (1991), [b] McConnachie et al. (2005), [c] Walterbos and Kennicutt (1987).

1.2.1 X-ray Emission

X-ray observations provide information about high-energy phenomena such as the distribution of hot gas, black holes and supernova remnants. M 31 is an ideal target for detailed X-ray source population studies due to its proximity and moderate Galactic foreground absorption (Stark et al., 1992). Stiele et al. (2011) combined observations from the Deep XMM-Newton EPIC Survey of M 31, as well as archival XMM-Newton observations along the major axis in the 0.2-4.5 keV (XID) band (Pietsch et al., 2005; Di Stefano et al., 2002) which covered the entire D_{25} ellipse (Fig. 1.3). An X-ray catalogue of 1897 sources was created, 914 of which were detected for the first time, with a luminosity lower limit of $\sim 10^{35}$ erg s^{-1}. The faintest source has an XID band flux of 5.8×10^{-16} erg cm^{-2} s^{-1}; the brightest source has an XID Flux of 3.75×10^{-12} erg cm^{-2} s^{-1} and is located in the centre of M 31.

Fig. 1.3 shows the resultant combined exposure corrected EPIC PN, MOS 1 and MOS 2 RGB image of the Deep M 31 Survey including archival data; red represents the 0.2-1.0 keV band, green the 1.0-2.0 keV band, and blue the 2.0-12 keV band. The colour of the sources represents the class of X-ray; sources that are more red represent mainly supersoft sources (SSSs); yellowish sources represent supernova remnants (SNRs) and foreground stars; and blue (or white) sources represent background sources and X-ray binaries (XRBs). The distribution of the XID source fluxes is shown in Fig. 1.4. Revnivtsev et al. (2014) measured the total X-ray flux from M 31 in the 2-100 keV band using data from RXTE/PCA, INTEGRAL/ISGRI, and SWIFT/BAT space experiments. The total flux from the galaxy in the 2-20 keV and 20-100 keV bands were found to be $(9.1 \pm 0.9) \times 10^{-11}$ and $(7.00 \pm 0.96) \times 10^{-11}$ ergs^{-1}cm^{-2} respectively.

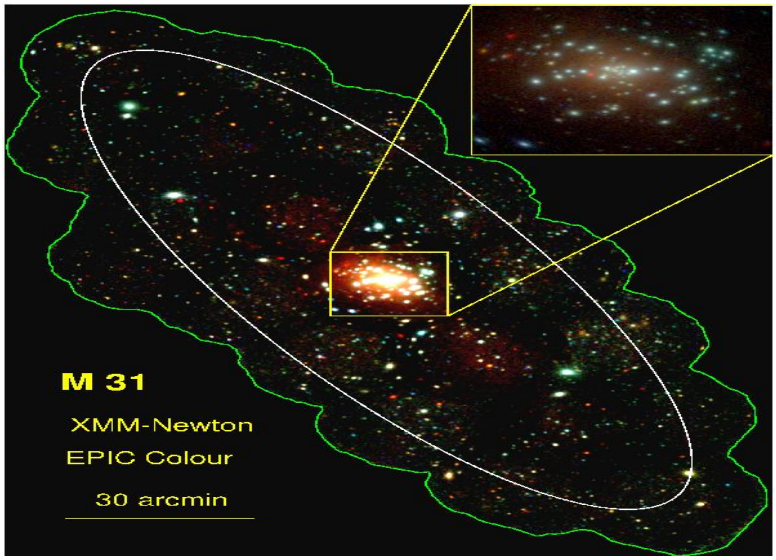

Figure 1.3: Combined EPIC PN, MOS 1 and MOS 2 RGB image of the Deep M 31 Survey including archival data (Stiele et al., 2011; see Sect. 1.2.1). The optical extent (D_{25}) is indicated by the white ellipse.

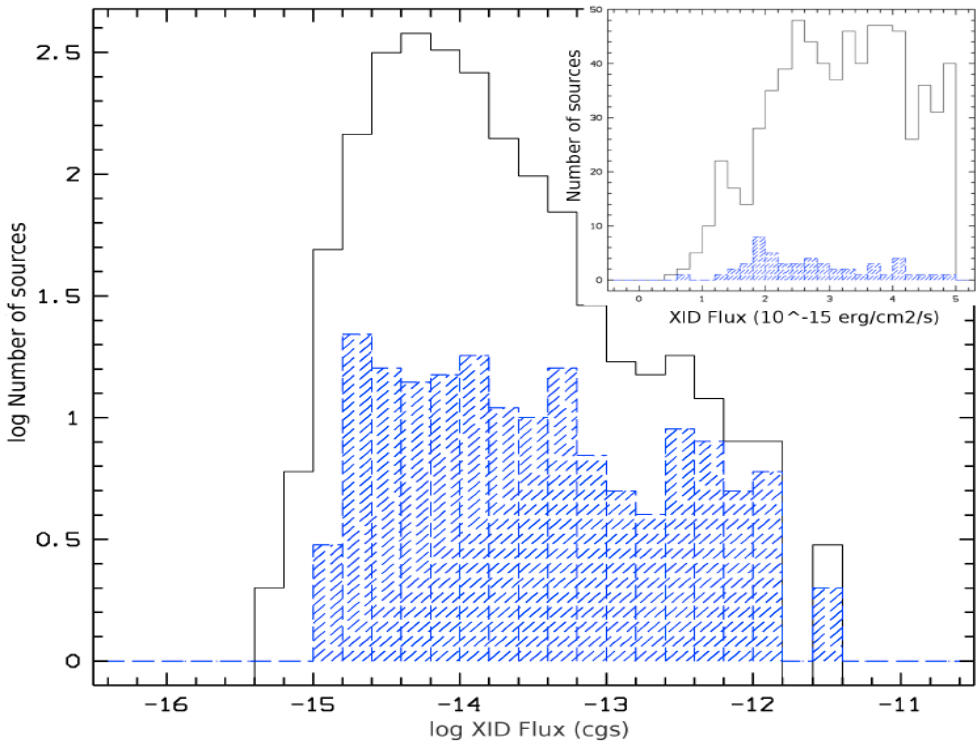

Figure 1.4: Distribution of the source fluxes in the 0.2-4.5 keV band (Stiele et al., 2011). The inlay shows the number of sources for fluxes lower than 5×10^{-15} erg cm^{-2} s^{-1}. The blue histogram gives the distribution of sources classified or identified as either SSSs, SNRs, XRBs or globular cluster sources.

1.2.2 Ultraviolet Emission

Ultraviolet flux is often used to trace and quantify recent star formation in nearby and distant galaxies. This is because young massive (O and B) stars emit powerful radiation in the ultraviolet. These stars are short-lived and form in associations in the galactic disk, therefore, they contribute to the global characteristics of their host galaxy at some particular period of the galaxy's evolution. UV imaging is ideal to characterize these stars, as they are confused with older stellar populations when observed at longer wavelengths.

Far and near-ultraviolet (FUV, 1516 $\mathring{A}$; NUV, 2267 $\mathring{A}$) global properties of nearby galaxies, including M 31, were presented by Gil de Paz et al. (2007) using data from the Galaxy Evolution Explorer (GALEX). Figure 1.5 shows the false-colour RGB map of the galaxy (left panel): blue represents the FUV image; red, the NUV image; and green, a linear combination of the two. The DSS-1 (Digitized Sky Survey) optical image of the same field of view is shown alongside for comparison, revealing that the UV emission is comparatively more extended than the optical light. The mean surface brightness was computed within elliptical annuli of fixed center and position angle out to 5 times the D_{25} radius using the central position, ellipticity and position angle of the D_{25} ellipse (Fig. 1.6). The fluxes and magnitudes were obtained using the derived surface brightness profiles and the area of each elliptical annulus, and extrapolating to infinity. The FUV and NUV magnitudes were found to be 8.34±0.01 and 7.50±0.01 mag, respectively with an effective radius of 1462.20″ and 1430.04″, respectively. Kang et al. (2009) derived an average (over the last 400 Myr) star formation rate (SFR) of $\sim$ 0.6 or 0.7 $M_\odot$ yr^{-1} (for metallicity 0.02 or 0.05, respectively) from UV observations of young star forming regions. They detected 894 SF regions over the 26 kpc disk.

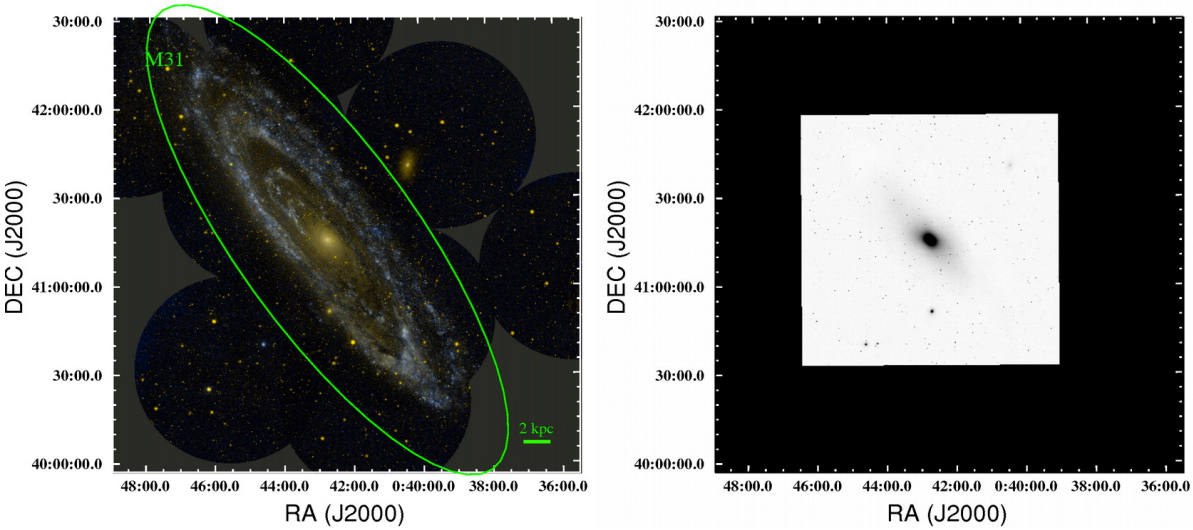

Figure 1.5: False-colour UV (GALEX) image of M 31 with the DSS-1 image of the same field of view alongside (Gil de Paz et al. 2007).

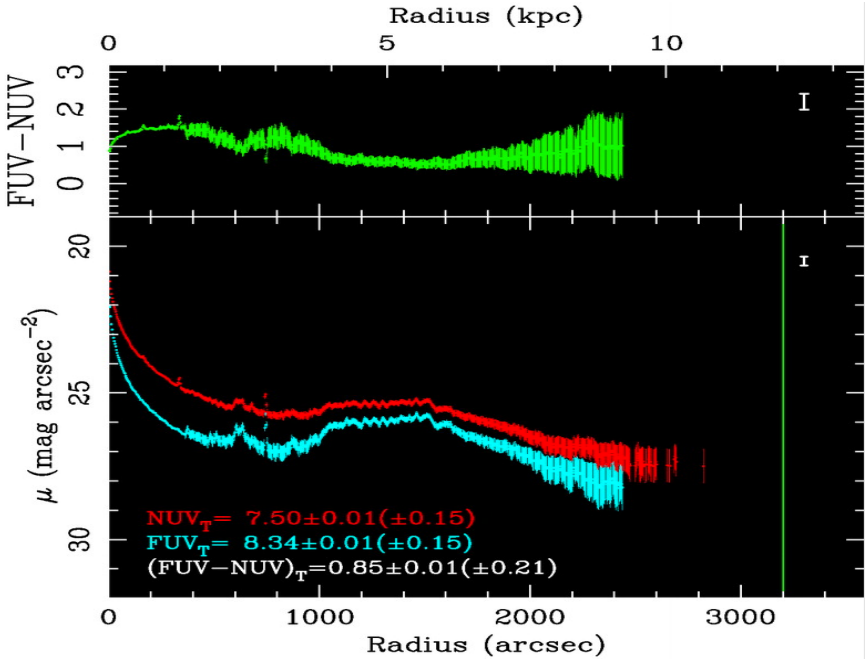

Figure 1.6: FUV and NUV surface brightness and colour profiles of M 31 derived by Gil de Paz et al. 2007.

1.2.3 Optical Emission

The peak radiation of most stars lies in the visible range of the electromagnetic spectrum, therefore, optical observations form a major part of determining the stellar content, structure, and mass of galaxies. However, the presence of dust in galaxies affects the optical (and ultraviolet) emission observed by absorbing part of the radiation. The absorbed energy is reradiated at infrared wavelengths, therefore, one can (theoretically) restore the intrinsic properties of galaxies by observing them in the IR to far-IR (see Sect. 1.2.4).

Tempel et al. (2010) created a three-dimensional galaxy model with axi-symmetric stellar populations in order to estimate extinction and, hence, restore the intrinsic luminosity and colour distributions of a galaxy. The model was applied to M 31, using the *Spitzer* far-IR maps to determine the dust distribution (estimated by approximating the far-IR spectral energy distribution with modified black body functions assuming the presence of a colder and a warmer dust component). The calculated total extinction-corrected luminosity of M 31 was found to be $L_B = (3.64 \pm 0.15) \times 10^{10}\ L_\odot$, corresponding to an absolute luminosity M_B=-20.89 ± 0.04 mag. This implied that 20% (0.24 mag) of the total B-luminosity is obscured by the dust in M 31.

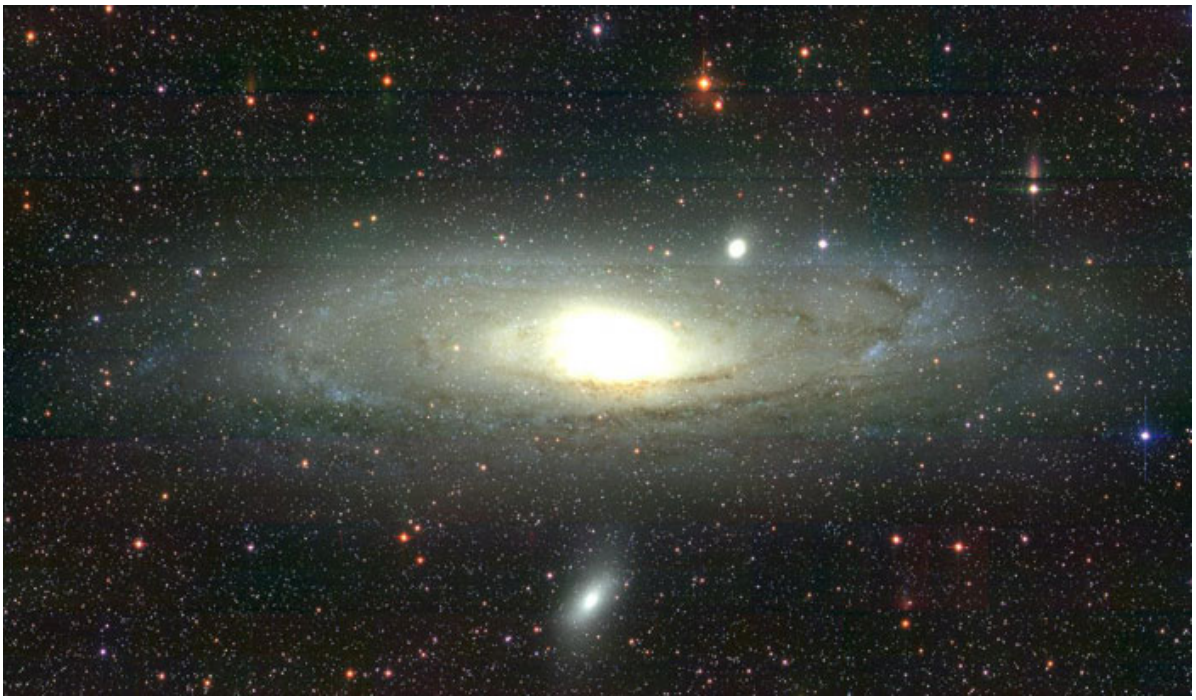

Figure 1.7: Optical image of M31 from the Sloan Digital Sky Survey.

1.2.4 Infrared Emission

Ultraviolet and Optical radiation absorbed by dust is reradiated at IR to far-IR wavelengths. Observing galaxies in the IR range allows for the spatial distribution, temperature and physical properties of interstellar dust grains to be understood. This in turn allows for the restoration of intrinsic photometric properties of galaxies where estimates of light extinction are not applicable (Tempel et al., 2010).

Montalto et al. (2009) collected all the integrated flux measurements of M 31 performed using observations that had been acquired with different instruments (IRAC and MIPS) on the *Spitzer* Space Telescope (SST) as well as COBE, IRAS, MSX and ISO. The aim was to directly compare the fluxes in each band; therefore, the obtained images were resampled to the same astrometric reference system. The flux densities, specifically in the 3.6, 8.0, 24, 70, and 160 μm bands (IRAC and MIPS observations) from Barmby et al. (2006, Fig. 1.9) and Gordon et al. (2006, Fig. 1.10), were then recalculated. Fig. 1.9 shows mid-IR images of the galaxy (3.6-8 μm), where emission is mostly due to evolved stars and molecules in the interstellar medium. Fig. 1.10 shows far-IR images of the galaxy (24-160 μm), due to dust emission heated by star formation. The bottom panel shows the three-colour composite of the MIPS images; the colour gives an indication of the dust temperature (cyan -hot, red -cold). The images reveal the presence of two spiral arms in addition to a ring of star formation which forms an almost complete circle. The shape and splitting of the ring suggest M 31 is not undisturbed, but has been significantly affected by interactions. The same area was used in all the images to

measure the integrated flux (semi-major axis = $84'$ and semi-minor axis = $18'$).

The resultant fluxes, presented in Table 1.2, were found to be in good agreement with previous measurements by Barmby et al. (2006) and Gordon et al. (2006), and define the spectral energy distribution (SED) of M 31 in the infrared range (from ~ 4 μm to ~ 160 μm). The 4.5 and 12 μm fluxes are also shown in Table 1.2 for completeness (Barmby et al., 2006; Rice et al., 1988). The infrared SED was plotted using the recalculated fluxes, as well as fluxes obtained from previous studies using COBE, IRAS, MSX and ISO for comparison. The SED was found to be dominated by cold-dust emission, by fitting a model of Draine et al. (2007) to the data. A lower limit of $M_{dust} > 1.1 \times 10^7 M_\odot$ was derived for the dust-mass, a weak constraint as majority of the analyzed observations are found at shorter wavelengths than the peak (~ 160 μm). The result, however, is in agreement with expectations from CO and HI measurements.

The recent HELGA (*Herschel* Exploitation of Local Galaxy Andromeda) Survey observed the M 31 region ($\sim 5.5^\circ \times 2.4^\circ$) at five far-IR wavelengths (100-500 μm). Fritz et al. (2012) presented *Herschel* maps in the five bands, viz., 100 and 160 μm (PACS), and 250, 350 and 500 μm (SPIRE), which are shown in Fig. 1.11. They measured the respective flux densities within an elliptical annulus with semi-major axis 42.4 kpc and semi-minor axis 9.5 kpc, see Table 1.2. Ford et al. (2013) used the maps to estimate the SFR using far-UV and 24 μm emission for calibration, and found a global value of $0.25^{+0.06}_{-0.04}$ $M_\odot yr^{-1}$. Viaene et al. (2014) combined *Herschel* data with data from GALEX, SDSS, WISE and *Spitzer*, to obtain estimations of the SFR and total stellar mass of $0.189^{+0.002}_{-0.01}$ $M_\odot yr^{-1}$ and $(5.5 \pm 0.01) \times 10^{10}$ $M_\odot$, respectively.

Gordon et al. (2006) fit a simple stellar population-plus-dust grain model (Marleau et al., 2006) to their SED with their MIPS global fluxes along measurements from COBE, IRAS, MSX and ISO. The fit resulted in an IR luminosity measurement of 1.7×10^{43} ergs s^{-1}, which corresponds to an SFR of 0.75 $M_\odot yr^{-1}$ using the Kennicutt (1998) calibration. Barmby et al. (2006) derived an SFR of 0.4 $M_\odot yr^{-1}$ using the Wu et al. (2005) calibration for SFRs as a function of 8 μm non-stellar luminosity.

Table 1.2: M 31 infrared integrated flux densities.

λ	f_ν
μm	Jy
3.6	239 ± 29 [a]
4.5	144 ± 20 [b]
8.0	149 ± 27 [a]
12	163 ± 24 [c]
24	118 ± 17 [a]
70	1086 ± 256 [a]
100	3055 ± 31 [d]
160	7315 ± 1632 [a]
160	7348 ± 73 [d]
250	5791 ± 405 [d]
350	3047 ± 213 [d]
500	1313 ± 92 [d]

References. [a] Montalto et al. (2009), [b] Barmby et al. (2006), [c] Rice et al. (1988), [d] Fritz et al. (2012).

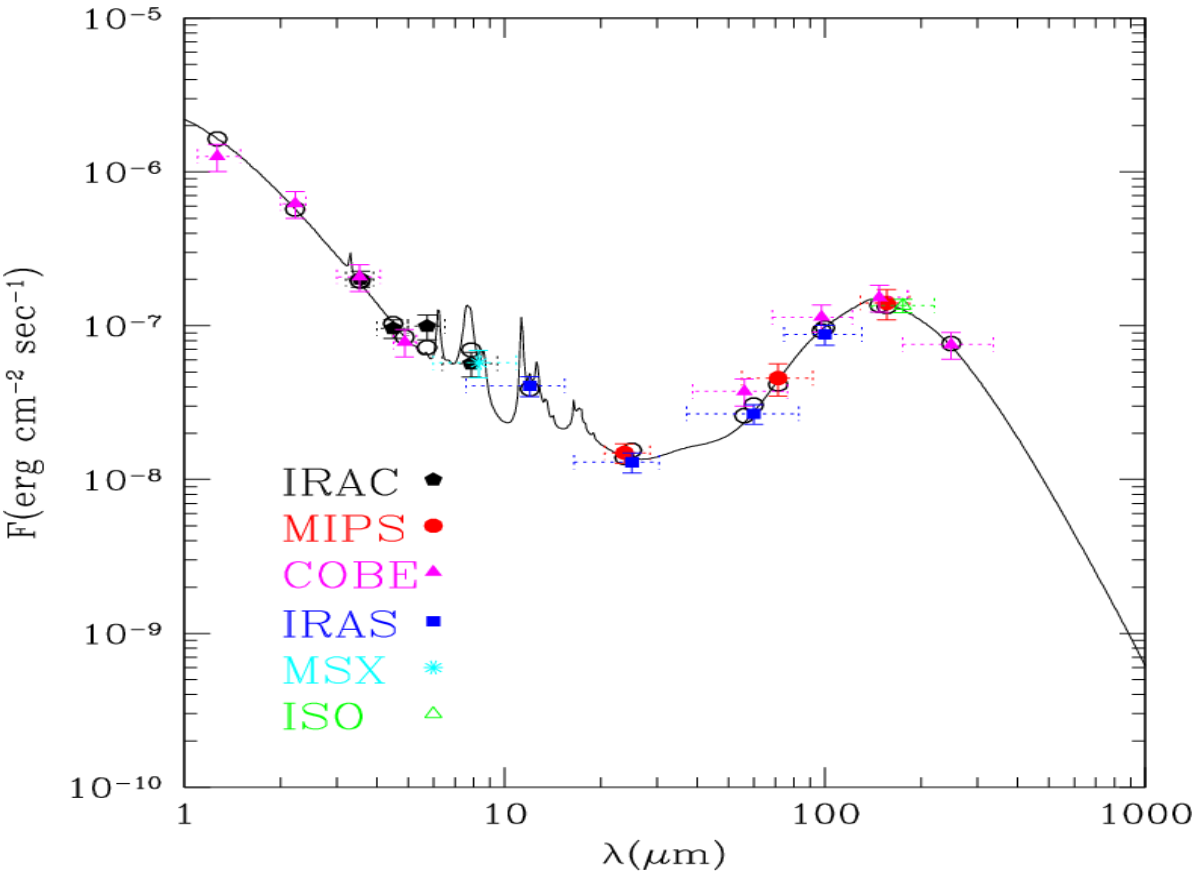

Figure 1.8: Infrared spectral energy distribution of M 31 using measurements from different instruments (IRAC, MIPS, etc) that have been used to observe the galaxy (Montalto et al., 2009). The continuous line, the best-fit model from Draine et al. (2007), is shown for comparison.

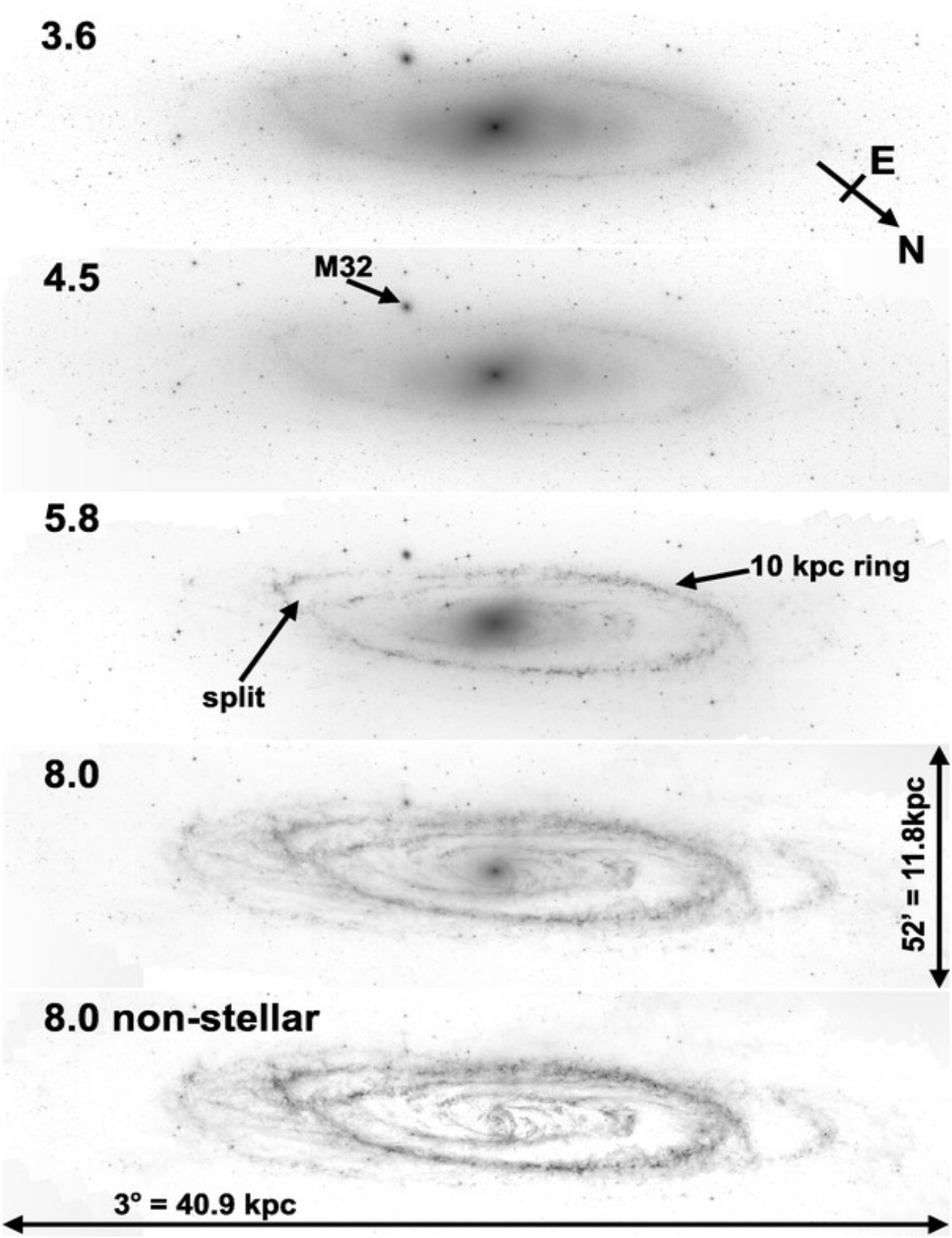

Figure 1.9: Mid-infrared logarithmic gray scaled images of M 31 covering an area of $3^\circ \times 0.9^\circ$ as seen in IRAC bands 3.6, 4.5, 5.6 and 8 μm (Barmby et al., 2006).

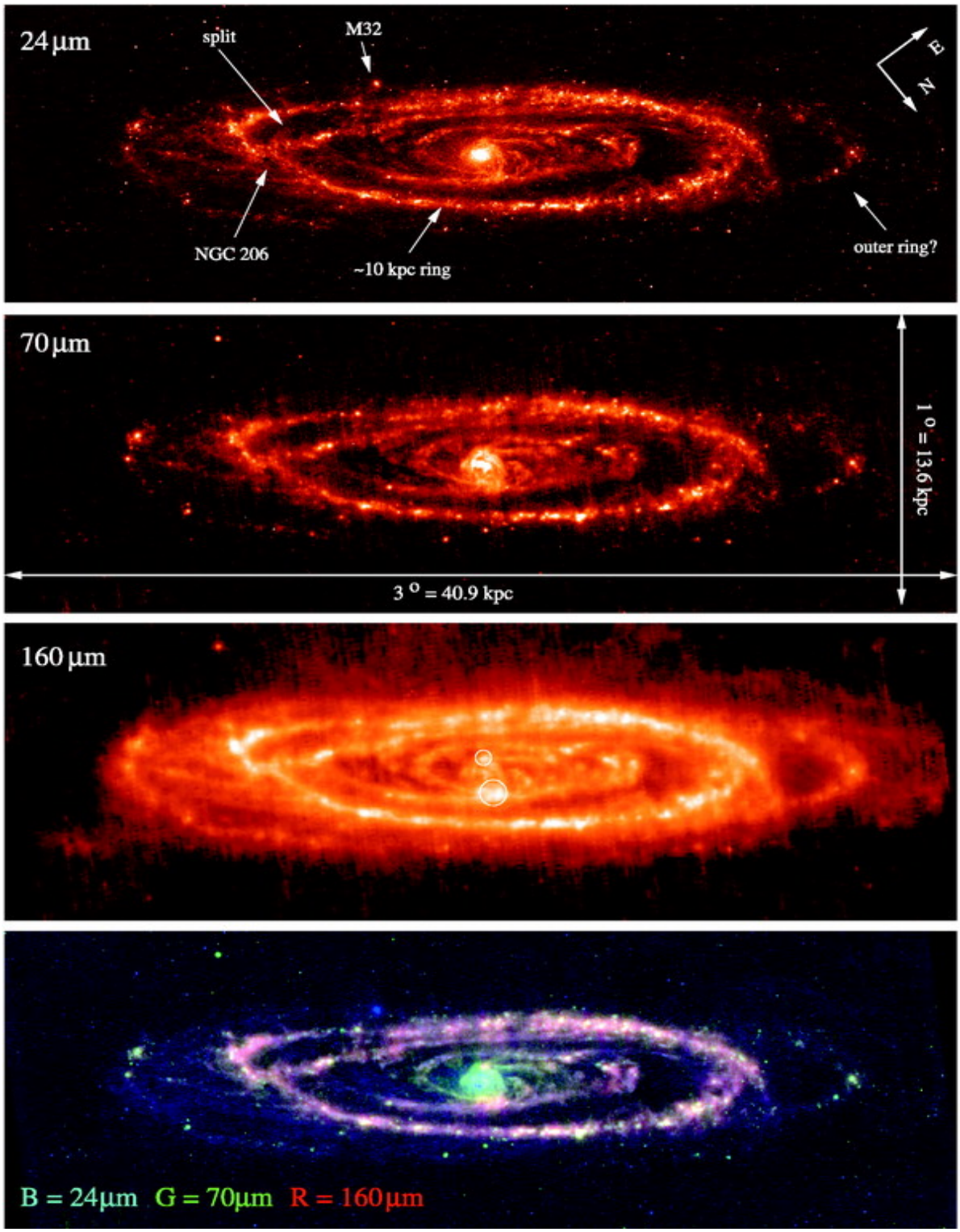

Figure 1.10: Far-infrared MIPS images of M 31 (scaled using quadratic root) in the 24, 70 and 160 μm bands (Gordon et al., 2006). The bottom panel shows the three-colour composite of the images indicating the dust temperature.

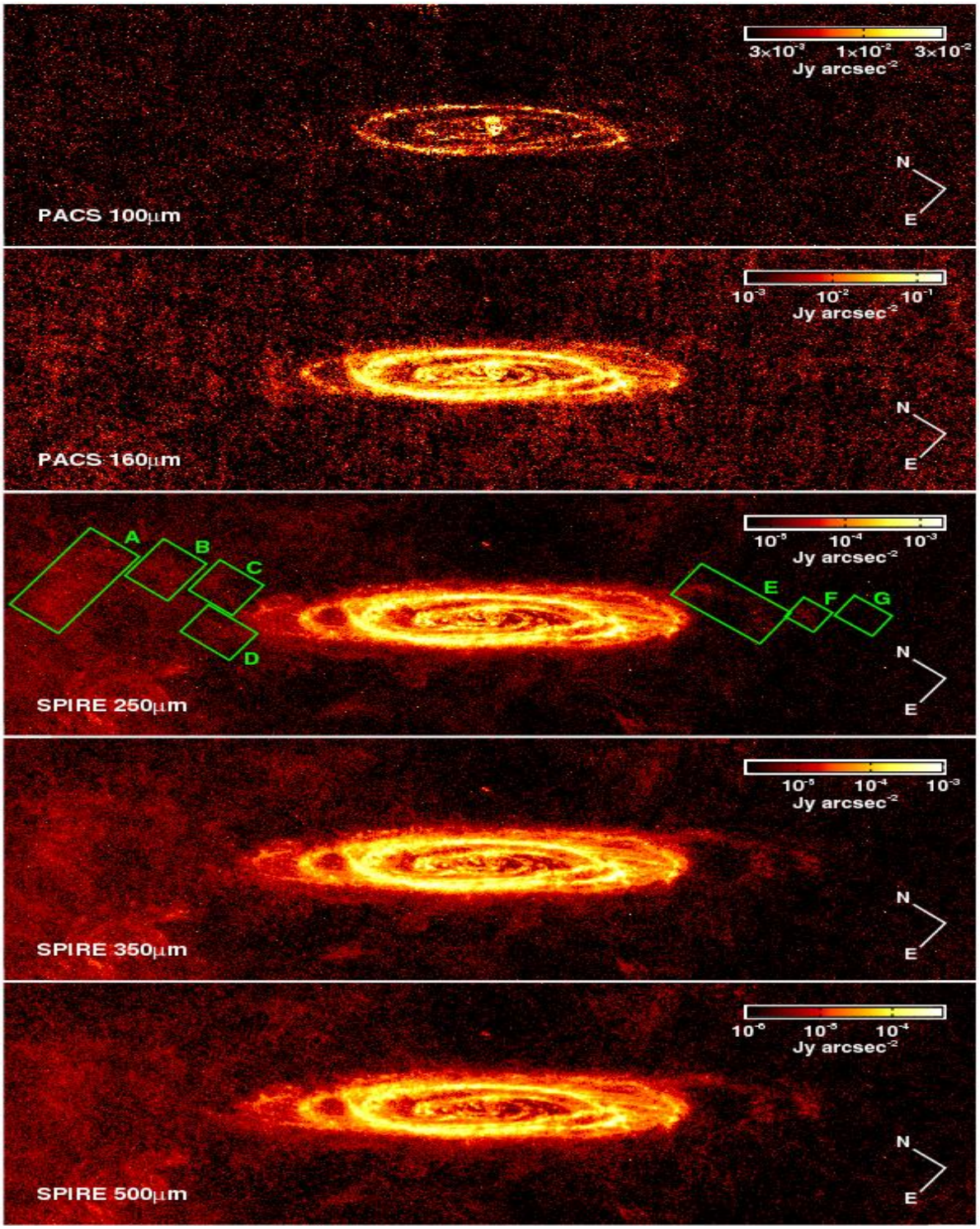

Figure 1.11: Far-infrared *Herschel* PACS (100 and 160 μm) and SPIRE (250, 350 and 500 μm) images of the M 31 region (Fritz et al., 2012). The green rectangles in the 250 μm map represent tentative detections of dust in the outskirts of the galaxy. The directional axes length corresponds to $15'$ (3.4 kpc).

1.2.5 Radio Emission

Radio observations can probe the gas content of galaxies, specifically neutral hydrogen (HI). HI is of primary importance from an evolutionary standpoint, as generally a galaxy abundant in HI indicates potentially active star formation processes, while a galaxy lacking in HI indicates an aging stellar population. HI observations are also important for determining the dynamical mass of galaxies.

A 21 cm survey of M 31 was made based on high-resolution observations with the Synthesis Telescope and the 26 m antenna at the Dominion Radio Astrophysical Observatory (DRAO, Chemin et al. 2009). The HI distribution and kinematics of the disk were analyzed in order to determine the basic dynamical properties of the galaxy (Fig. 1.12). From the HI profile (left panel in Fig 1.12), an integrated flux of 29221.4 Jy km s^{-1} (1.39×10^8 Jy Hz) was found, implying a total HI mass of $4.23 \times 10^9 M_\odot$. The dynamical mass enclosed within a radius of 38.1 kpc (10000″) was found to be $(4.7 \pm 0.5) \times 10^{11} M_\odot$ which includes baryonic mass (black hole, stellar and gaseous mass) and dark matter. The total enclosed mass derived inside the virial radius (159 kpc) was then found to be $1.0 \times 10^{12} M_\odot$. This measurement is in good agreement with lower limits determined from previous studies, viz. Ibata et al. (2004) and Chapman et al. (2006) with $5.4 \times 10^{11} M_\odot$ and $9 \times 10^{11} M_\odot$ respectively.

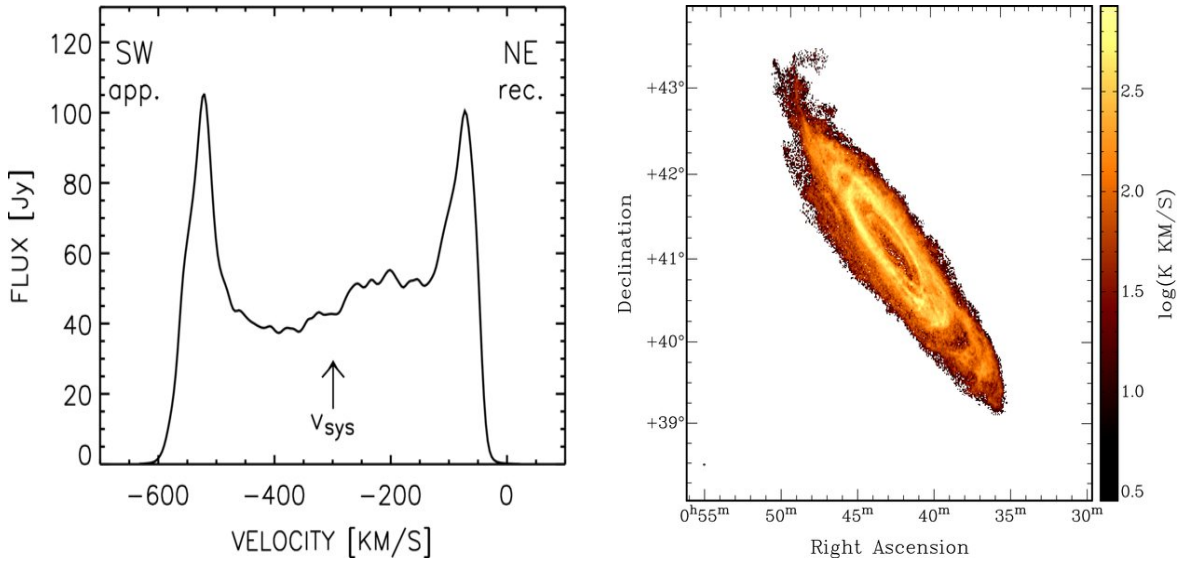

Figure 1.12: HI integrated profile (left panel), and total HI distribution of M 31 (right panel) from DRAO observations (Chemin et al., 2009).

1.2.6 Summary of Photometric Properties

The photometric fluxes across the electromagnetic spectrum are tabulated below. These measurements, along with measurements that are obtained from the WISE data, will be used to plot the SED of the galaxy in Chapter 4.

Table 1.3: M 31 Photometric Properties.

	Instrument	Band [μm]	Semi-major Radius [arcsec]	Integrated Flux [Jy]
X-ray 20-100 keV	BAT [a]	3.1×10^{-5}	1200	$(9.1 \pm 1.2) \times 10^{-7}$
2-20 keV	PCA [a]	1.4×10^{-4}	1200	$(4.2 \pm 0.4) \times 10^{-6}$
UV AB	GALEX [b]	0.15	1462	1.67±0.01
	GALEX [b]	0.23	1430	3.82±0.02
Optical B	SDSS [c]	0.48	4599	278 ± 11
Infrared	2MASS [d]	1.3	3100	230 ± 3
	2MASS [d]	1.7	3100	314 ± 5
	2MASS [d]	2.2	3100	269 ± 4
	IRAC [e]	3.6	5040	239 ± 29
	IRAC [f]	3.6	6480	259 ± 32
	IRAC [f]	4.5	6480	144 ± 20
	IRAC [e]	8.0	5040	149 ± 27
	IRAC [f]	8.0	6480	151 ± 21
	IRAS [g]	12	5334	163 ± 24
	MIPS [e]	24	5040	118 ± 17
	IRAS [g]	25	5334	108 ± 16
	IRAS [g]	60	5334	536 ± 80
	MIPS [e]	70	5040	1086 ± 256
	IRAS [g]	100	5334	2928 ± 439
	PACS [h]	100	11140	3055±31
	MIPS [e]	160	5040	7315 ± 1632
	PACS [h]	160	11140	7348±73
	SPIRE [h]	250	11140	5791±405
	SPIRE [h]	350	11140	3047±213
	SPIRE [h]	500	11140	1313±92
Radio	DRAO [i]	21×10^4	10000	9.79×10^{-2}

Notes. [a] Revnivtsev et al. (2014), [b] Gil de Paz et al. (2007), [c] Tempel et al. (2010), [d] Jarrett et al. (2003), [e] Montalto et al. (2009), [f] Barmby et al. (2006), [g] Rice et al. (1988), [h] Fritz et al. (2012), [i] Chemin et al. (2009).

1.3 M 31 Globular Clusters

The study of globular cluster systems is a fundamental part of the investigation of the formation and evolution of their host galaxies. This is because their spatial distribution and chemical composition are distinctly different from most stars, thereby revealing a different aspect of galactic structure. Globular clusters (GCs) are also the oldest objects in their host galaxies; therefore they contain information regarding the formation and early evolution of the galaxy (Ashman & Zepf, 1998).

The M 31 globular cluster system has been studied for over 80 years (Hubble, 1932). The first catalogues of candidates were made as early as 1932 by Hubble, who identified 140 objects in the vicinity of the galaxy as globular clusters. Further detections, analyses and classifications have since been published by authors such as Sargent et al. (1977), Crampton et al. (1985), Barmby et al. (2000, 2001), Galleti et al. (2004, 2009) and many others. These studies include GC candidate lists, their optical colours and spectral indices. Galleti et al. (2004) obtained J, H, K integrated photometry for some confirmed GC's and candidates from the 2MASS database spread out over an area of more than $3^\circ \times 3^\circ$ around the center of M 31. This, including previous photometric data of other candidates, constituted the Revised Bologna Catalogue and is the most comprehensive list of confirmed and candidate clusters with 337 confirmed GC's and 688 candidates. Metallicity estimates for 245 entries of the catalogue were obtained by Galleti et al. (2009) using Lick indices. The study found that most metal-rich GC's tend to cluster around the center of the system and also cluster tightly around the galactic rotation curve defined by the HI disk, while the velocity dispersion about the curve increases with decreasing metallicity. An estimate of the total number of GC's made by Barmby & Huchra (2001) using their completeness results was 460 ± 70.

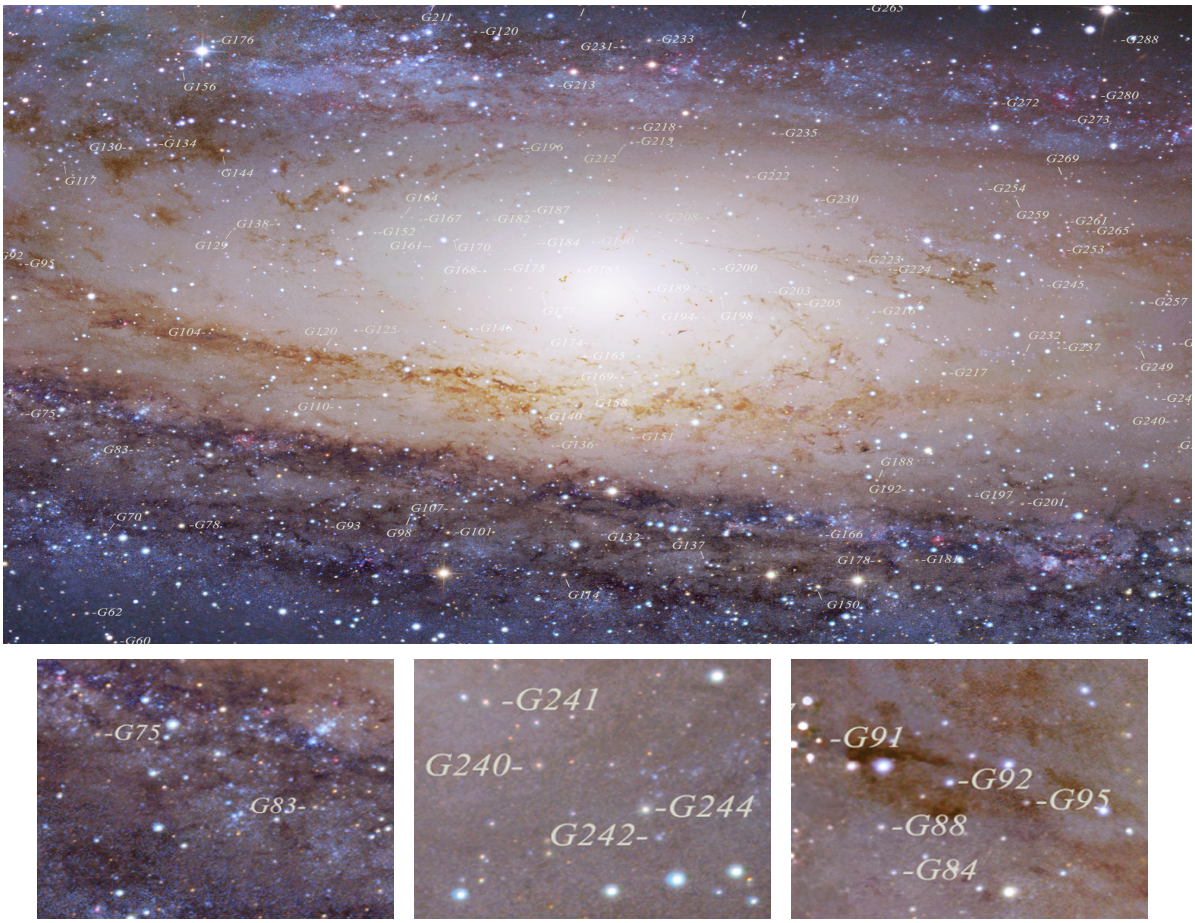

Figure 1.13: Globular clusters in M 31. The top panel shows central globular clusters and the bottom panel shows clusters from random regions in the galaxy (Gendler, 2006).

1.4 M 31 Satellite Galaxies

Investigating the structure and distribution of satellite galaxies is not only important to understand their evolution, but also the evolution of their host galaxies, as they are linked via gravitational forces and other effects associated with orbiting them. The Pan-Andromeda Archaeological Survey (PAndAS), using the Canada-France-Hawaii Telescope, designed to investigate the structure and content of M 31 (and its satellite M 33) out to 150 kpc from the galaxy has observed satellites which have been previously detected (van den Bergh, 2006) and has also revealed a substantial dwarf galaxy population in the halo of the galaxy (McConnachie et al., 2009). To date, there have been about 30 M 31 satellite galaxies detected (25 dwarf spheroidal galaxies) with the PAndAS survey (Richardson et al., 2011, see Fig. 1.14) as well as the Sloan Digital Sky Survey (SDSS; Bell et al., 2011; Slater et al., 2011) at distances from the galaxy as small as 6 kpc (M 32), and as large as 365 kpc (And XXVIII). The satellites have absolute magnitudes ranging from -6.4 to -16.5 mag, and metallicities ranging from -0.5 to -1.9. Knowledge of the satellite system is, however, incomplete at the faint end as current wide area observations are limited to detections at the bright end ($M_V \leq -6.5$; Richardson et al., 2011). Intriguing work by Conn et al. (2013) revealed that 15 M 31 satellites (of the 27 observed) lie within a thin disk that is almost perpendicular to the Milky Way disk (Fig 1.15). In addition, the majority of the satellites detected lie on the Milky Way side of the galaxy; implying that the M 31 and Milky Way halos, are not completely isolated structures.

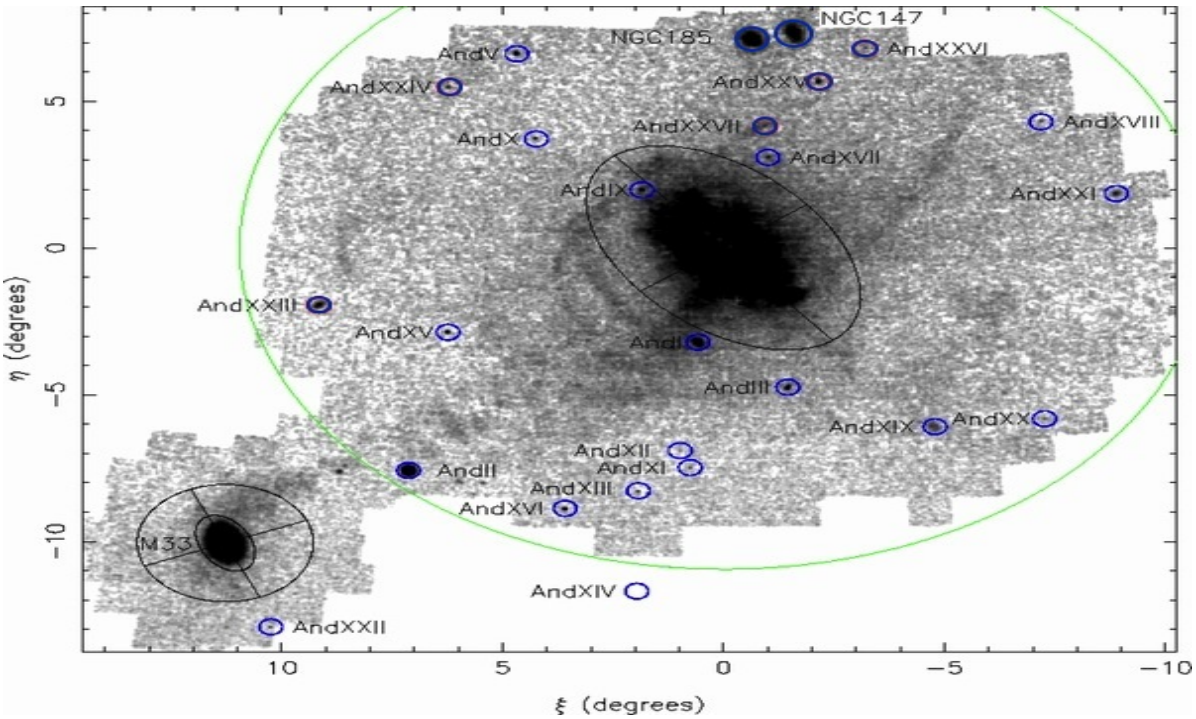

Figure 1.14: Satellite population of M 31 (Richardson et al., 2011). The green circle shows the maximum projected radius of 150 kpc for the PAndAS survey.

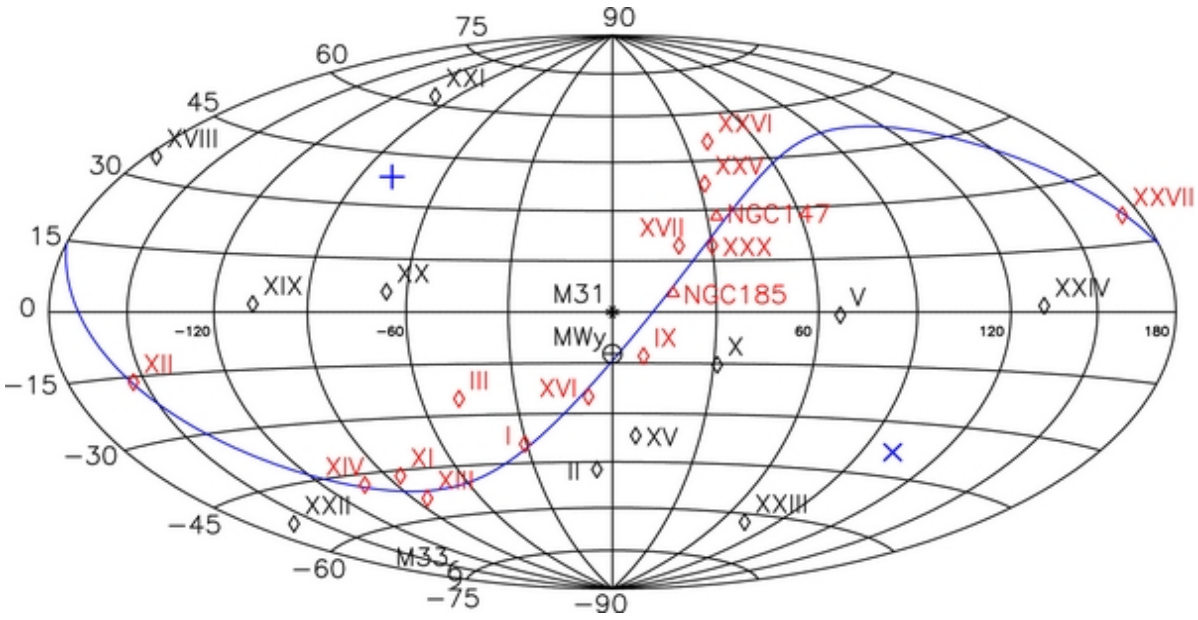

Figure 1.15: An Aitoff-Hammer Projection showing the Great plane of M31 satellites (Conn et al., 2013). Positions show the appearance of each satellite from the sky if viewed from the center of M 31.

1.5 Thesis Outline

In this dissertation, the global properties of the M 31 system are addressed using WISE combined with ancillary data. The infrared photometric and surface brightness properties are measured and contrasted across the electromagnetic spectrum to create a multi-wavelength catalogue of the galaxy.

The dissertation has the following structure. Chapter 2 presents the method of characterizing the foreground Milky Way population; thereby obtaining clean WISE images of M 31. Chapter 3 presents the characterization results for M 33, the galaxy used as a test of the discussed method. In Chapter 4, basic photometric measurements of M 31 are presented using cleaned data. Chapter 5 discusses the local M 31 environment (GCs and satellites) as seen by WISE. Finally, in Chapter 6, a summary is given as well as future perspectives.

Chapter 2

Distinguishing the Milky Way Population from the M 31 System

In this chapter, a statistical classification scheme for identifying the foreground Milky Way population in the WISE images is formulated in Sect. 2.1. This is necessary in order to obtain a clean measurement of M 31 and its system. The population characteristics of the region are shown in Sect. 2.2 followed by an application of the classification scheme in Sect. 2.3. The statistical results are then analyzed in Sect. 2.4 with a description of dealing with the incompleteness of WISE in Sect. 2.4.1.

2.1 Statistical Classification Scheme

To characterize and extract the M 31 system, the WISE images must be adequately cleaned of all Milky Way (MW) stars located in the foreground to M 31. This is a two step process: (1) identify and separate the source populations, and (2) remove the stars identified as Milky Way from the images. The objective is to statistically identify the nature of a source (i.e., to which set of classes the source belongs, MW or M 31) in the image, given several features $D = D_1, ..., D_n$ of the source. This is done probabilistically with the probability, $P(C_i|D)$, denoting a real number describing the degree of belief in the class C_i of the source, on the condition that $D_1, .., D_n$ are true. Since M 31 is much further away, the photometric features of its sources should differ from those of the MW, i.e., its stars are much fainter and differ in color to those of the MW because WISE is more sensitive to the more luminous evolved population. It is assumed that there are only two types of classes, type C_1 (corresponding to a foreground Galactic source) and type C_2 (a source belonging to the M 31 galaxy system). There are also background galaxies, however, these are not removed as they resemble, in color and morphology, the SF regions belonging to M31. Therefore, types C_1 and C_2 form a complete set of mutually exclusive classes denoted by $\{C_i\}$ such that

$$P(\{C_i\}|D) = \sum_i P(C_i|D) = 1 \tag{2.1}$$

Assuming that the features are independent of each other, the probability that a source is of type C_i is

$$P(C_i|D_j, ..., D_n) = \sum_j^n w_j \times p(C_i|D_j), \tag{2.2}$$

where $w_j \in [0, 1]$ is the weight, the confidence in the class C_i, and $p(C_i|D_j)$ is the likelihood of the possibility of C_i with feature D_j. As one cannot be absolutely certain of the class of a source, each source is assigned a random number, $ran(u) \in [0, 1]$, which is then compared to the probability metric in (2.2), determining whether a source is of type C_1 or C_2. Since MW sources are spread throughout the sky, the null hypothesis is that all sources in the region concerned are Galactic. Therefore, the Galactic population that is located adjacent to M 31 is used as the control to identify and separate the MW and M 31 populations. See Sect. 2.2.2 for a discussion on how this region determined.

2.2 Population Characteristics of M 31 region

The classification scheme is formulated by investigating three metrics: the infrared flux (WISE and 2MASS), color and proximity to the M 31 core. This scheme is inspired by early work done by Block (2011) in classifying fulgurites. However, this scheme expands the method to include more bands, colors and careful treatment of stellar number density curves. To assess the reliability of the classification scheme for removing foreground sources, the characteristics of the source catalogue data are investigated. The WISE data for the sources were extracted through IRSA from the WISE All-Sky Source Catalog[1] centered on M 31 spanning 6° to fully encompass the $6° \times 6°$ WISE images, thus including both the M 31 system and the surrounding Milky Way population. 2MASS photometric data was also extracted from the 2MASS All-Sky Source Catalog for near-IR data to supplement source characterization, as 2MASS data provides near-IR (1-3 μm) information for the sources. Atlas image mosaics of M 31, which were made using a resampling and co-addition method optimized for point source detection, are provided from the WISE mission (Wright et al., 2010) and are publicly available from the Infrared Science Archive (IRSA; Cutri et al., 2012). However, these images are not large enough for the study M 31, nor are they optimized for extended source emission. Therefore,

[1] http://irsa.ipac.caltech.edu/applications/Gator/

new mosaics of the images were constructed using a 'drizzle' co-addition algorithm that preserves the native resolution of WISE imaging (Masci, 2013). This achieves effectively a resolution of 5.9″, 6.5″, 7.0″ and 12.4″ in the W1, W2, W3 and W4 bands, respectively (Jarrett et al., 2012). The completed mosaics have 1.5″ pixels and span 6° in order to cover the entire region of the M 31 system, including the extended disk and greater halo. These mosaics, which have 40 to 50% improved resolution, are available on request.

2.2.1 Source Selection

A total of 369278 WISE sources were extracted within $\sim$ 27 deg^2 region defined by $7.68° \leq \text{RA} \leq 13.68°$ and $38.27° \leq \text{Dec} \leq 44.27°$. To minimize spurious detections, only sources with the following criteria (for each band) were considered in the analysis:

Table 2.1: Per WISE and 2MASS band criteria for foreground determination analysis.

Signal-to-noise	≥ 5
Reduced chi^2	< 2
Number of blend components used in fit	< 2
Active deblend	*No*

The signal-to-noise criteria is chosen to avoid spurious detections. Note that M 31 sources are likely to be faint, therefore, sources that don't meet this criteria are more likely to be M 31 sources. The reduced chi^2 criteria is chosen to separate point sources from extended ones (Jarrett et al., 2013), and the blend criteria are chosen to avoid confused sources, which are more likely to be M 31 sources. The criteria resulted in 337757 sources. The total number of 2MASS sources was 377600. The photometric properties of these sources are presented below, where the magnitudes are in Vega units.

2.2.2 Spatial and Photometric Properties of sources in M 31 region

An important parameter for discriminating M 31 from Galactic sources is the angular proximity to the core of M 31 itself. Consequently, the source photometry as a function of the distance to the center of M 31 is analyzed. The (approximate) elliptical shape of M 31 is used to set the geometric parameters, see Table 2.2. The region is then divided into 32 elliptical shells centered on M 31 using the galaxy's axis ratio and position angle. The semi-major axis for the innermost shell is 0.2° and subsequent semi-major axes increase by 0.1° with the outermost being 3.3° from the center of M 31, resulting in a total of 143264 sources to be analysed. Small regions encircling the satellite galaxies

in the region, viz., M 32 and M 110 shown in red ellipses in figure 2.1, are excluded from the analysis. This is done by placing ellipses centered on M 32 and M 110, with semi-major axes 0.08° and 0.2°, respectively, chosen such that they encompass the bulk of the satellite emission, see Table 2.2.

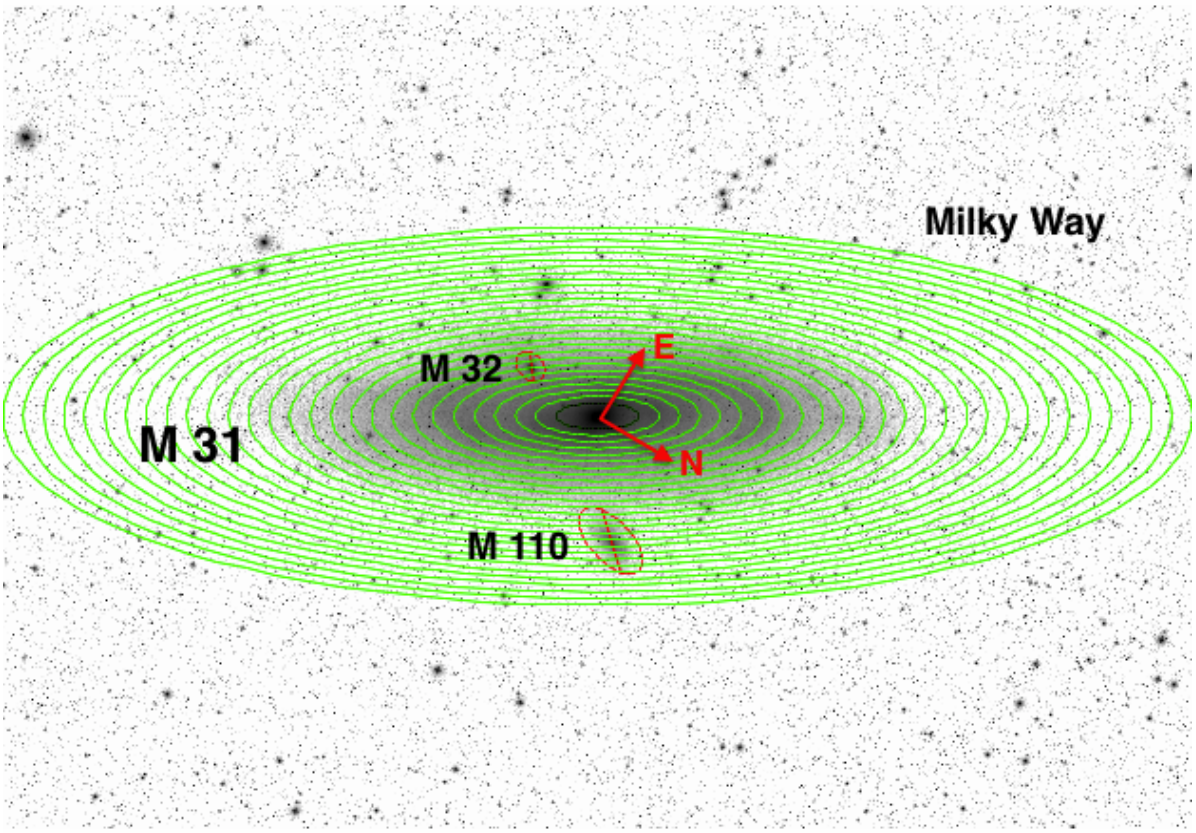

Figure 2.1: Elliptical shells centered on W1 image of M31 (innermost semi-major axis is 0.2°, outermost is 3.3°). Satellite galaxies M 32 and M 110 have red ellipses that demark the masked regions from the M 31 analyses.

Table 2.2: Properties of ellipses centered on M 31 and satellites.

	M 31	M 32	M 110
RA	00h42m44.3s [a]	00h42m41.8s [c]	00h40m22.08s [d]
Dec	+41d16m08.63s [a]	+40d51m55.03s [c]	+41d41m07.10s [d]
PA [deg]	38 [b]	100 [a]	100 [a]
b/a	0.32 [a]	0.75 [a]	0.50 [a]

References. [a] de Vaucouleurs et al. (1991), [b] Walterbos and Kennicutt (1987), [c] Evans et al. (2010), [d] 2MASX (2003).

The source counts separated by the defined shells are now considered. The axisymmetric W1 source counts is plotted against the semi-major axis radius (Fig. 2.2) to examine the distribution of sources across the region, which is used to assess the reliability of the classification scheme. The figure shows the source density distribution with respect to the center of M 31, with mean values computed within the elliptical shells. The region consists of both foreground sources and sources that form part of the M 31 system, as well as background galaxies. The challenge and the task is to determine whether the two types of sources are distinguishable. The black solid line represents all W1 sources; faint sources ($15.5 < W1 < 16.5$) are represented by the dark-grey solid line, the intermediate range ($14.2 < W1 < 14.7$) is represented by the light-grey solid line; and bright sources ($12.0 < W1 < 12.5$), by the grey dotted line. Sources in brightness range $13.0 < W1 < 13.5$ are represented by the grey dashed line to show the transition between the intermediate and bright sources.

The distribution of bright sources, W1 < 12.5 mag, is fairly constant throughout ($\sim$100 sources per square degree), i.e., bright sources in the region are not correlated with proximity to M 31. This is indicates that sources brighter than 12.5 mag belong to the MW. This is not unexpected, the distance modulus to M 31 is 24.46 (Conn et al., 2012), which means mostly luminous groups of M 31 stars will be visible to WISE imaging. A K-giant star ($M_{W1} \sim -3.5$ mag), for example, will have an apparent magnitude of about 21 mag at M 31's distance, which is well beyond the detection limits for WISE ($\sim$ 17 mag). Cepheids and late M giants, however, will be visible to WISE imaging. In contrast, sources in the intermediate brightness range, $14 < W1 < 15$, show an overdensity in the inner regions ($a < 1.3°$) due to the presence of M 31 sources adding to the regular foreground MW population; after which, the source count converges to about 600 per square degree. In the faint regime, the source counts converge at a later stage ($a > 2°$) to about 3000 sources per square degree.

All the distributions converge to a constant level as expected, since M 31 sources should decrease exponentially with radius, while Galactic sources are distributed uniformly across the region (notably along the same Galactic latitude). However, what is also seen, for the faint and intermediate brightness range, is a decrease in the source count distributions in the inner regions; $a < 1.2°$ and $a < 0.3°$ for the faint and intermediate brightness range, respectively. This is attributed to confusion and source blending in the inner regions where sources are too close together to be resolved by the WISE beam. Source confusion is usually a hallmark of high source density fields (such as the plane of the Milky Way), but is also present due to M 31 itself. The light that is seen toward the central regions of M 31 represents potentially thousands of sources along the line of sight. The blending effect is more evident at the faint end.

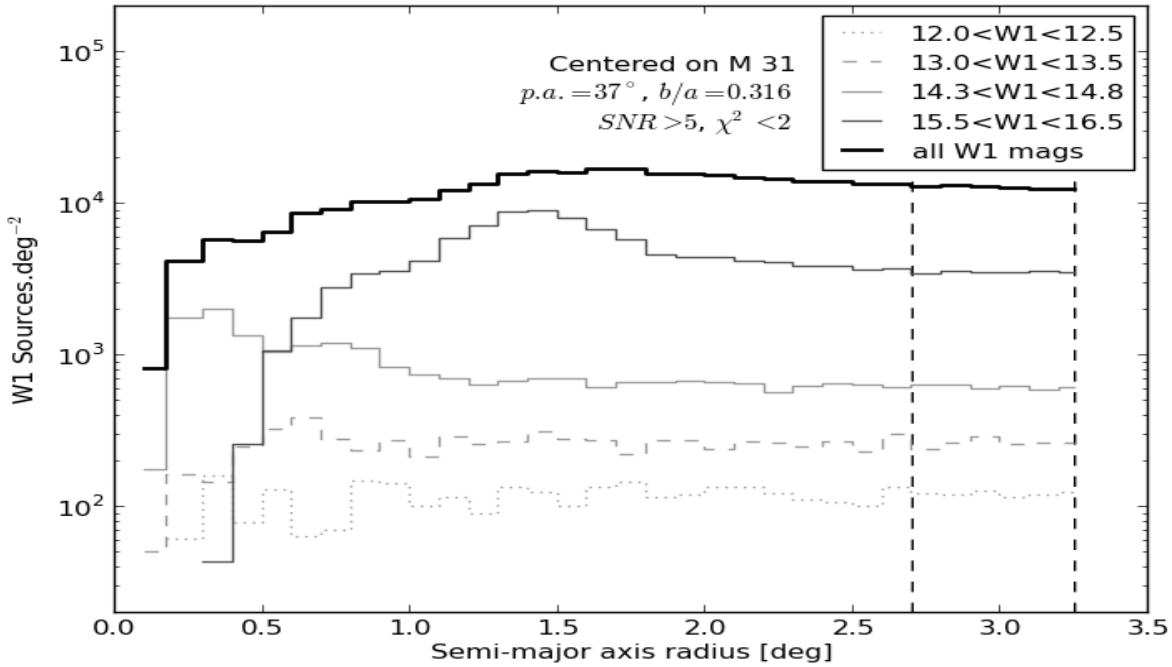

Figure 2.2: Axisymmetric W1 source counts per square degree as a function of radius from the center of M 31. Low, intermediate and high observed flux sources are represented by dark-grey, light-grey and light-grey dashed lines respectively. Outer bins converge to the expected Milky Way source level (vertical dashed black lines at 2.7° and 3.3°, henceforth defined as the MW "background" level).

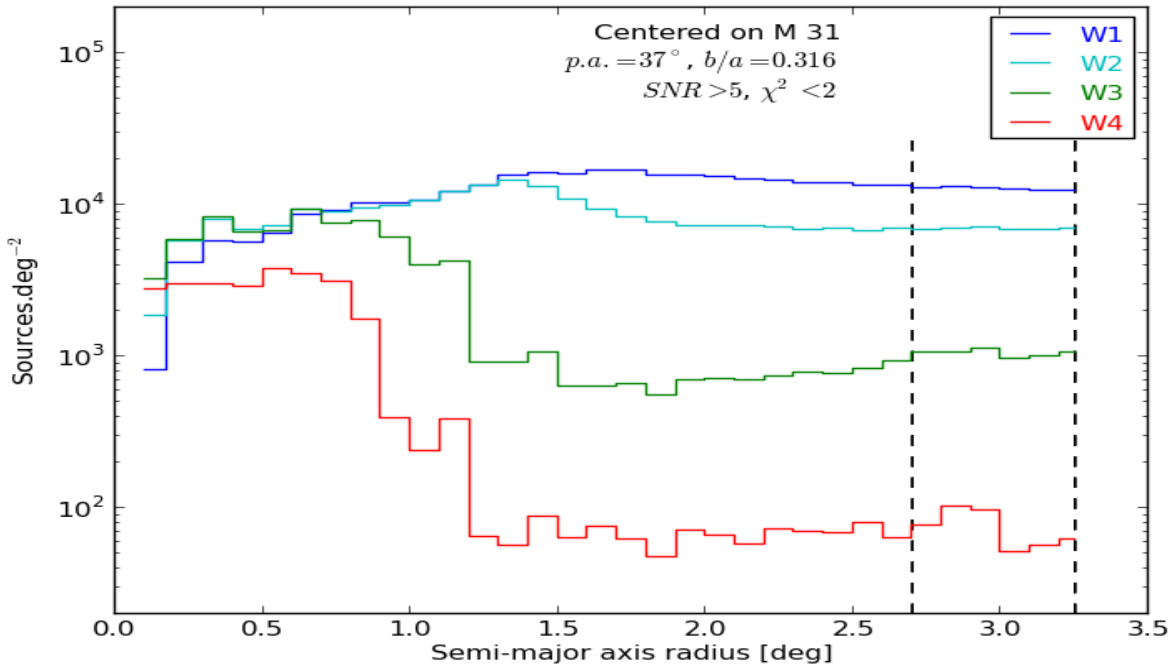

Figure 2.3: Axisymmetric W1, W2, W3 and W4 source counts as a function of radius.

The WISE multi-band source counts are also plotted, showing convergence to Milky Way levels, see Fig. 3.3. Similar trends are seen with W2, W2 and W4 as with W1: confusion in the innermost regions ($a < 1.3°$, $a < 0.6°$ and $a < 0.5°$ for W2, W3, and W4 distributions, respectively), with distributions flattening to Milky Way levels at about $a = 2.4°$, $a = 2.7°$ and $a = 1.4°$ for W2, W3, and W4, respectively. The W1, W2, W3, and W4 source counts are fairly flat in the range $2.7° \leq a \leq 3.3°$, indicated by the vertical dashed lines in Fig. 2.2 and 3.3, consistent with a Galactic distribution. Therefore, all sources in this semi-major axis range (2.7°-3.3°) are considered to be Milky Way sources and will represent the foreground population in further analyses below. Sources with $a > 3.3°$ are considered to be part of the Galactic foreground and will not be included in the analysis.

To further characterize the sources in the M 31 region, the traditional LogN-LogS differential source counts and the color distributions are considered here. The W1, W2, W3 and W4 source number densities (sources per square degree per magnitude bin); and the W1-W2, W2-W3 and J-K_s color histograms (sources per square degree) are plotted for the various shells. Here, a representative 7 shells are highlighted for the differential source counts and shell 7 is highlighted for the color distributions, see Fig 2.4 and 2.5, respectively. The full set of plots are presented in Appendix A. The sizes of the magnitude bins were chosen to optimize the distributions of the histograms. Since the foreground is distributed uniformly across the region, a black line representing the foreground distribution ($2.7° \leq a \leq 3.3°$, as discussed in above paragraphs), is shown in each plot for comparison.

For the W1, W2, W3 and W4 source number densities, the distributions of the inner shells ($a < 2.4°$) show significant deviation from the foreground distribution at the faint end (see Fig. 2.4). In shell 0, $0.0° \leq a \leq 0.2°$, the source number density curves lie under the foreground distribution curves implying that there are fewer sources per square degree compared to the expected foreground population. That is to say there are to few sources in this region. This is attributed to source confusion, individual stars are not resolved by the WISE beam in highly dense regions (large groups of stars are detected as one); therefore, the source count in this region is much lower than in the outer unconfused regions. From shell 1 to about shell 22, $0.2° \leq a < 2.4°$, overdensities relative to the expected Galactic are seen, principally at the faint end. The overdensities also have peak maxima, which propagate to the faint end as the shell number (radius) increases, an indication of incompleteness at the faint end where WISE loses photometric sensitivity. These maxima, where WISE is inferred to be complete, for each band, are shown in Table 2.3, as well as Fig. 2.6 for a visual interpretation. The 2MASS J, H and K peak maxima have also been included in the table (note that the J, H and K maxima do not change as the shell number increases because the 2MASS beam has much less blending issues, see Appendix A, Fig. A.9 to A.11). Moreover, blending of faint sources lowers the detection rate in the inner regions of the galaxy due to the high densities. The confusion effect decreases as the shell number increases, more faint sources are detected and the peak maxima propagate to fainter magnitudes. From shells 23 to 31 ($a \geq 2.4°$), the distributions are much more similar to the foreground distribution ($2.7° \leq a \leq 3.3°$);

therefore, it is concluded that sources in these regions are dominated by the Galactic population.

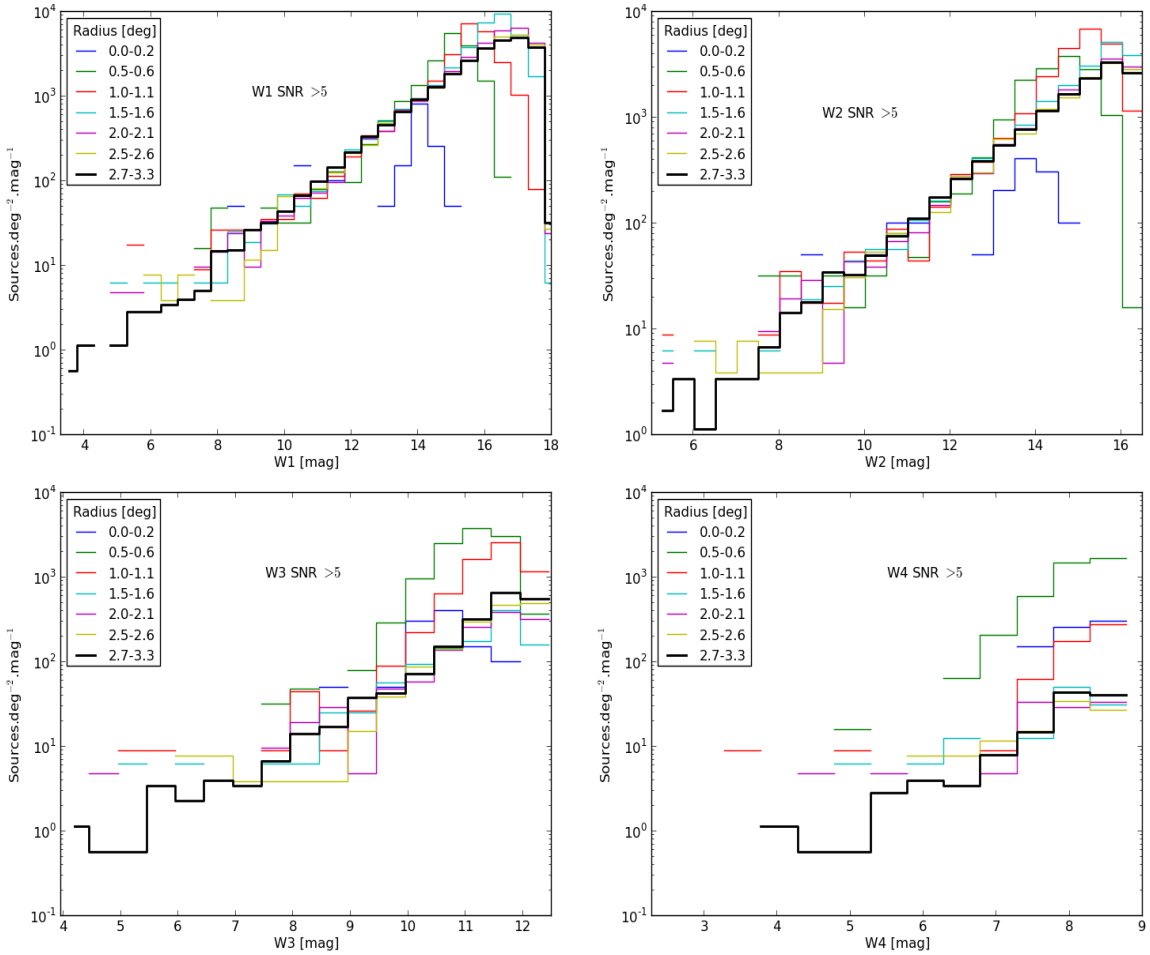

Figure 2.4: The W1, W2, W3 and W4 source number density distributions for a representative 7 shells.

Further insight to the population differences between Galactic and M 31 sources is gained by comparing the color distributions. To mitigate the effects of band-to-band incompleteness on the following statistical analyses, for each WISE color (W1-W2, W2-W3 and W3-W4) and 2MASS color (J-K_s), only magnitudes brighter than the peak maxima (Table 2.3), the point at which WISE loses sensitivity to faint sources, in each shell were used. The maxima are indicated by 'limit' in each color plot for shell 7 ($0.8° \leq a \leq 0.9°$) in Fig. 2.5, the full set of plots are presented in Fig. A.5 to A.8 in Appendix A.

Shell 7 represents the inner shells ($a < 1.9°$) whose color distributions vary significantly from the foreground MW distributions. The inner shells show excess at the red end, viz., W1-W2 > 0.0, W2-W3 > 1.0, W3-W4 > 1.0 and J-K_s > 0.8 mag, respectively; with distributions converging to the foreground distributions thereafter. It is clear that sources belonging to M 31 have a different color from those in the general field. This

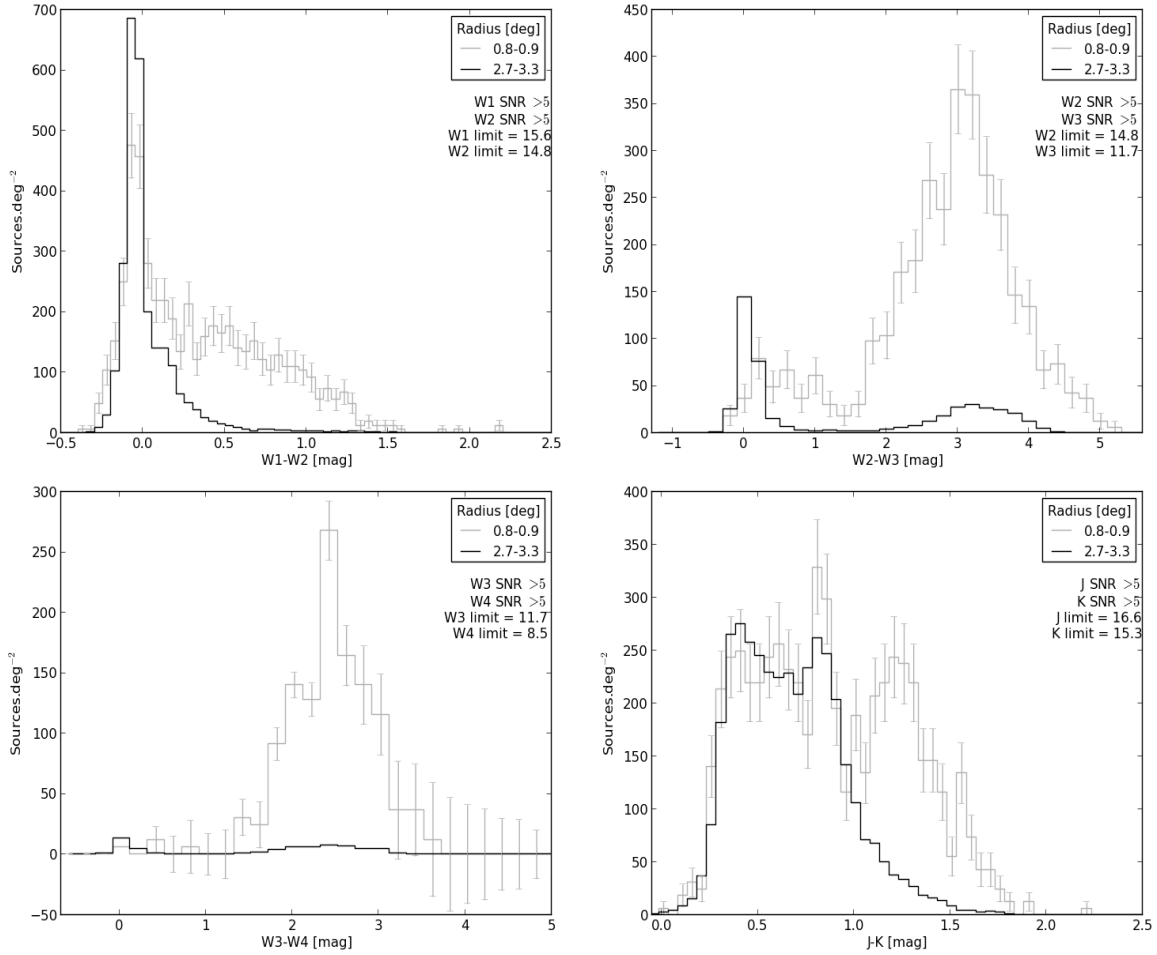

Figure 2.5: The W1-W2, W2-W3, W3-W4 and J-K_s color distributions for shell 7.

is to be expected; M 31 sources are further away and thus only the more luminous (evolved giants) are seen, which are redder in color compared to the Main Sequence population. Moreover, detections that are dominated by ISM emission (e.g., HII regions and star-forming sites) will have much redder colors, none of which are expected for the foreground MW population which is well above the plane of the MW where evolved giants are mostly confined (glon $\sim 11°$, glat $\sim 41°$). However, background galaxies are also red, and these are seen in the distributions of the defined foreground population. For example, sources with W2-W3 colors between $\sim$2 and $\sim$4 mag for the MW distribution ($2.7° \leq a \leq 3.3°$, Fig. 2.5) are expected to be background galaxies from their number densities (Jarrett et al., 2011).

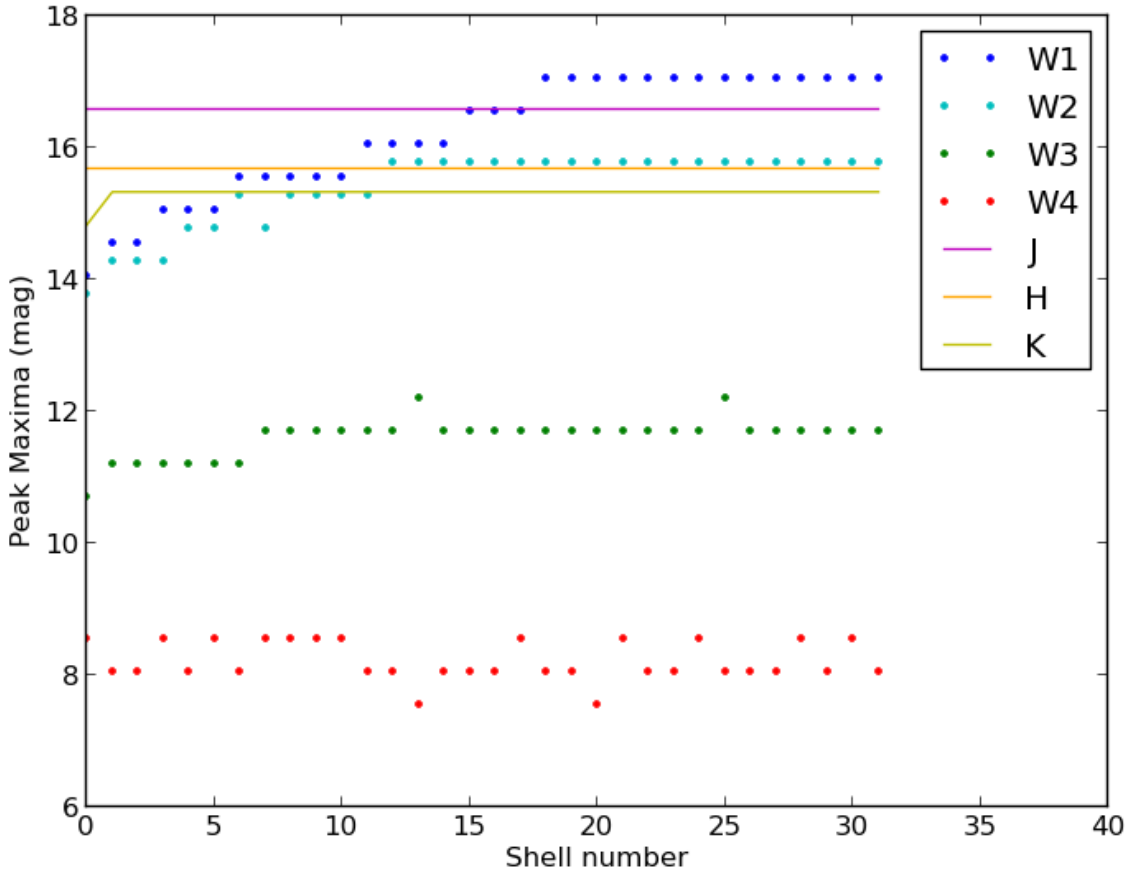

Figure 2.6: Magnitudes at which the LogN-LogS source counts peak, for each band, as a function of shell number.

Table 2.3: Magnitudes at which the LogN-LogS source counts peak.

Shell no.	W1 [mag]	W2 [mag]	W3 [mag]	W4 [mag]	J [mag]	H [mag]	K_s [mag]
0	14.05	13.78	10.71	8.54	16.57	15.68	14.83
1	14.55	14.28	11.21	8.04	16.57	15.68	15.33
2	14.55	14.28	11.21	8.04	16.57	15.68	15.33
3	15.05	14.28	11.21	8.54	16.57	15.68	15.33
4	15.05	14.78	11.21	8.04	16.57	15.68	15.33
5	15.05	14.78	11.21	8.54	16.57	15.68	15.33
6	15.55	15.28	11.21	8.04	16.57	15.68	15.33
7	15.55	14.78	11.71	8.54	16.57	15.68	15.33
8	15.55	15.28	11.71	8.54	16.57	15.68	15.33
9	15.55	15.28	11.71	8.54	16.57	15.68	15.33
10	15.55	15.28	11.71	8.54	16.57	15.68	15.33
11	16.05	15.28	11.71	8.04	16.57	15.68	15.33
12	16.05	15.78	11.71	8.04	16.57	15.68	15.33
13	16.05	15.78	12.21	7.54	16.57	15.68	15.33
14	16.05	15.78	11.71	8.04	16.57	15.68	15.33
15	16.55	15.78	11.71	8.04	16.57	15.68	15.33
16	16.55	15.78	11.71	8.04	16.57	15.68	15.33
17	16.55	15.78	11.71	8.54	16.57	15.68	15.33
18	17.05	15.78	11.71	8.04	16.57	15.68	15.33
19	17.05	15.78	11.71	8.04	16.57	15.68	15.33
20	17.05	15.78	11.71	7.54	16.57	15.68	15.33
21	17.05	15.78	11.71	8.54	16.57	15.68	15.33
22	17.05	15.78	11.71	8.04	16.57	15.68	15.33
23	17.05	15.78	11.71	8.04	16.57	15.68	15.33
24	17.05	15.78	11.71	8.54	16.57	15.68	15.33
25	17.05	15.78	12.21	8.04	16.57	15.68	15.33
26	17.05	15.78	11.71	8.04	16.57	15.68	15.33
27	17.05	15.78	11.71	8.04	16.57	15.68	15.33
28	17.05	15.78	11.71	8.54	16.57	15.68	15.33
29	17.05	15.78	11.71	8.04	16.57	15.68	15.33
30	17.05	15.78	11.71	8.54	16.57	15.68	15.33
31	17.05	15.78	11.71	8.04	16.57	15.68	15.33

2.3 Classification of foreground sources

Applying the scheme in Sect. 2.1, foreground sources can be statistically identified and separated from the M 31 population using their proximity to the center of the galaxy, their WISE and 2MASS fluxes, and their colors. It is of interest to define the likelihood that a source in shell i and bin n (see Fig. 2.4 and 2.5, Sect. 2.2) is a Milky Way (foreground) source given the features $D_1, ..., D_n$. The features, in this case, are the WISE fluxes (W1,W2, W3 and W4); the 2MASS fluxes (J, H and K_s); and colors W2-W3, W3-W4 and J-K_s of the source. WISE color W1-W2 was not used here as using W1-W2 colors gives results biased towards W1 likelihoods (see Sect. 2.4).

Examining the different source count densities in the different shells (Sect. 2.2), the likelihood that a source is part of the foreground population is defined as

$$p(MW|D_j) = \frac{N_{n_{MW}}}{N_{n_i}} \tag{2.3}$$

where N_{n_i} is the number density for a source in shell number i and magnitude bin n and $N_{n_{MW}}$ is the corresponding density for a foreground source ([Sources.deg^{-2}.mag^{-1}] for the fluxes and [Sources.deg^{-2}] for the colors). If the source's semi-major axis is less than 0.2°, $P(MW|D)$ is set to 0.0 (i.e sources in this region are assumed to be M 31 in origin). This is because the Galactic population in this region is blended with the M 31's population; and so, will be dealt with in a different manner (see section Sect. 2.4.1). Conversely, if the source's semi-major axis is greater than 2.7°, then $P(MW|D_j) = 1.0$ (sources in this region are all considered to be Galactic sources, see Sect. 2.2). If $N_{n_i} \leq N_{n_{MW}}$, then $p(MW|D_j) > 1.0$; therefore, the probability is set to 1.0, i.e., the source is assumed to be Milky Way. The foreground distribution, as described in Sect. 2.2.2, is represented by sources in semi-major axis range 2.7°-3.3°, i.e., $N_{n_{MW}} = N_{n_{31}}$.

For improved robustness, that takes into account measurement errors, the probabilities for the data are combined using different weights to statistically identify sources as either foreground or belonging to the galaxy:

$$
\begin{aligned}
P(MW|D_1,...,D_n) &= \sum_{j=1}^{10} w_j \times p(MW|D_j) \\
&= w_{W1} \times p(MW|D_{W1}) + w_{W2} \times p(MW|D_{W2}) \\
&+ w_{W3} \times p(MW|D_{W3}) + w_{W4} \times p(MW|D_{W4}) \\
&+ w_J \times p(MW|D_J) + w_H \times p(MW|D_H) \\
&+ w_{K_s} \times p(MW|D_{K_s}) + w_{W2-W3} \times p(MW|D_{W2-W3}) \\
&+ w_{W3-W4} \times p(MW|D_{W3-W4}) + w_{J-K_s} \times p(MW|D_{J-K_s}) \qquad (2.4)
\end{aligned}
$$

The weights, w_j, correspond to the confidence in the likelihoods. Therefore, to optimize the classification scheme, they must be related to the signal-to-noise ratio for each feature:

$$
w_j = \frac{(SNR_j)^\alpha}{\sum_i^{10} (SNR_i)^\alpha}. \qquad (2.5)
$$

The value of alpha is chosen in order to optimize the results (see Sect. 2.4). If any D_j is not available for a source (SNR < 5 or reduced chi$^2 < 2$, see Sect 2.2.1), its weight is set to $w_j = w_j/2$ and its likelihood set to 0 (which still means it is used, but it is much more likely to be M 31 since the faintest sources predominantly arise from M 31). The weights are then re-normalised. As stated in Sect. 2.1, the probability metric (2.4) is compared to the assigned random number. If $ran(u) \leq P(MW|D_1,...,D_n)$, then the source is identified as part of the foreground population; and if $ran(u) > P(MW|D_1,...,D_n)$, then the source is identified as part of the galaxy's population.

The classification algorithm is summarized below:

1. The likelihood of feature D_j for the source is calculated using Eq. 2.3.
2. The weight of the likelihood is calculated using Eq. 2.5, and then multiplied to the likelihood.
3. If feature D_j is not available for the source, the weight is set to half it value, and the likelihood is set to 0, i.e. an M 31 source.
4. Steps 1 to 3 are repeated for each D_j.
5. The total probability is calculated using Eq. 2.4.
6. If the semi-major axis of the source is less than 0.2°, the total probability is set to 0, if it is greater than 2.7°, the probability is set to 1.

7. The total probability is compared to a generated random number, ran(u) $\in$ [0,1], if the random number is lower, the source is classified as MW, if it higher, the source is classified as M 31.

8. Steps 1 to 7 are repeated for all the sources. Two lists are compiled; one for MW sources and the other for M 31 sources.

9. Visual inspection is used to further identify any bright (saturated) sources and resolved background galaxies.

2.4 Statistical results

In order to select the optimal combination of flux and color metrics to use for classification, the following combinations are assessed:

1. W1, W2 and W3
2. W1, W2, W3 and W4
3. W1, W2, W3, W4, W2-W3, W3-W4
4. W1, W2, W3, W4, W2-W3, W3-W4, J, H, K_s and J-K_s

The magnitude and color combinations were assessed with (1) equal weighting and (2) signal-to-noise weighting (Eq. 2.5). The results of the classification scheme obtained for each combination were then used to create the W1, W2, W3 and W4 source number densities (Figures A.1 to A.3) for the MW sources and M 31 sources. This was done in order to discern whether the foreground in each shell is adequately characterized, for each combination, by comparing it to the expected foreground distribution ($2.7^\circ \leq a \leq 3.3^\circ$). The combination of features that resulted in the closest resemblance to the foreground distributions for all bands was chosen as the optimal classification method. This was found to be W1, W2, W3 and W4 fluxes; J, H and K_s fluxes; and W2-W3, W3-W4 and J-K_s colors (combination 4, with weighting, $\alpha = 1$). This is not surprising since combination 4 uses the most independent information to help assess the population type of the source.

For demonstration of the classification performance, the resultant distributions for shells 4 and 12 using this optimal combination, are shown in Figs 2.7 and 2.8. The MW sources are shown in cyan and the M 31 sources in magenta. Shell 4 ($0.5^\circ \leq a \leq 0.6^\circ$) shows the distribution of sources far enough away from the center (confusion), but still well inside M 31's influence and thus should be dominated by the M 31 disk population. Shell 12 ($1.3^\circ \leq a \leq 1.4^\circ$), on the other hand, shows the distribution in transition between predominantly M 31 sources and foreground sources.

In shell 4, the W1 and W2 bands reliably identify the brighter MW sources (W1, W2 < 14 mag). However, due to WISE incompleteness at the faint end, the total number of sources drops off for W1, W2 > 14 mag, and the MW distribution is not as well characterized because MW sources are blended with M 31 sources, see Sect. 2.2.2. The W3 distribution shows slight overestimations ($\sim$10%) for W3 < 11 mag, as well as underestimations at the faint end by about the same amount ($\sim$11%). MW sources are also overestimated for the W4 distribution, by about 13%. It should be kept in mind that the W3 and W4 bands contain only about 40% and 20%, respectively, of the sources in W1, therefore, the overestimations of the MW distributions seen in the W3 and W4 bands are small compared to the large sample of W1 (and W2) sources. Shell 4 is a good representation of the inner shells, which are affected more so by incompleteness, therefore, the more sensitive W1 and W2 bands underestimate the foreground distributions at the faint end to a greater extent.

Shell 12 shows consistent characterization of the MW distribution for all four bands but still shows some incompleteness for the W1 band at fainter magnitudes (W1$<$ 16 mag). This shell is a good representation of the outer shells, which are further away from the center (lower source density), and hence their foreground distributions are more cleanly characterized.

Signal-to-noise weighting gives better results overall for W1, W2, W3 and W4. The value of α (Sect. 2.3) was chosen to be 1 so that W1 (the most sensitive band) is not overly weighted. Moreover, combination 4 was chosen as it was sufficiently not biased towards W1 likelihoods (by underestimating W2 and W3 source number densities; combination 1 and 2); and due to the addition W2-W3, W3-W4 and J-K_s colors, the W3 and W4 source number densities are underestimated less than the other cases (combination 1, 2 and 3).

The slight underestimations of the MW distributions for W1, W2 and W3 (due to incompleteness in the inner shells at faint end) and the slight overestimations for the W3 and W4 distributions (low number statistics due to the low sensitivity of WISE in these bands) will likely affect the total flux density calculations by only a few percent.

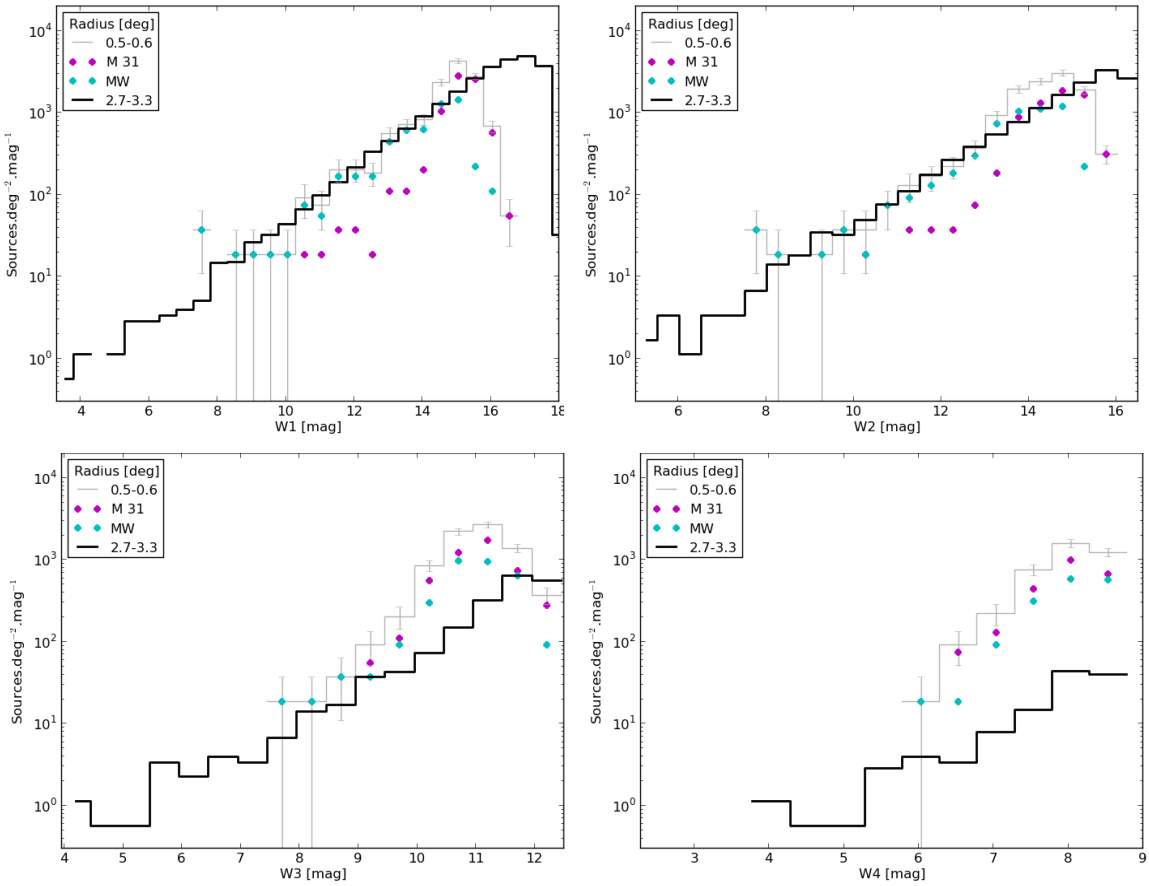

Figure 2.7: The resultant W1, W2, W3 and W4 MW source number density distributions (cyan points) for shell 4 (0.5°-0.6°) compared to the defined foreground distribution (black line). The W3 and W4 MW distributions are only overestimated by about 10% and 13%, respectively. The M 31 source number density distribution is shown in magenta.

Using combined probabilities for identifying foreground sources with WISE and 2MASS luminosities and colors shows consistent results. A uniform distribution of foreground sources is seen, as would be expected, up to the point where the galaxy itself is concealing the fainter foreground stars (due to its high surface brightness, Figure 2.9). As expected, a cluster of M 31 sources in the region of the galaxy is seen and a decrease of M 31 sources outward as the galaxy becomes invisible due to the exponential decline in the stellar source density (Figure 2.10). Bright sources are classified as Galactic, as expected even with small number statistics at the bright end. This was done by optimizing the weights using signal-to-noise weighting.

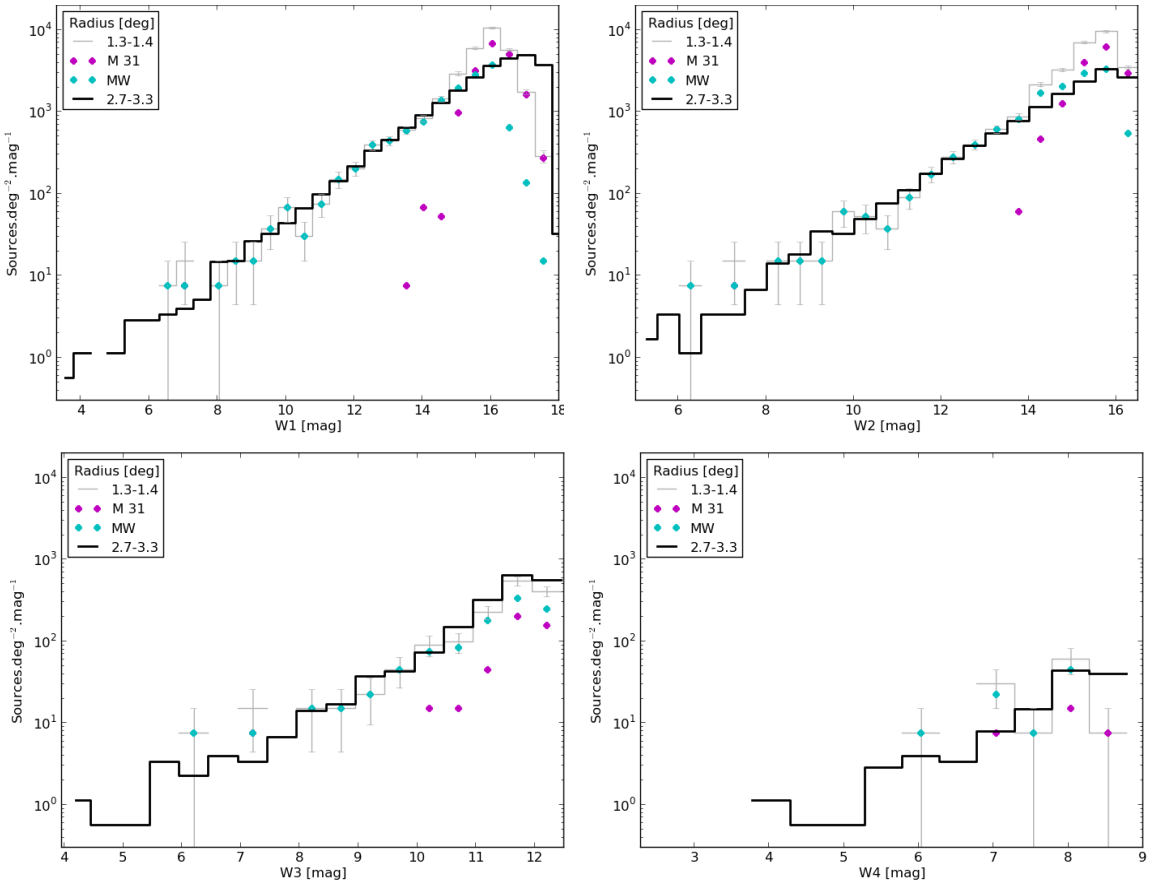

Figure 2.8: Resultant W1, W2, W3 and W4 MW source number density distributions (cyan points) for shell 12 (1.3°-1.4°) compared to the defined foreground MW distribution (black line). The M 31 source number density distribution is shown in magenta.

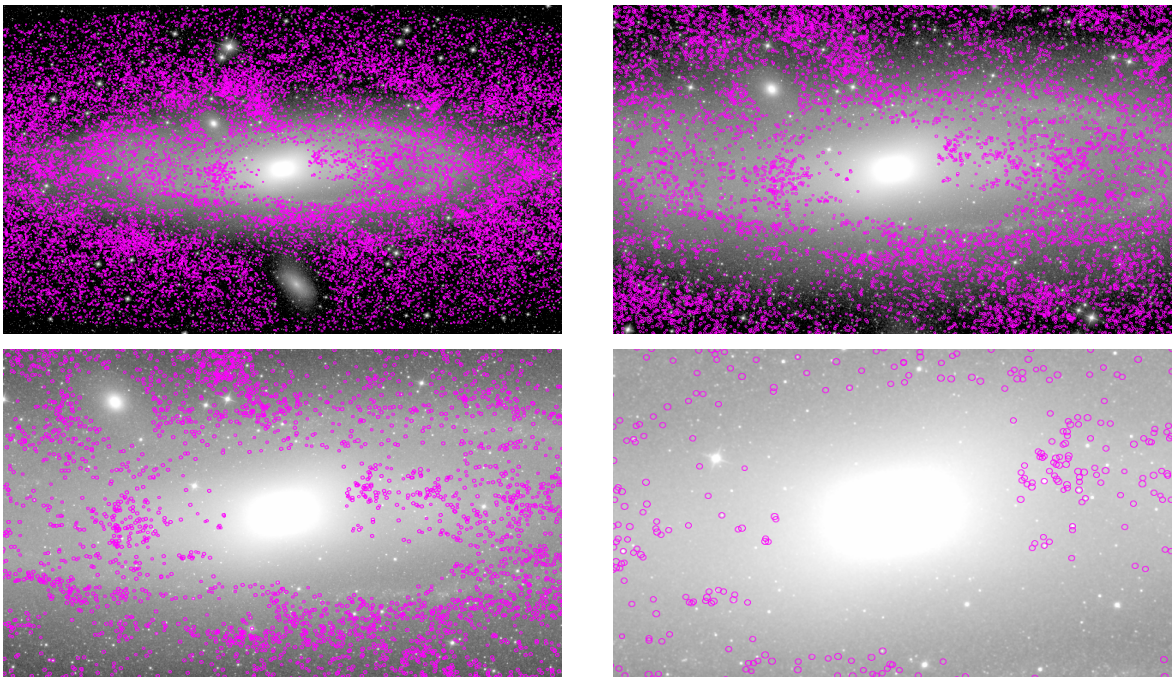

Figure 2.9: The top-left panel shows classified M 31 sources (magenta) overlaid on the WISE image of M 31. Subsequent panels are the zoomed-in versions of the image.

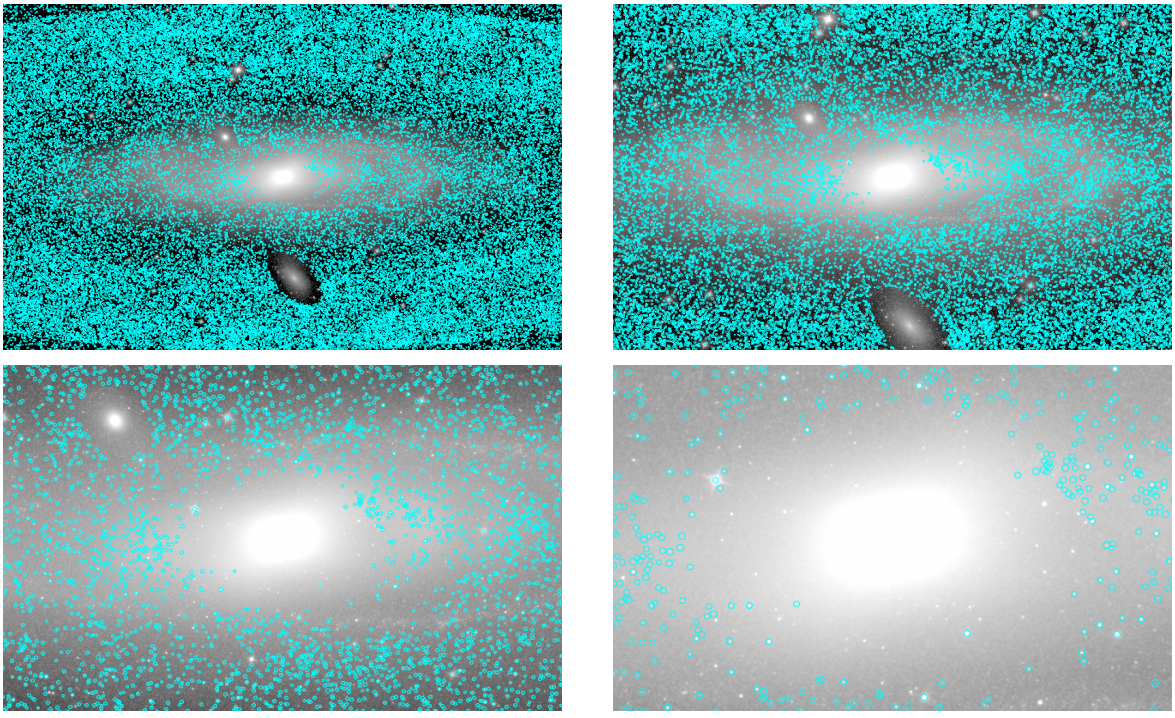

Figure 2.10: The top-left panel shows classified foreground sources (cyan) overlaid on the WISE image of M 31. Beyond $a = 2.7$, all sources are considered to be part of the foreground MW (Sect. 2.2.2). Bright saturated sources are not circled but are assumed to be MW in origin. Subsequent panels are the zoomed-in versions of the image.

2.4.1 Assessing the Photometric Incompleteness

Since MW sources in the innermost shells are underestimated at the faint end for W1, W2 and W3, due to source blending and incompleteness, and overestimated for W3 and W4, due to low number statistics as a consequence of the low sensitivity of WISE in these bands, the integrated flux densities that are computed after the MW sources have been subtracted from the images will require small corrections. To assess the flux disparities, the difference between the designated foreground source density distribution ($2.7^\circ - 3.3^\circ$) and the classified foreground distribution (see Sect. 2.4) is calculated for each magnitude bin and added up in each shell (Fig 2.11). Underestimation of the foreground is only seen in the inner shells ($a < 1.2^\circ$) for the W1 and W2 bands. Shell 0, for example, has an area of about 0.04°, so a difference in flux of 3.4 Jy/deg^2 in W1, only amounts to a total flux correction of 0.1 Jy, which is less than 1% of the integrated MW W1 flux.

For the W3 and W4 bands, an overestimation of the foreground contribution for $a < 0.9^\circ$ is seen, whereas, like W1 and W2, W3 is overestimated for $a > 1.3^\circ$. After about 1.7°, the differences between the distributions converge to 0, showing that in these outer regions, the MW is well characterized by the classification scheme. The flux differences are added in each shell up until 2.7° (the expected foreground) for each band in Table 1.4 revealing that 2.84 Jy, 0.70 Jy and 0.02 Jy need to be subtracted from the total M 31 flux in the W1, W2 and W3 bands respectively; and 2.18 Jy needs to be added back to the M 31 integrated flux in the the W4 band. Using the previous 3.6 μm measurement of 256 Jy (Barmby et al., 2006), and comparing it to W1, this would amount to a $\sim$1% correction to the flux. Since the W1 flux is expected to be similar to previous measurements, the flux corrections are expected to only affect the flux densities by only a few percent (similar corrections are expected for the other bands as well).

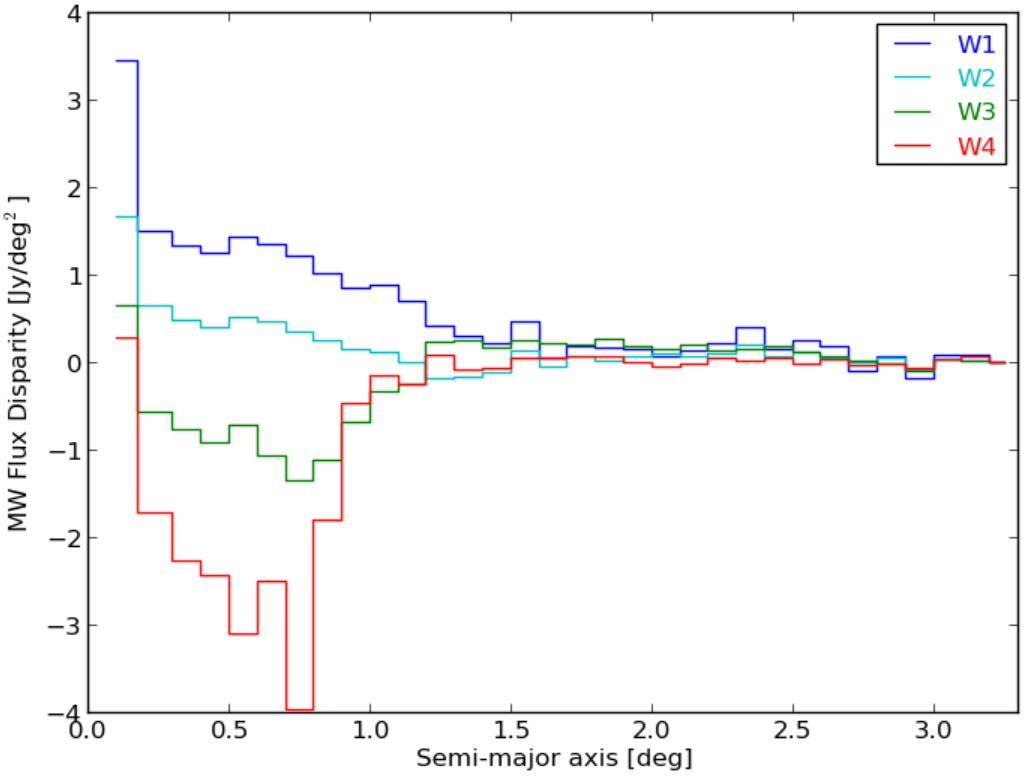

Figure 2.11: Difference between the expected foreground ($2.7° - 3.3°$) and the classified foreground in each shell. Under-estimation of the foreground is seen in the inner shells ($a < 1.2°$) for the W1 and W2 bands and for the W3 and W4 bands, overestimation of the foreground is seen for $a < 0.9°$. These disparities are all very small (<2%) compared to the integrated flux of M 31.

Table 2.4: Departure from the MW Flux in each M 31 shell

Shell	Radius [°]	Area [deg^2]	W1 Sources	W1 Flux [Jy]	W2 Sources	W2 Flux [Jy]	W3 Sources	W3 Flux [Jy]	W4 Sources	W4 Flux [Jy]
(1)	(2)	(3)	(4)	(5)	(6)	(7)	(8)	(9)	(10)	(11)
0	0.15	0.040	495	0.137	258	0.066	34	0.026	2	0.011
1	0.25	0.050	534	0.081	249	0.036	-13	-0.028	-11	-0.076
2	0.35	0.070	736	0.081	334	0.032	-26	-0.052	-29	-0.143
3	0.45	0.090	911	0.111	390	0.036	-49	-0.094	-47	-0.230
4	0.55	0.109	1097	0.136	459	0.044	-45	-0.092	-75	-0.430
5	0.65	0.127	1249	0.181	516	0.057	-83	-0.131	-74	-0.382
6	0.75	0.145	1287	0.174	472	0.049	-108	-0.170	-98	-0.525
7	0.85	0.164	1470	0.155	533	0.033	-156	-0.195	-59	-0.290
8	0.95	0.185	1559	0.157	494	0.032	-123	-0.131	-10	-0.063
9	1.05	0.208	1697	0.170	469	0.013	-66	-0.077	-11	-0.059
10	1.15	0.228	1848	0.164	497	0.003	-59	-0.080	-22	-0.097
11	1.25	0.248	1661	0.121	207	-0.040	101	0.062	4	0.012
12	1.35	0.268	1647	0.089	89	-0.042	101	0.064	2	-0.017
13	1.45	0.285	1700	0.070	105	-0.033	78	0.055	4	-0.007
14	1.55	0.302	1866	0.144	244	0.045	129	0.073	5	0.016
15	1.65	0.321	1297	0.019	156	-0.010	145	0.080	5	0.024
16	1.75	0.340	1438	0.066	225	0.024	140	0.074	3	0.021
17	1.85	0.360	1490	0.062	195	0.009	166	0.101	7	0.023
18	1.95	0.380	724	0.064	237	0.028	137	0.074	-0	-0.000
19	2.05	0.399	772	0.023	266	0.037	125	0.059	-3	-0.017
20	2.15	0.420	829	0.061	164	0.026	142	0.085	2	-0.000
21	2.25	0.441	940	0.098	278	0.048	128	0.067	1	0.019
22	2.35	0.462	1015	0.183	309	0.093	141	0.071	1	0.002
23	2.45	0.486	967	0.076	185	0.032	142	0.089	5	0.021
24	2.55	0.506	1080	0.124	303	0.056	104	0.051	-0	-0.015
25	2.65	0.526	1117	0.092	200	0.027	75	0.038	6	0.015
TOTAL			31428	2.840	7837	0.702	1161	0.016	-396	-2.184

Notes. Columns 4, 6, 8 and 10 represent total number of MW sources missing in that shell for the W1, W2, W3 and W4 bands, respectively, and columns 5, 7, 9 and 11 represent the resultant flux corrections.

Chapter 3

M 33 Foreground Characterization

For efficiency and to develop the methodology of the removal of foreground sources for M 31, M 33 was used as a test galaxy. Consequently, the results obtained for the galaxy are shown in this chapter.

3.1 Characteristics of M 33 region

The Triangulum galaxy (M 33), one of the largest members of the local group (including M31 and the Milky Way), is a spiral galaxy that has been extensively observed across the electromagnetic spectrum. M33 is connected to M 31 via HI gas and stars (McConnachie et al., 2009), and is thought, by many, to be a satellite of M 31 (McConnachie et al., 2010). Its proximity to the Milky Way, like M 31, allows for it to be studied in detail; and its smaller size allows for its global properties to be more easily measured.

Before the classification method was implemented for M 31 (Sect. 2.2), it was first tested on M 33, which has also been observed by WISE (Fig. 3.1). This was done to investigate the reliability and efficiency of the classification method. The galaxy is much smaller than M 31 ($\sim 1^\circ$); it is also not as inclined and flattened (higher axis ratio); therefore, it makes for an easier analysis. However, it still offers a challenge to identify and separate Milky Way sources from M 33 sources.

The analysis carried out for M 33 was exactly the same as that for M31 (Sect. 2.3); with only sources with the criteria stated in Sect. 2.2 being considered. The region is divided into 20 elliptical shells centered on M 33 using the galaxy's axis ratio and position angle (Table 3.1 and Fig. 3.2). The semi-major axis for the innermost shell is 0.1° and subsequent semi-major axes increase by 0.1° with the outermost being 2.0° (with a total of 84084 sources).

The smooth transition from the M 33 analysis to M 31 shows that this statistical method

well suited for adaptation to machine-learning methods. The classification method can be translated to a more Bayesian-like analysis to improve the results, which would require quantifying the posterior probability that a source belongs to the galaxy concerned verses the MW. This, however, is beyond the scope of this work.

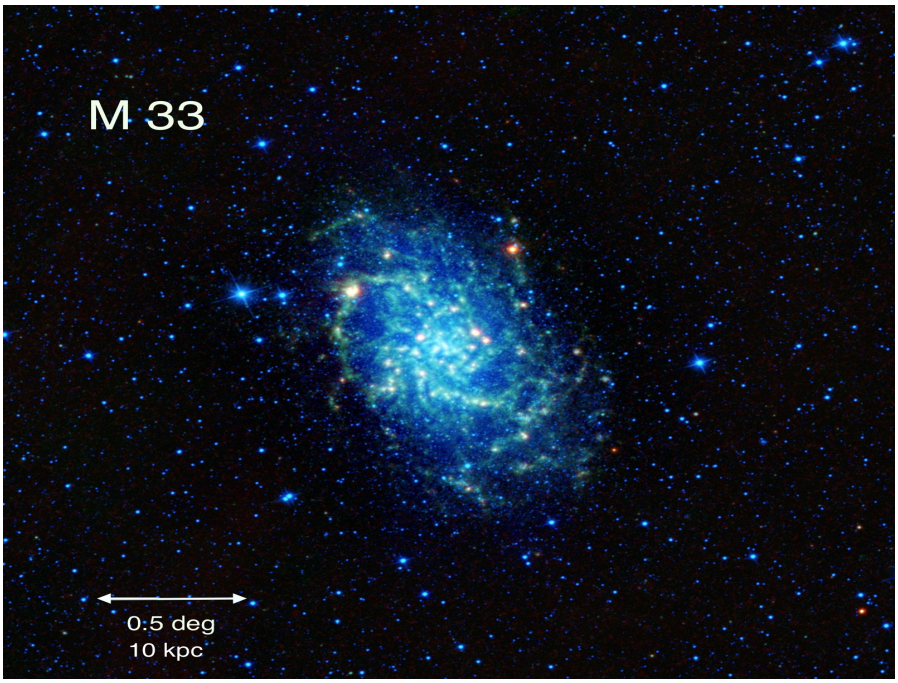

Figure 3.1: Composite image of M 33 with colors corresponding to WISE bands: 3.4μm (blue), 4.6μm (cyan), 12μm (green) and 22μm (red).

Table 3.1: Basic Parameters of M 33.

Parameter	Value
Right Ascension (J2000)	$01^h33^m50.9^s$ [a]
Declination (J2000)	$+30°39'36.8''$ [a]
Distance (Mpc)	0.883 ± 0.370 [b]
Inclination	5°
Position angle	23° [c]
Axial Ratio	0.615 ± 0.01 [d]

Notes. [a] Evans et al. (2010), [b] Tully et al. (2009), [c] Regan and Vogel (1994), [d] de Vaucouleurs (1959).

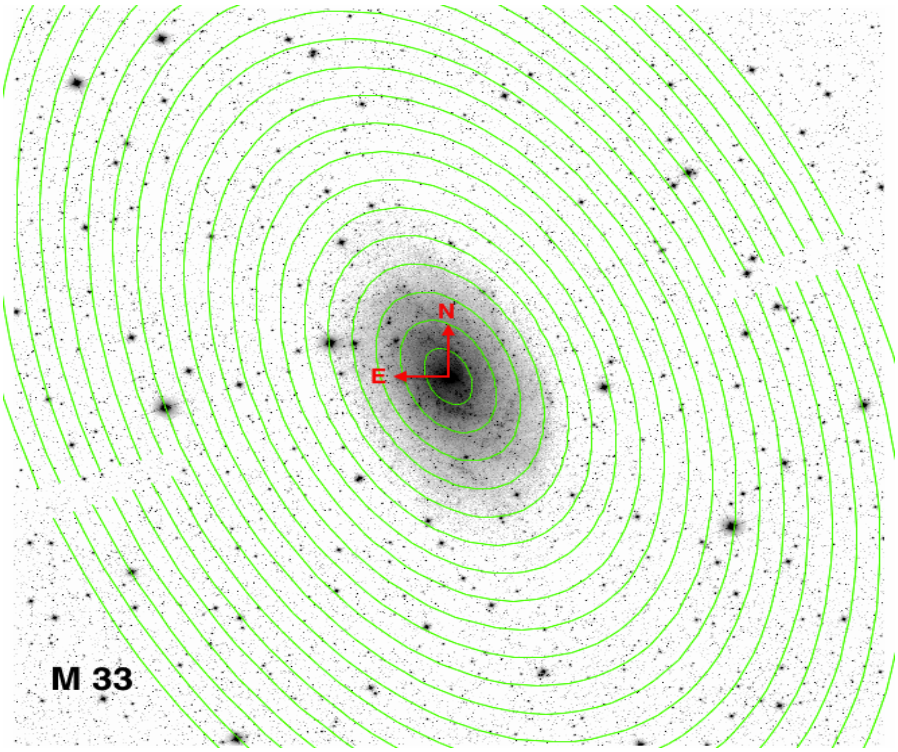

Figure 3.2: Elliptical shells centered on W1 image of M33 (innermost semi-major axis is 0.1°, outermost is 2.0°).

The axisymmetric W1 source counts plotted against the semi-major axis radius (Fig. 3.3), showing the source density distribution with respect to the center of M 33, with mean values computed within the elliptical shells, has similarities with those seen for M 31. The black solid line represents all W1 sources; faint sources ($15.5 < W1 < 16.5$) are represented by the dark-grey solid line, the intermediate range ($14.2 < W1 < 14.7$) is represented by the light-grey solid line, and bright sources ($12.0 < W1 < 12.5$), by the grey dashed line. The distribution of bright sources is fairly constant throughout (∼100 sources per square degree, as M 31), indicating that bright sources in the region are not correlated with proximity to M 33, and thus are almost exclusively Galactic. Sources in the intermediate brightness range show an overdensity in the inner regions ($a < 0.4°$) due to the presence of M 33 sources; after which, the source count converges to about 400 per square degree. In the faint regime, the source counts converge at a later stage ($a > 0.7°$) to about 3000 sources per square degree. However, the decrease in the source count distribution in the inner regions, due to incompleteness, is only seen in the faint regime ($a < 0.3°$).

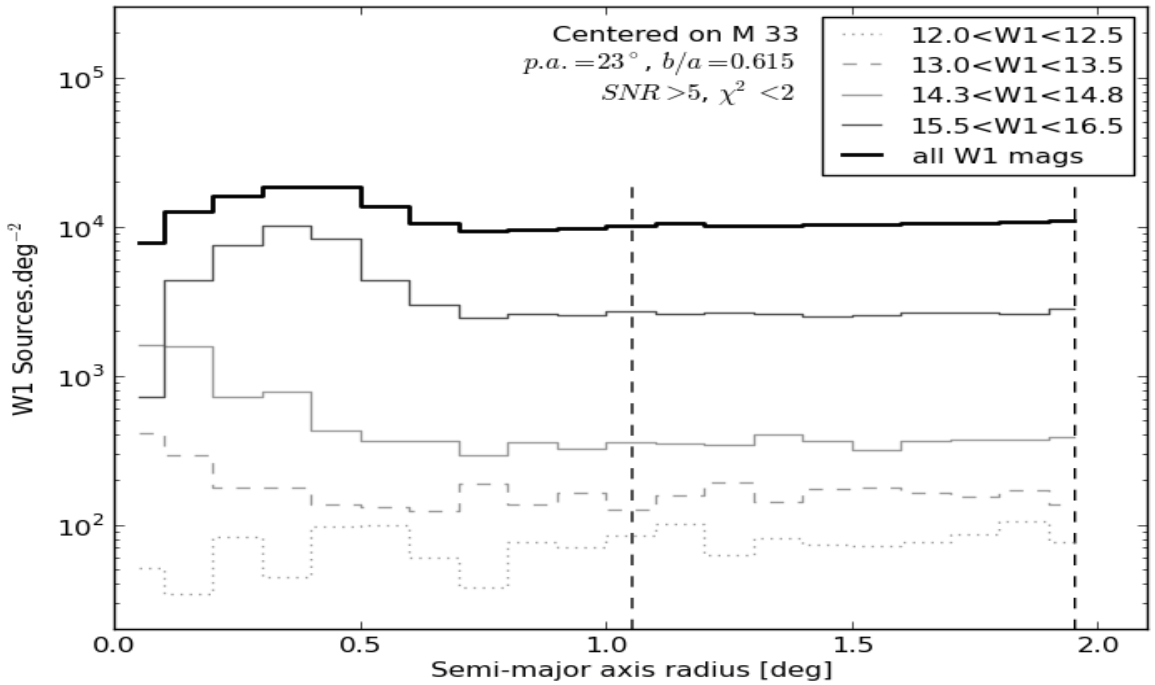

Figure 3.3: Axisymmetric W1 source counts as a function of radius from the center of M 33. Low, intermediate and high observed flux sources are represented by dark-grey, light-grey and light-grey dashed lines respectively. Outer bins converge to the expected Milky Way source level (vertical dashed black lines at 1.0° and 2.0°).

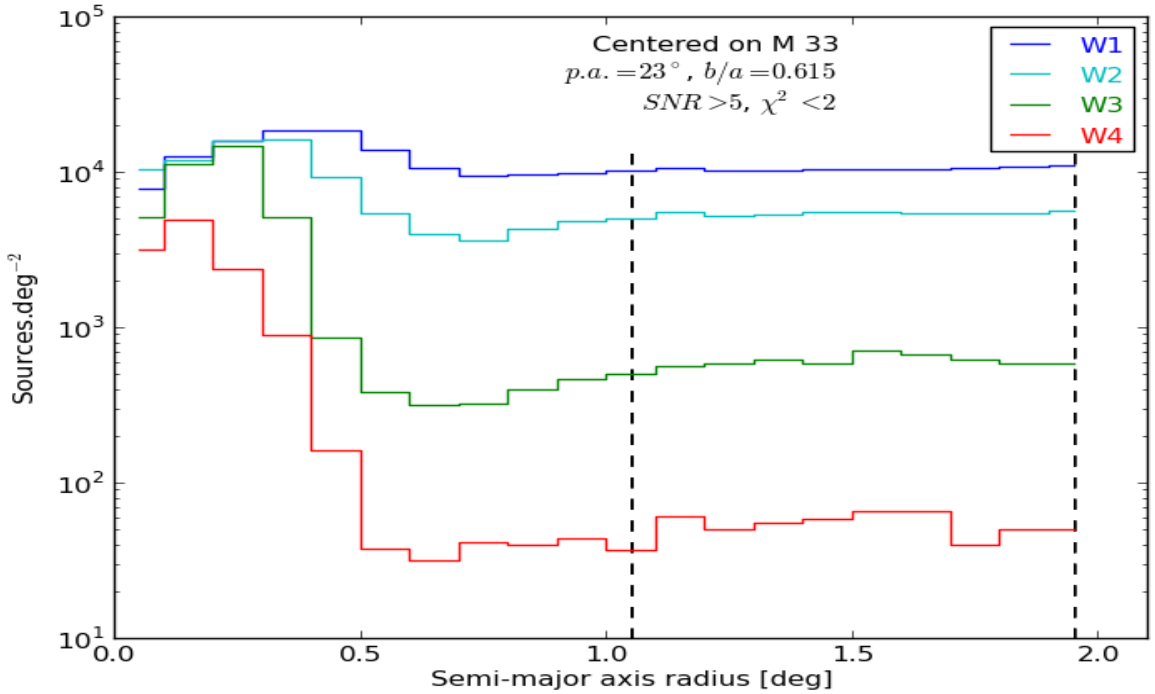

Figure 3.4: Axisymmetric W2, W3 and W4 source counts as a function of radius.

The WISE multi-band source counts plotted to verify that the distribution of sources at those wavelengths converge to a Milky Way level as well (Figure 3.3), also show similar trends. The source counts show confusion in the innermost regions, $a < 0.3°$, $a < 0.2°$ and $a < 0.1°$ for W2, W3, and W4 distributions, respectively. The distributions then flatten to Milky Way levels at about $a = 0.9°$, $a = 1.0°$ and $a = 0.9°$ for W2, W3, and W4, respectively. The W1, W2, W3, and W4 source count distributions are fairly flat for $1.0° \leq a \leq 2.0°$, indicated by the vertical dashed lines in Fig. 3.3 and 3.4, consistent with a Galactic distribution. Therefore, all sources in this semi-major axis range $(1.0° - 2.0°)$ are considered to be Milky Way sources. Sources with $a > 2.0°$ are considered to be part of the Galactic foreground and will not be included in the analysis. The W1, W2, W3 and W4 LogN-LogS differential source counts are shown for a representative 4 shells in Fig 3.5 and the W1-W2, W2-W3, W3-W4 and J-K color distributions for shell 2 are shown in Fig. 3.6.

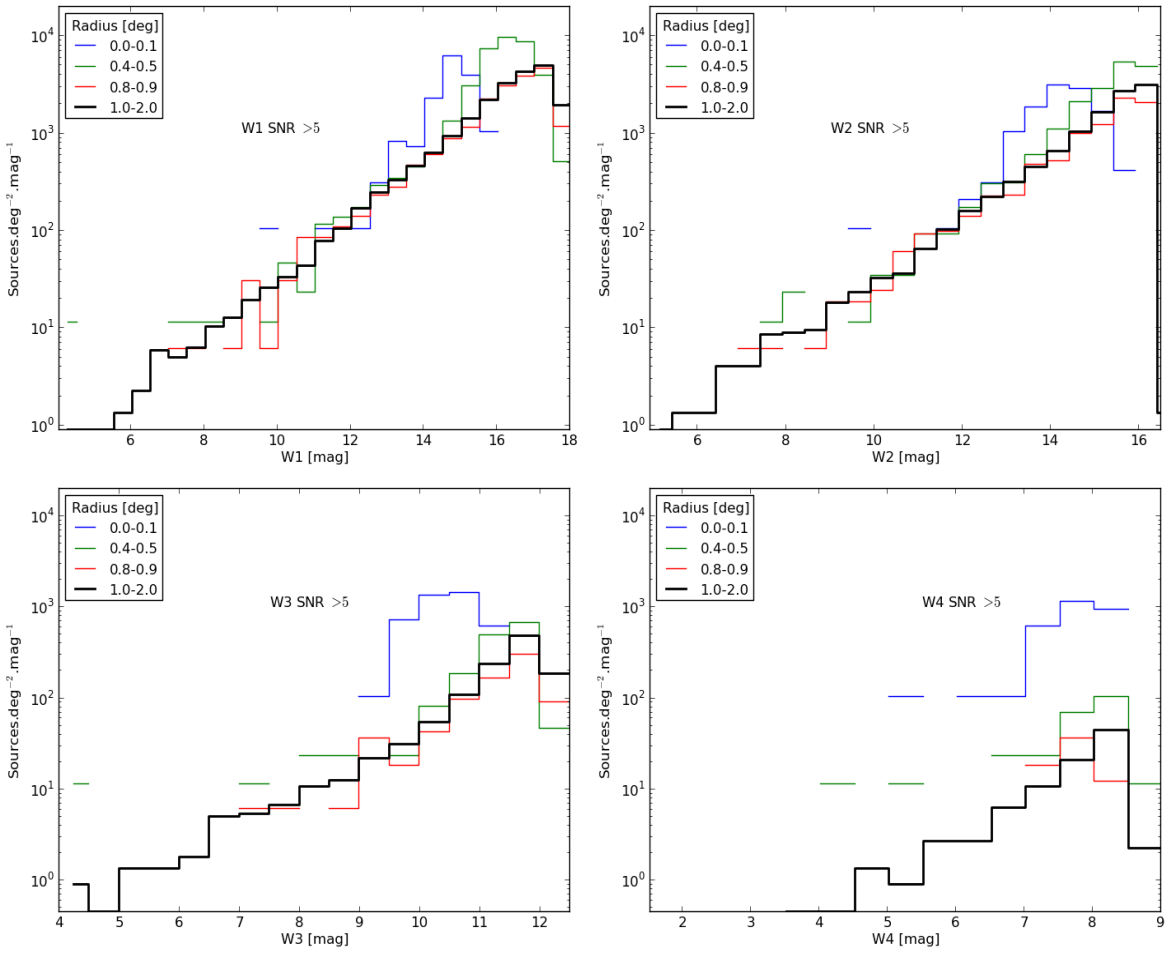

Figure 3.5: The W1, W2, W3 and W4 source number density distributions for a representative 4 shells.

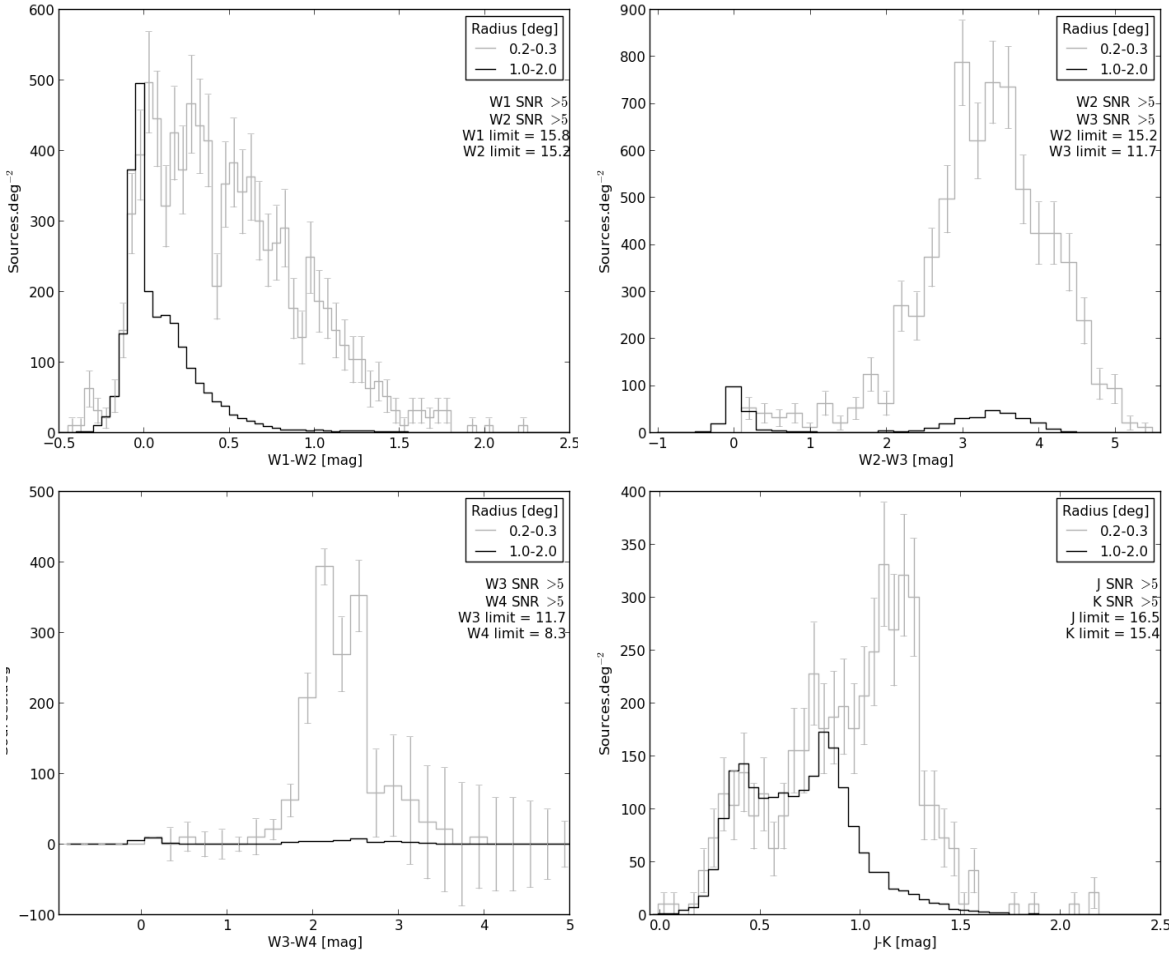

Figure 3.6: The W1-W2, W2-W3, W3-W4 and J-K color distributions for shell 2.

3.2 Statistical results

The statistical results using WISE fluxes W1, W2, W3, W4, WISE colors W2-W3 and W3-W4, 2MASS fluxes J, H, K, and 2MASS color J-K for each source with signal-to-noise weighting (combination 4, Sect. 2.4), are shown in Fig. 3.7 and 3.8 for shells 2 ($0.2^\circ \leq a \leq 0.3^\circ$) and 5 ($0.5^\circ \leq a \leq 0.6^\circ$), respectively. Shell 2 shows the distribution of sources far enough away from the center (where confusion dominates), but still well inside the galaxy and thus should be dominated by the M 33 population. Shell 5 shows the distribution in transition between dominantly M 33 sources and foreground sources (Fig. 3.2). As in M 31, the M 33 inner shells are affected more by incompleteness, allowing the W1 and W2 foreground distributions in the inner shells to be underestimated to a greater extent at the faint end (W1, W2> 15.5 for shell 2). The outer shells, which are further away from the center (lower source density), have their foreground distributions more cleanly characterized. Low number statistics in the W3 and W4 bands, due to the low sensitivity of WISE in these bands compared to the W1 and W2 bands, make these bands less affective in the classification scheme, causing the MW distributions in these

bands to be slightly overestimated, by about ∼10%, in the inner shells. Sources in these bands only represent about 40% of the W1 and W2 sources, therefore, these deviations are small compared to the entire sample.

Combined probabilities for identifying foreground sources with WISE and 2MASS luminosities and colors also show consistent results for M 33. As expected, a uniform distribution of Galactic sources is seen, up to the point where the galaxy conceals the fainter foreground stars (high surface brightness, Fig. 3.9). A cluster of M 33 sources in the region of the galaxy is seen (Figure 3.10) with an exponential decrease of M 33 sources outward as the galaxy becomes invisible due to the exponential decline in the stellar source density as seen in the axisymmetric sources counts (Fig. 3.3 and 3.4).

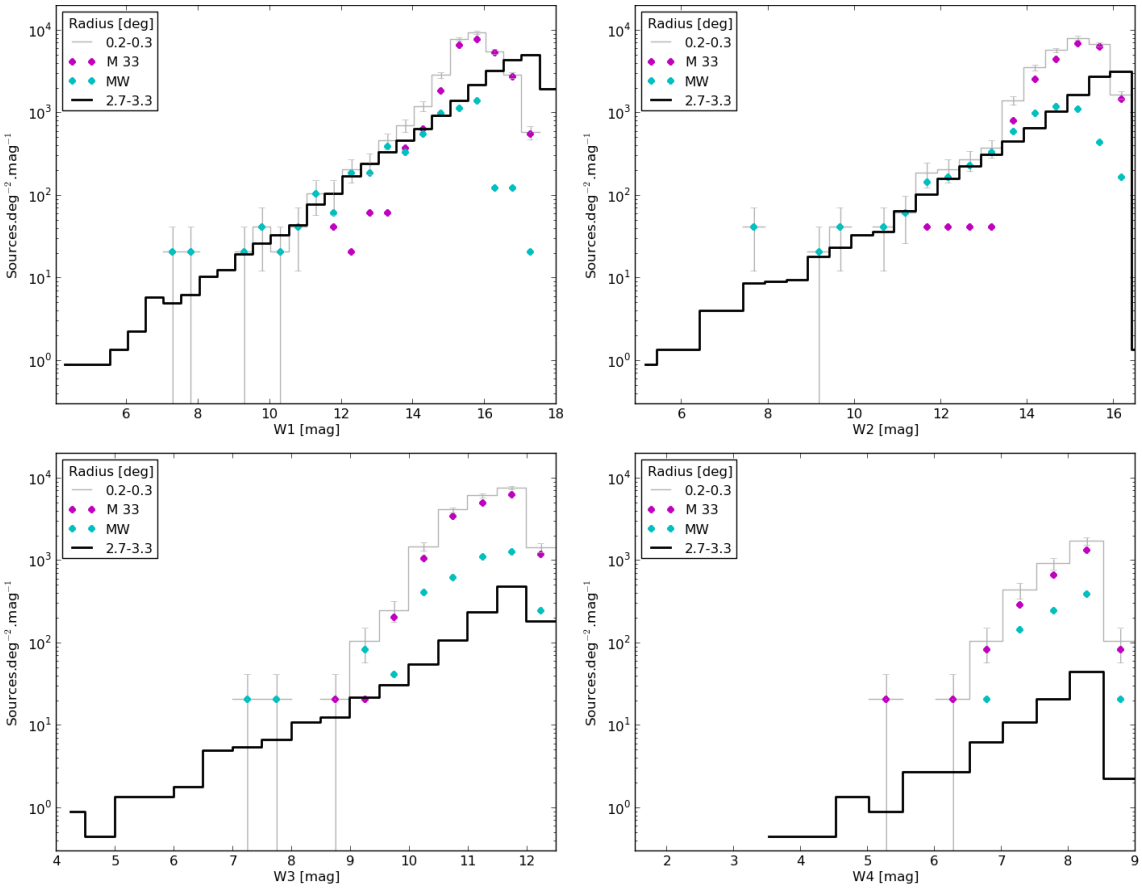

Figure 3.7: The resultant W1, W2, W3 and W4 MW source number density distributions (cyan points) for shell 2 (0.2°-0.3°) compared to the defined foreground distribution (black line). The M 33 source number density distribution is shown in magenta.

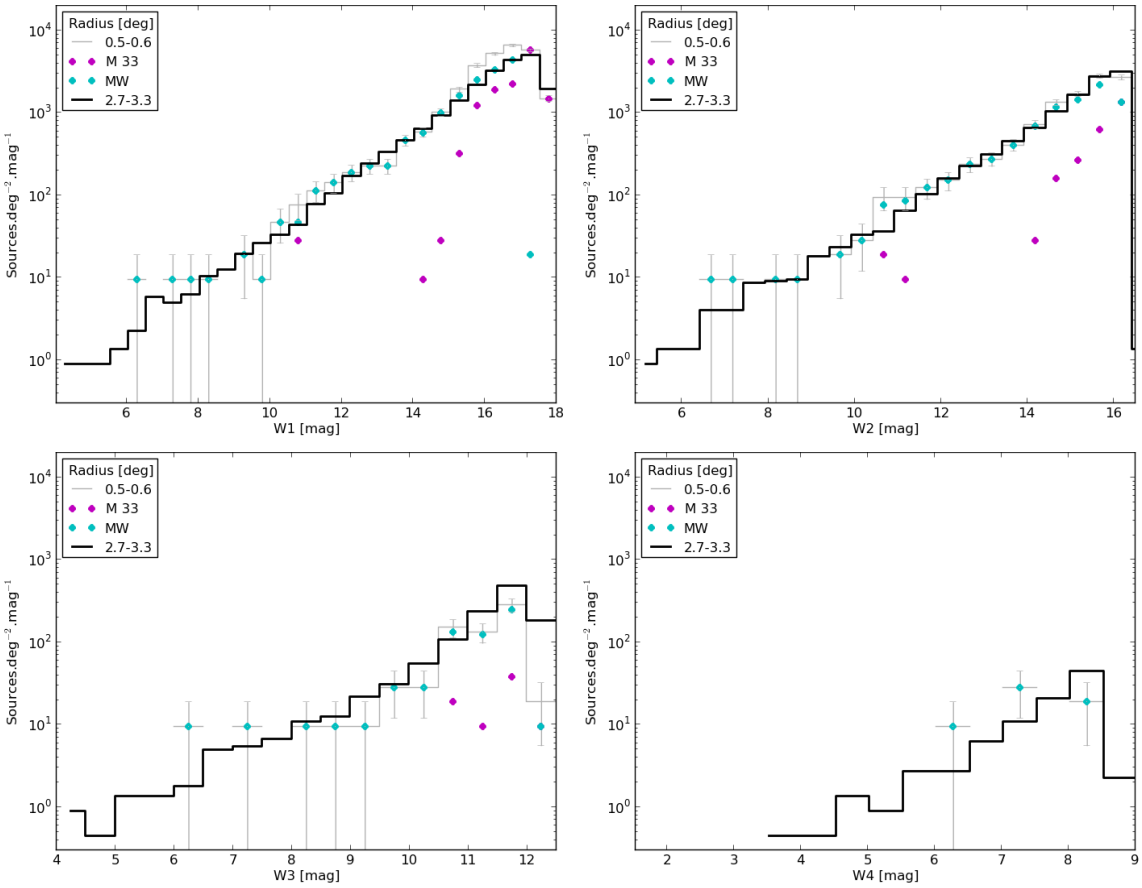

Figure 3.8: The resultant W1, W2, W3 and W4 MW source number density distributions (cyan points) for shell 5 (0.5°-0.6°) compared to the defined foreground distribution (black line). The M 33 source number density distribution is shown in magenta.

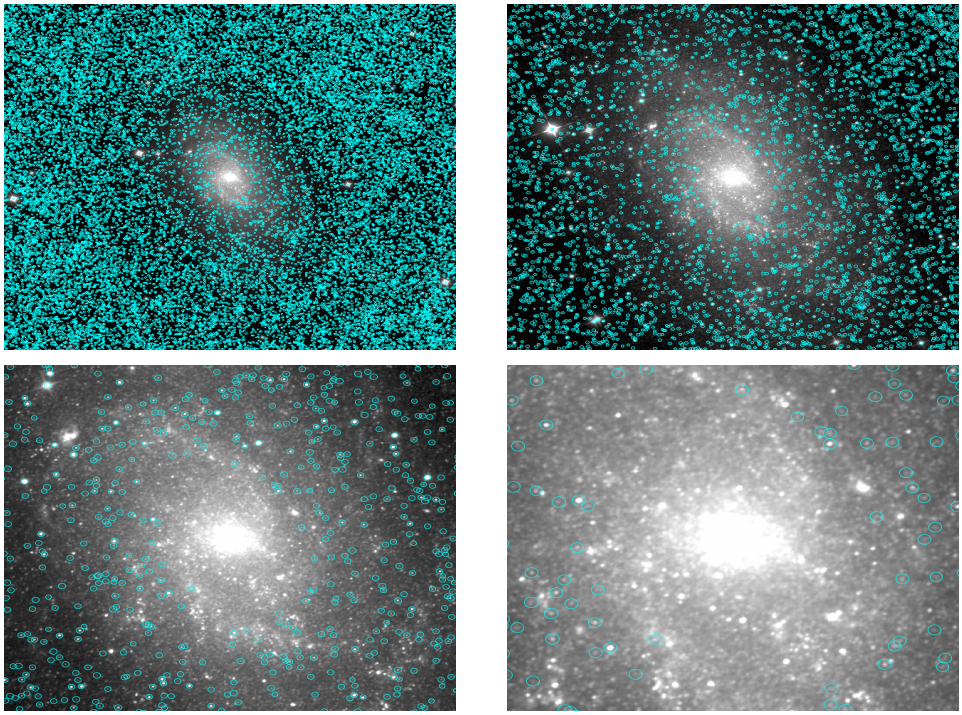

Figure 3.9: The top-left panel shows classified foreground sources (cyan) overlaid on the WISE image of M 33. Subsequent panels are the zoomed-in versions of the image.

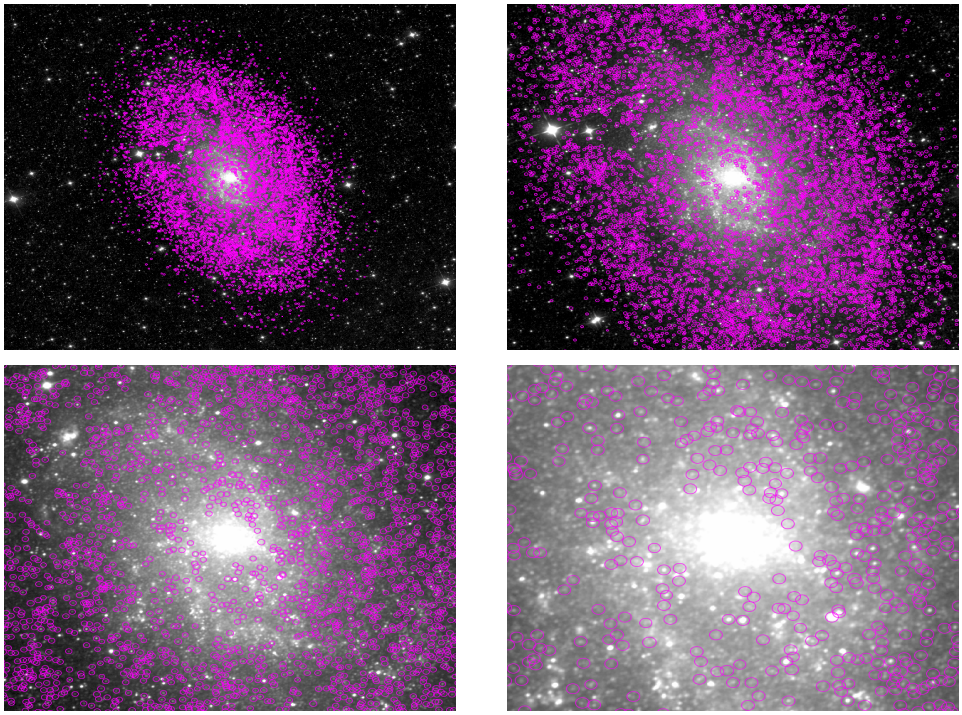

Figure 3.10: The top-left panel shows classified M 33 sources (magenta) overlaid on the WISE image of M 33. Bright saturated sources are not circled but are assumed to be MW in origin. Subsequent panels are the zoomed-in versions of the image.

3.2.1 Accounting for the M 33 Photometric Incompleteness

The deviation of the MW distributions in the inner shells compared to the defined foreground (underestimation, for W1 and W2, due to source blending and incompleteness, and overestimation, for W3 and W4, due to low number statistics as a consequence of the low sensitivity of WISE in these bands), slightly affects the measurements of the flux densities for M 33 in all four bands (∼3% flux correction, see Chapter 4). The correction for this is made by calculating the differences between the designated foreground source density distribution ($1.0° - 2.0°$) and the classified foreground distribution (see Sect. 3.2) for each magnitude bin and adding those up in each shell (Fig 3.11). The flux differences are added up until 1.0° (the defined foreground) for each band, shown in Table 1.2, revealing that 0.50 Jy and 0.29 Jy need to be subtracted from the total M 33 flux in the W1 and W2 bands, respectively; and 0.03 Jy and 0.50 Jy need to be added to M 33 flux in the the W3 and W4 bands, respectively.

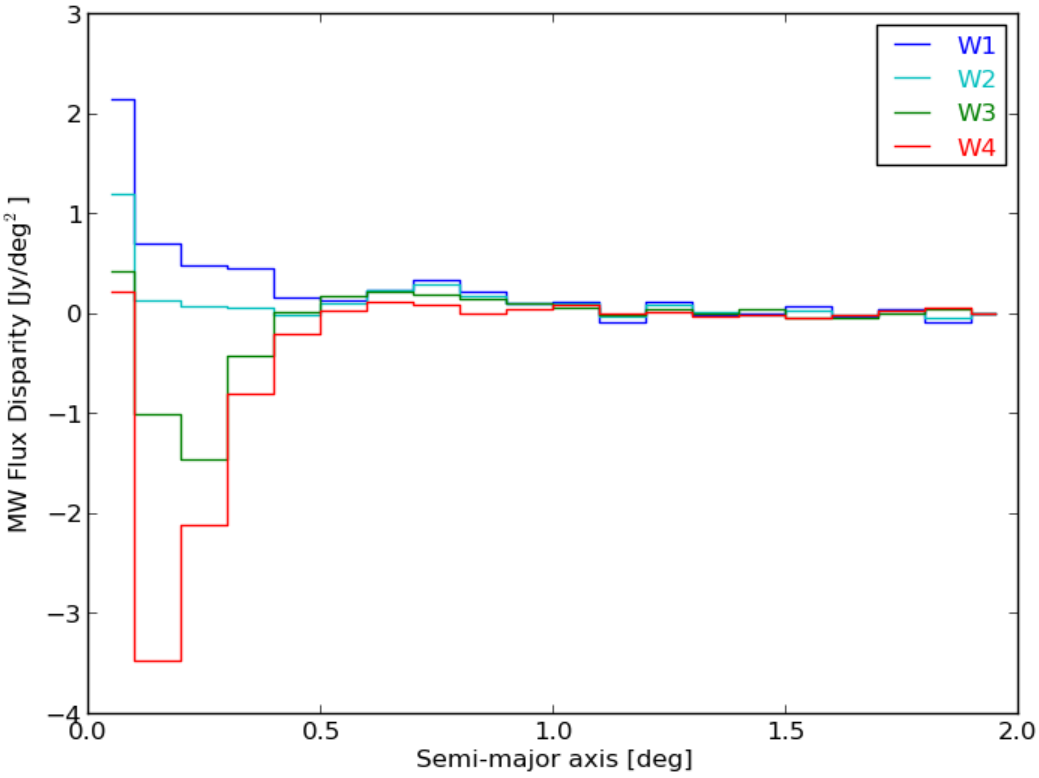

Figure 3.11: Difference between the defined foreground ($1.0° - 2.0°$) and the classified foreground in each shell. Underestimation of the foreground is seen in the inner shells ($a < 0.2°$) for the W1 and W2 bands with an opposite affect seen for the W3 and W4 bands, with an overestimation of the foreground for $a < 0.4°$. These disparities are all very small (∼3%) compared to the integrated flux of M 33.

Table 3.2: Departure from the MW Flux in each M 33 shell

Shell	Radius [°]	Area [deg^2]	W1 Sources	W1 Flux [Jy]	W2 Sources	W2 Flux [Jy]	W3 Sources	W3 Flux [Jy]	W4 Sources	W4 Flux [Jy]
(1)	(2)	(3)	(4)	(5)	(6)	(7)	(8)	(9)	(10)	(11)
0	0.05	0.019	201	0.041	98	0.022	10	0.008	1	0.004
1	0.15	0.058	448	0.034	158	0.006	-39	-0.058	-36	-0.204
2	0.25	0.096	724	0.044	236	0.005	-127	-0.135	-36	-0.220
3	0.35	0.135	888	0.053	189	0.002	-61	-0.061	-20	-0.112
4	0.45	0.173	922	0.030	213	-0.003	14	-0.002	-7	-0.033
5	0.55	0.213	742	0.036	277	0.024	59	0.036	3	0.006
6	0.65	0.251	305	0.056	409	0.057	75	0.055	5	0.027
7	0.75	0.290	544	0.096	545	0.083	78	0.051	3	0.023
8	0.85	0.328	601	0.070	425	0.056	61	0.042	2	-0.006
9	0.95	0.367	251	0.037	200	0.037	47	0.034	3	0.013
TOTAL			5625	0.500	2756	0.292	118	-0.028	-82	-0.503

Notes. Column 4, 6, 8 and 10 represent total number of MW sources missing in that shell for the W1, W2, W3 and W4 bands, respectively, and column 5, 7, 9 and 11 represent the resultant flux corrections.

Chapter 4

Results: Global Photometric Measurements

The resultant Galactic source-cleaned images (obtained from using the source characterization methods in Sect. 2.3) are shown Sect. 4.1, basic measurements for M 31 are shown in Sect. 4.2, and the results obtained are compared to ancillary results in Sect. 4.2.2. Results from the analysis of M 33 are also included.

4.1 Cleaned Images

Using the source characterization method discussed in Chapter 2, the M 31 region was cleaned of foreground sources. Sources were PSF-subtracted, using a region that captures over 99% of the light from the star (Jarrett et al., 2013). To determine the local background, some bright sources were masked and the pixels were replaced with local area averages, because of the large residuals from PSF subtraction. Then the background was estimated by the most common binned histogram value in the pixel value distribution in an annulus well outside the ellipse. In Fig. 4.1, the top panel shows the 3-color image of the M 31 region and the bottom panel shows the foreground source-cleaned W1 (left) and 3-color (right) images of M 31. Satellite galaxies M 32 and M 110 were masked from the images. The blue ellipse represents the W1 1-σ isophotal radius of M 31. The yellow annulus represents the area where the local background is determined, placed well outside the influence of the galaxy and estimated by the most common binned histogram value in the pixel value distribution in the annulus. The similarly cleaned images of M 33 are also shown in Fig. 4.2.

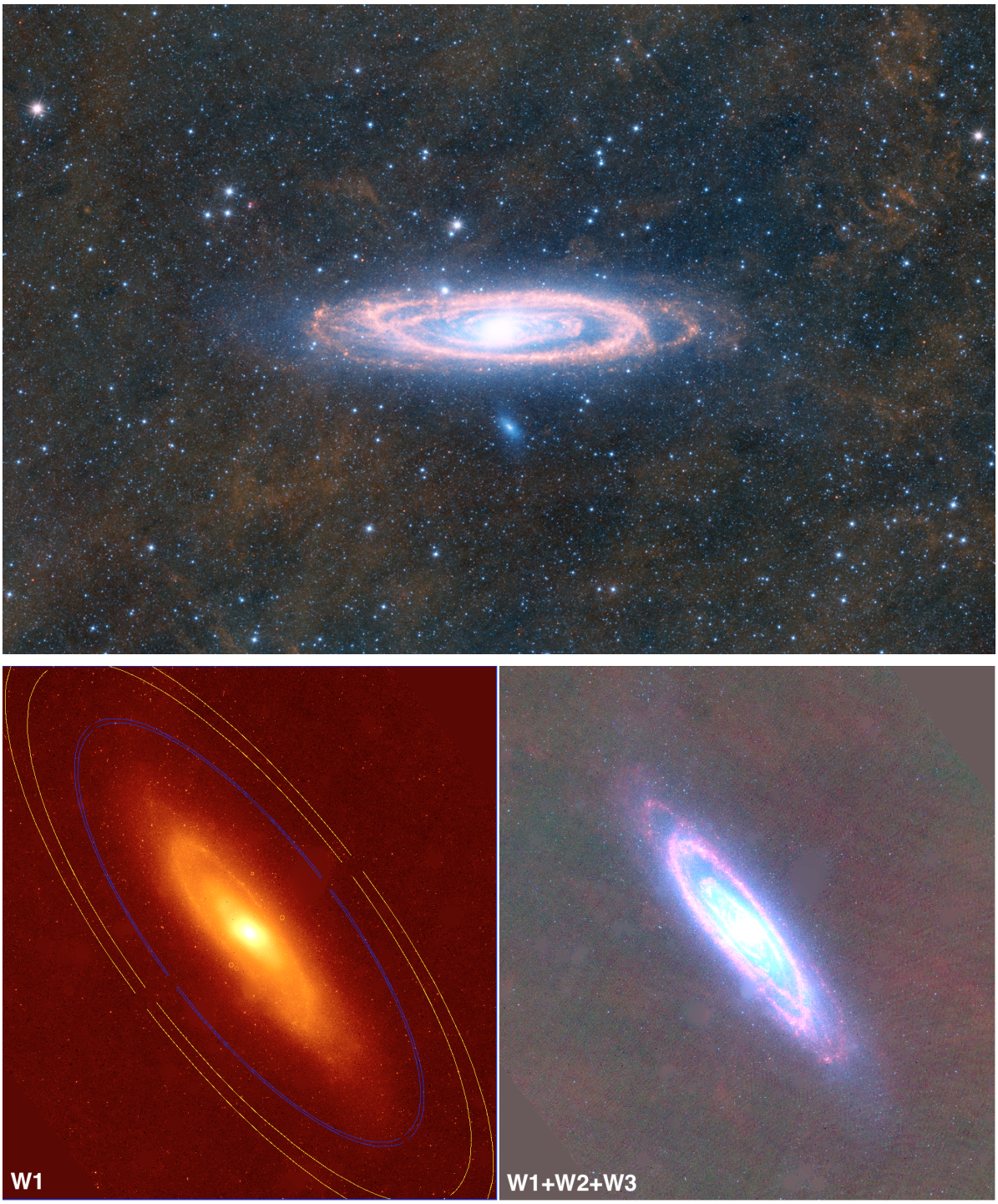

Figure 4.1: The top panel shows the 3-color image of the M 31 region rotated to fit the page. With standard E of N orientation, the bottom panel shows the Galactic source-cleaned W1 (left) and 3-color (right) images of M 31 using source classification methods discussed in Chapter 2. Satellite galaxies M 32 and M 110 were masked from the images to obtain a clean measurement of M 31.

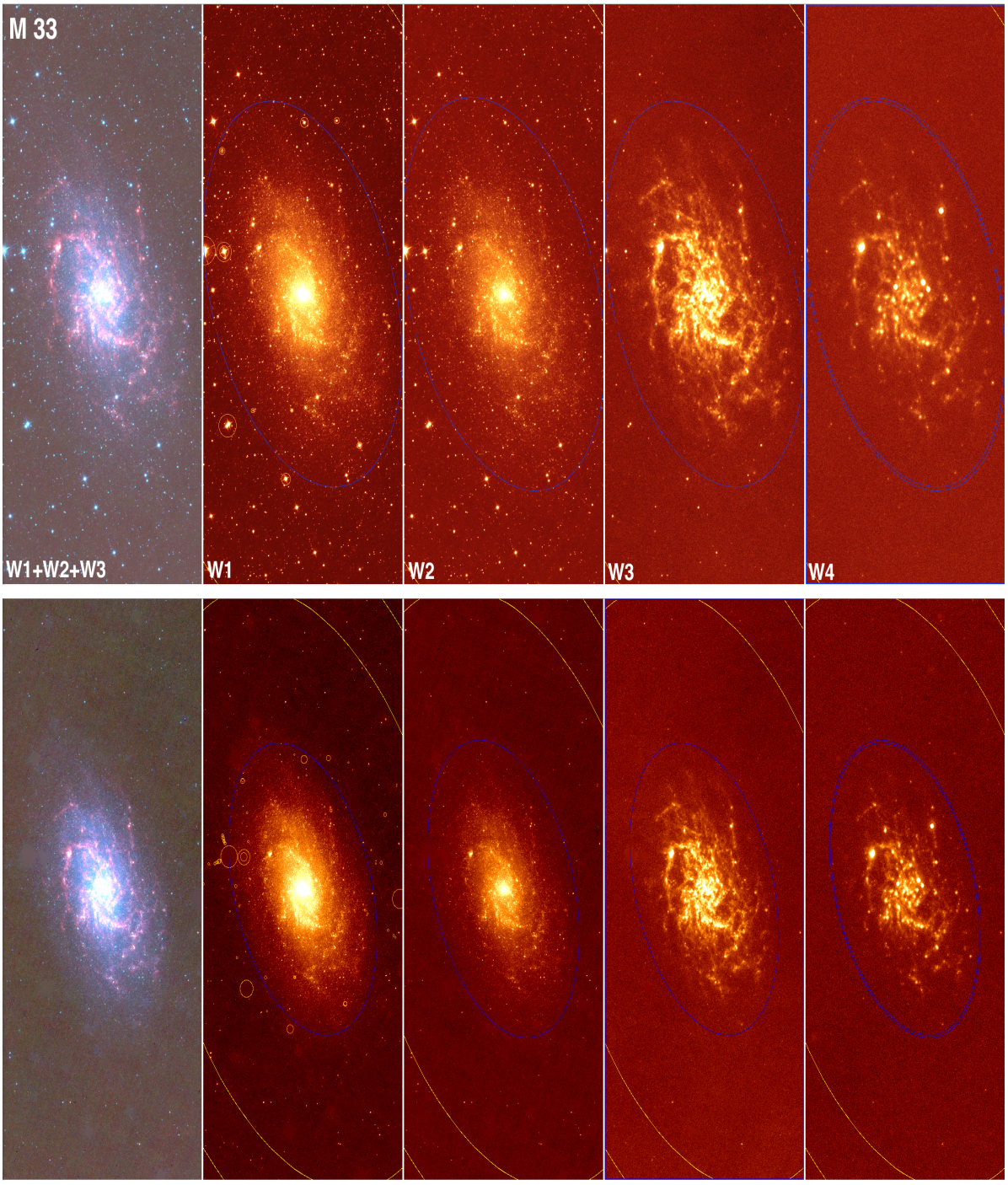

Figure 4.2: The top panel (left to right) shows the 3-color WISE image, and the W1, W2, W3 and W4 images of M 33. The bottom panel shows the images cleaned of Galactic sources. Images are 2° across the N-S (top-bottom) axis.

4.2 Basic Measurements

The WISE photometry and characterization measurements for M 31 (and M 33) extracted from the cleaned images are shown in Table 4.1 (fiducial isophotal photometry), Table 5.3 (extrapolated 'total' fluxes) and Table 5.4 (half-light and concentration indices). For cross-band colour comparisons, a fiducial aperture is adopted to report the integrated fluxes for each band. This is chosen as the W1 1σ isophotal radius because the W1 band is the most sensitive to faint lower surface brightness emission in the outer disks. The axis ratio and orientation, however, are based on the higher signal-to-noise ratio isophote at 3-σ in W1 (Jarrett et al., 2013). The flux measurements are not corrected for Galactic or internal extinction because for the WISE bands, these corrections are $< 1\%$. The flux uncertainties shown include contributions from both the Poisson errors and background estimation errors and accounting for correlated pixels and coverage depth differences (Jarrett et al., 2013). Fig. 5.8 shows colour-colour distribution of M 31 and M 33 overlaid on the WISE colour-colour plot (Wright et al., 2010). As expected, they lie in the "spiral" galaxy range of the plot.

Table 4.1: Mid-IR Isophotal Aperture Photometry.

Name	R.A. (°)	Decl. (°)	Axis Ratio	P.A. (°)	$R1_{iso}$ ($''$)	W1 (Jy)	W2 (Jy)	W3 (Jy)	W4 (Jy)
M 31	10.68479	41.26907	0.35	37.3	6686	285.3 ±3.0	151.8 ±1.6	175.5 ±1.8	142.7 ±1.5
M 33	23.46204	30.66022	0.59	18.9	1898	17.77 ±0.19	10.57 ±0.11	33.81 ±0.36	49.40 ±0.52

Notes. The fiducial aperture for all four bands is based on the W1 1σ isophotal radius for cross-band comparisons. Aperture and colour corrections have not been applied.

Table 4.2: Mid-IR Colour Photometry.

Name	W1-W2 [mag]	W2-W3 [mag]	W1-W3 [mag]	W3-W4 [mag]
M 31	0.033±0.016	2.081±0.016	2.048±0.016	1.150±0.016
M 33	0.073±0.016	3.185±0.016	3.258±0.016	1.774±0.016

Notes WISE colour measurements derived from matched aperture photometry.

Table 4.3: Mid-IR Extrapolated Photometry.

Name	$R1_{ext}$ ($''$)	$W1_{ext}$ (Jy)	$R2_{ext}$ ($''$)	$W2_{ext}$ (Jy)	$R3_{ext}$ ($''$)	$W3_{ext}$ (Jy)	$R4_{ext}$ ($''$)	$W4_{ext}$ (Jy)
M 31	10029	290.4±3.0	10029	152.5±2.0	10029	175.8±2.0	10029	143.5±2.0
M 33	2848	18.1±0.1	2848	10.8±0.2	3126	34.1±0.5	2848	50.4±0.6

Notes. The extrapolated 'total' photometry is the sum of the isophotal photometry in Table 4.1 and the integrated double-Sersic fit to the elliptical-radial surface brightness carried out from R_{iso} to R_{ext}.

Table 4.4: WISE Half-light Surface Brightness and Concentration.

Name	$R1_e$ ($''$)	$W1_e$ (mag/sq)	C1	$R2_e$ ($''$)	$W2_e$ (mag/sq)	C2	$R3_e$ ($''$)	$W3_e$ (mag/sq)	C3	$R4_e$ ($''$)	$W4_e$ (mag/sq)	C4
M 31	1393	16.64	4.80	1351	16.63	4.68	2176	15.59	2.03	2171	14.44	1.86
M 33	650.6	18.56	2.79	639.9	18.46	2.78	608.6	15.18	2.59	649.0	13.53	2.46

Notes. The half light is relative to the extrapolated integrated flux shown in Table 5.3, and the concentration index is the ratio of the 3/4 light-radius to the 1/4 light-radius.

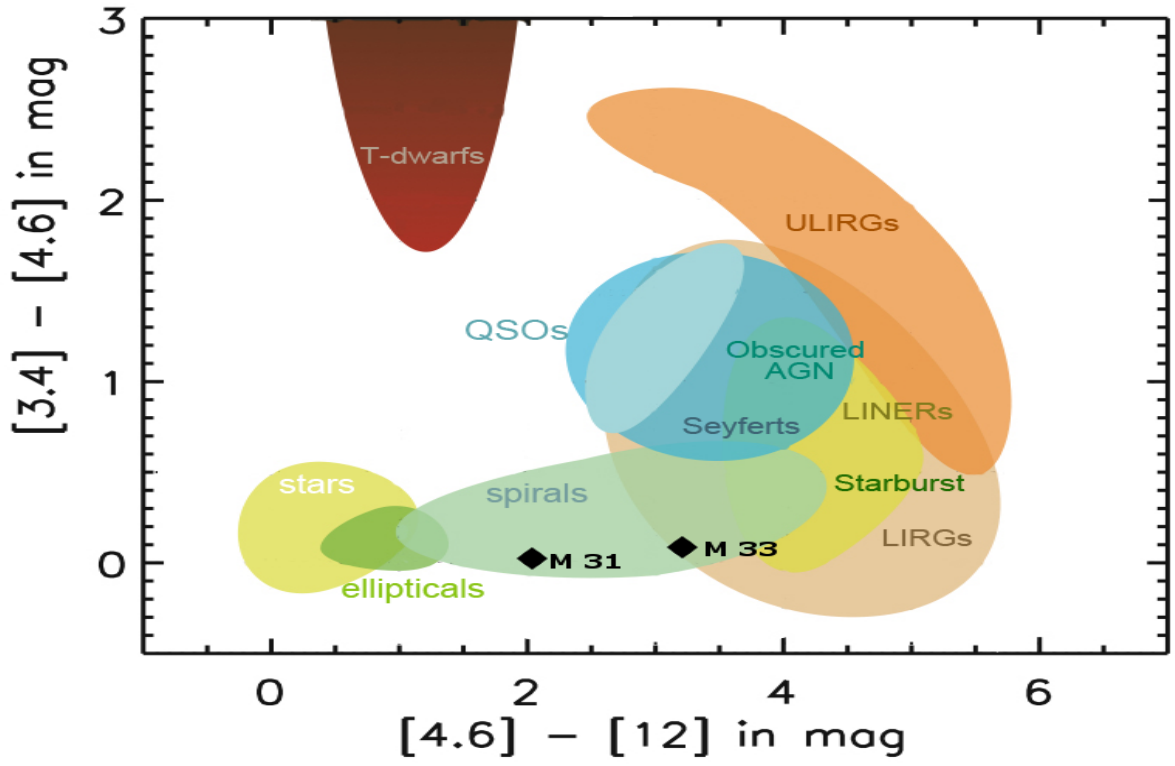

Figure 4.3: The colour-colour distribution of M 31 and M 33 overlaid on the WISE colour-colour plot (Wright et al., 2010), where they both lie in the 'spiral' galaxy range.

4.2.1 Surface Brightness Profiles

In Fig. 4.4 and 4.5, the azimuthal radial surface brightness profiles for the WISE W1, W2, W3 and W4 bands where the magnitudes are in Vega units for M 31 and M 33, respectively, are presented. The double-Sersic fits (Sérsic, 1963) to the radial profiles are also shown in the figures: the 'bulge' component in cyan, the 'disk' component in orange, and the composite fit in blue (method as described in Jarrett et al., 2013). The red dashed vertical lines represent the 1-σ isophotal radii and the green dashed lines, the effective (half-light) radii. M 31's bright spiral arms are seen as a bump in the W3 and W4 profiles between radii 1300″ (5 kpc) and 3200″ (12 kpc); the double-Sersic composite fits deviate from the profiles in this region, as expected. The double-Sersic profile fit parameters are shown in Table 4.5 below.

Table 4.5: Double Sérsic Profile Parameters.

Band	M 31				M 33			
	Bulge		Disk		Bulge		Disk	
	α [kpc]	β	α [kpc]	β	α [kpc]	β	α [kpc]	β
W1	0.154	1.60	3.185	1.15	0.187	1.50	2.866	0.70
W2	0.150	1.53	3.392	1.03	0.178	1.55	2.805	0.70
W3	0.142	1.55	6.127	0.80	0.291	1.20	2.613	0.70
W4	0.165	1.45	6.037	0.71	0.266	1.25	2.558	0.70

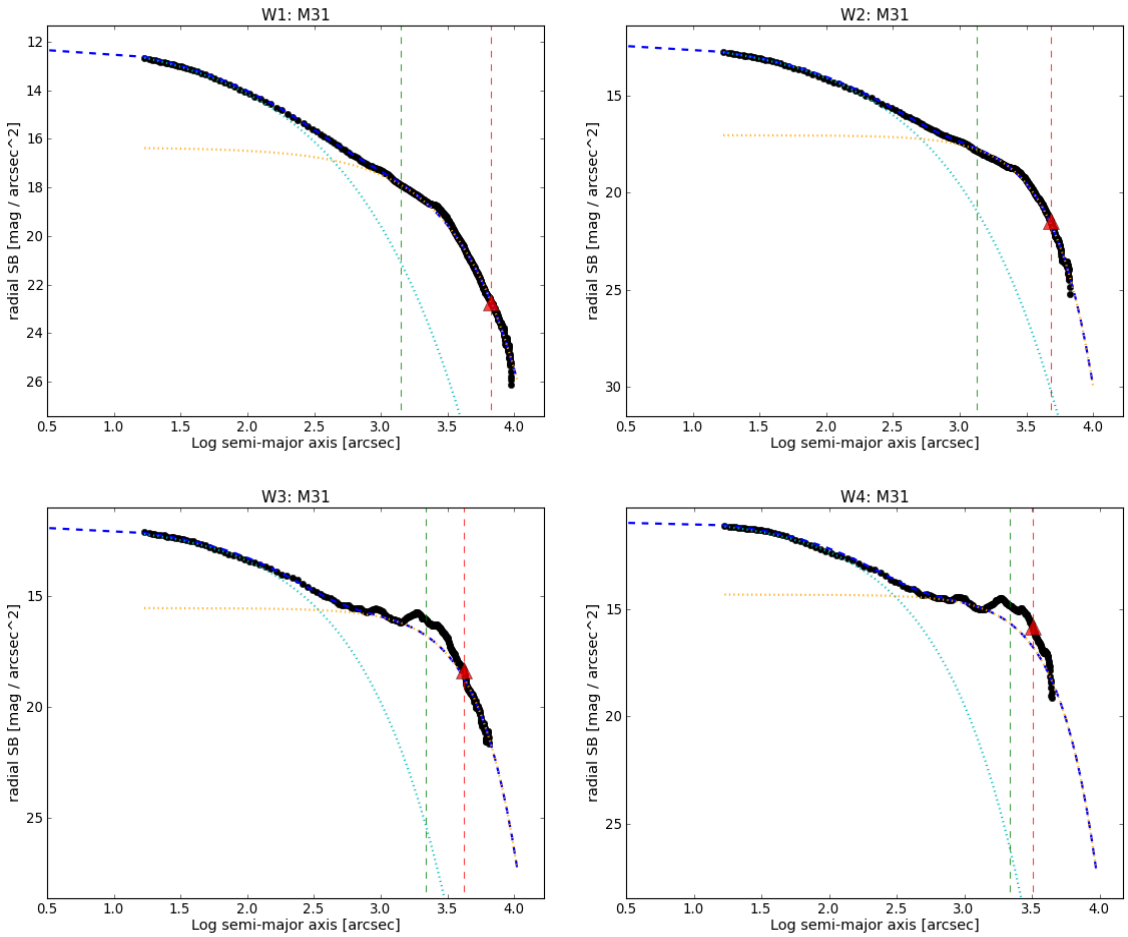

Figure 4.4: The W1 (top-left panel), W2 (top-right panel), W3 (bottom-left panel) and W4 (bottom-right panel) azimuthal radial surface brightness profiles of M 31 (black points). The Sérsic function fit to the profiles is represented by the blue dashed line; the cyan dotted line represents the 'bulge' component of the fit, and the orange dotted line represents the 'disk' component of the fit. The red dashed vertical line and the green dashed line represent the 1-σ isophotal radius and the effective (half-light) radius respectively. The red triangles demark the 1-sigma isophotal radius.

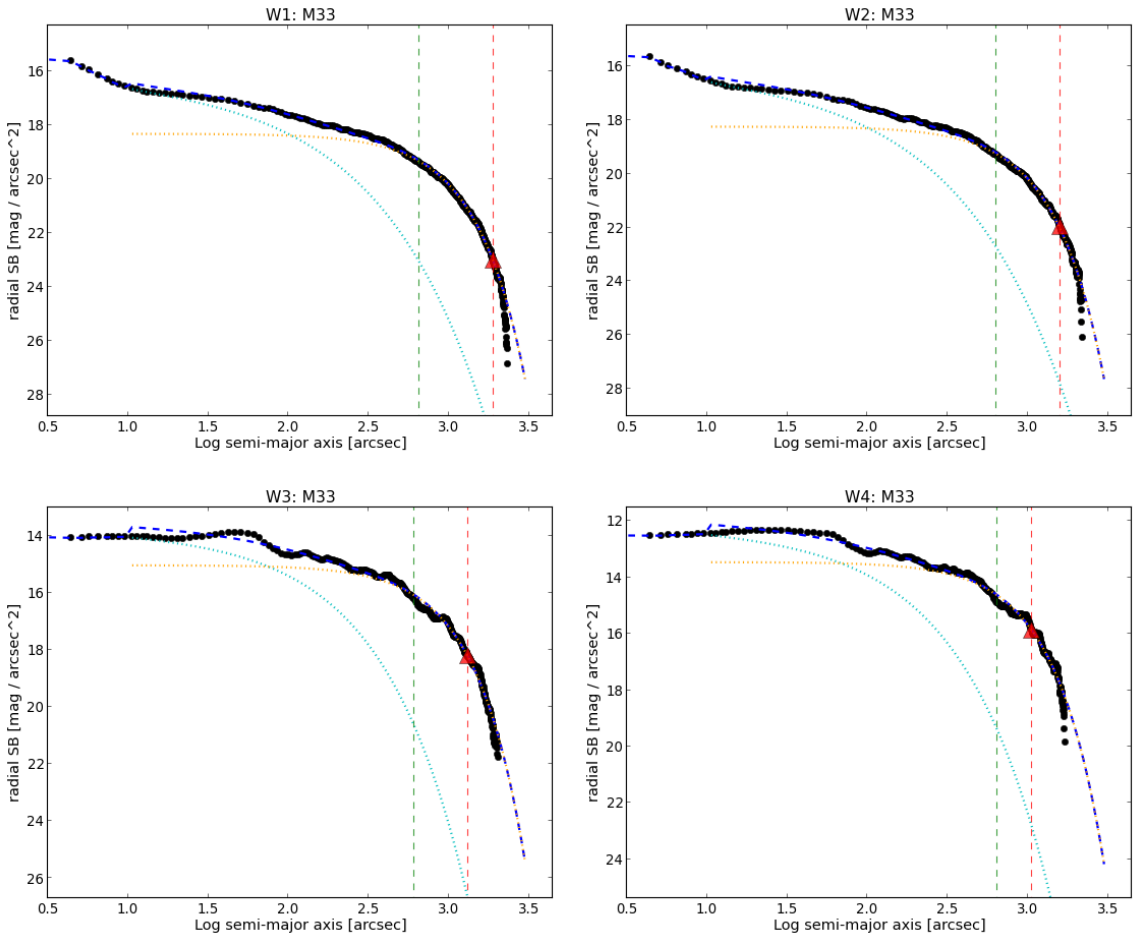

Figure 4.5: The W1 (top-left panel), W2 (top-right panel), W3 (bottom-left panel) and W4 (bottom-right panel) azimuthal radial surface brightness profiles of M 31 (black points). The Sérsic function fit to the profiles is represented by the blue dashed line; the cyan dotted line represents the 'bulge' component of the fit, and the orange dotted line represents the 'disk' component of the fit. The red dashed vertical line and the green dashed line represent the 1-σ isophotal radius and the effective (half-light) radius respectively. The red triangles demark the 1-sigma isophotal radius.

4.2.2 Comparison with Ancillary Data

Table 5.1 shows a summary of photometric results for M 31 from ancillary data and this work, and Fig. 4.6 shows the spectral energy distribution. For comparison, the SED was plotted with the template for an Sb galaxy from GRASIL models (Silva et al., 2011), represented by the yellow line, and the SEDs for SA(s)a type galaxy, NGC 4594, and SA(rs)ab type galaxy, NGC 4826, from Brown et al. (2013), represented by the light-grey and dark-grey lines, respectively. It should be noted that the 2MASS J, H and K integrated fluxes are too low due to the difficulty with background subtraction. Although, the M 31 flux densities mostly agree within error with results from Rice et al. (1988), Barmby et al. (2006) and Montalto et al. (2009), they are on average higher than their *Spitzer* counterparts. This is expected as WISE observes the entire region of M 31 and, therefore, has sufficient area to account for the local background. However, the difference between W2 and IRAC 4.5 μm is not significant. This may be because W2 is not as deep as W1, so the result is less affected by the size of the maps. This would allow the *Spitzer* measurement, even with smaller maps, to be comparable to the W2 measurement. The WISE photometry here has been aperture corrected (0.034, 0.041, -0.030 and 0.029 mag for W1, W2, W3 and W4, respectively) and W4 colour corrected (8% correction), as prescribed by Jarrett et al. (2013).

For M 33, previous multi-wavelength data were obtained from NED in order to construct the SED of the galaxy. The SED is plotted in Fig. 4.7, along with the template for an Sb galaxy (black line) and the template for an Sc galaxy (grey line), obtained from GRASIL models (Silva et al., 2011), for comparison. The aperture and W4 color corrected mid-IR integrated flux densities of the galaxy show good agreement with previous results, verifying the validity of the characterization method.

Table 4.6: M 31 Photometric Properties.

	Instrument	Band [μm]	Semi-major Radius [arcsec]	Integrated Flux [Jy]
X-ray 20-100 keV	BAT [a]	3.1×10^{-5}	1200	$(9.1 \pm 1.2) \times 10^{-7}$
2-20 keV	PCA [a]	1.4×10^{-4}	1200	$(4.2 \pm 0.4) \times 10^{-6}$
UV AB	GALEX [b]	0.15	1462	1.67±0.01
	GALEX [b]	0.23	1430	3.82±0.02
Optical B	SDSS [c]	0.48	4599	278 ± 11
Infrared	2MASS [d]	1.3	3100	230 ± 3
	2MASS [d]	1.7	3100	314 ± 5
	2MASS [d]	2.2	3100	269 ± 4
	WISE [j]	**3.4**	**6686**	$\mathbf{276 \pm 3}$
	IRAC [e]	3.6	5040	239 ± 29
	IRAC [f]	3.6	6480	259 ± 32
	IRAC [f]	4.5	6480	144 ± 20
	WISE [j]	**4.6**	**6686**	$\mathbf{146 \pm 2}$
	IRAC [e]	8.0	5040	149 ± 27
	IRAC [f]	8.0	6480	151 ± 21
	IRAS [g]	12	5334	163 ± 24
	WISE [j]	**12**	**6686**	$\mathbf{180 \pm 2}$
	WISE [j]	**22**	**6686**	$\mathbf{128 \pm 2}$
	MIPS [e]	24	5040	118 ± 17
	IRAS [g]	25	5334	108 ± 16
	IRAS [g]	60	5334	536 ± 80
	MIPS [e]	70	5040	1086 ± 256
	IRAS [g]	100	5334	2928 ± 439
	PACS [h]	100	11140	3055±31
	MIPS [e]	160	5040	7315 ± 1632
	PACS [h]	160	11140	7348±73
	SPIRE [h]	250	11140	5791±405
	SPIRE [h]	350	11140	3047±213
	SPIRE [h]	500	11140	1313±92
Radio	DRAO [i]	21×10^4	10000	9.79×10^{-2}

Notes. [a] Revnivtsev et al. (2014), [b] Gil de Paz et al. (2007), [c] Tempel et al. (2010), [d] Jarrett et al. (2003), [e] Montalto et al. (2009), [f] Barmby et al. (2006), [g] Rice et al. (1988), [h] Fritz et al. (2012), [i] Chemin et al. (2009), [j] Isophotal photometry from this work, where aperture (0.034, 0.041, -0.030 and 0.029 mag for W1, W2, W3 and W4, respectively) and W4 8% colour corrections, have been applied (Jarrett et al., 2013).

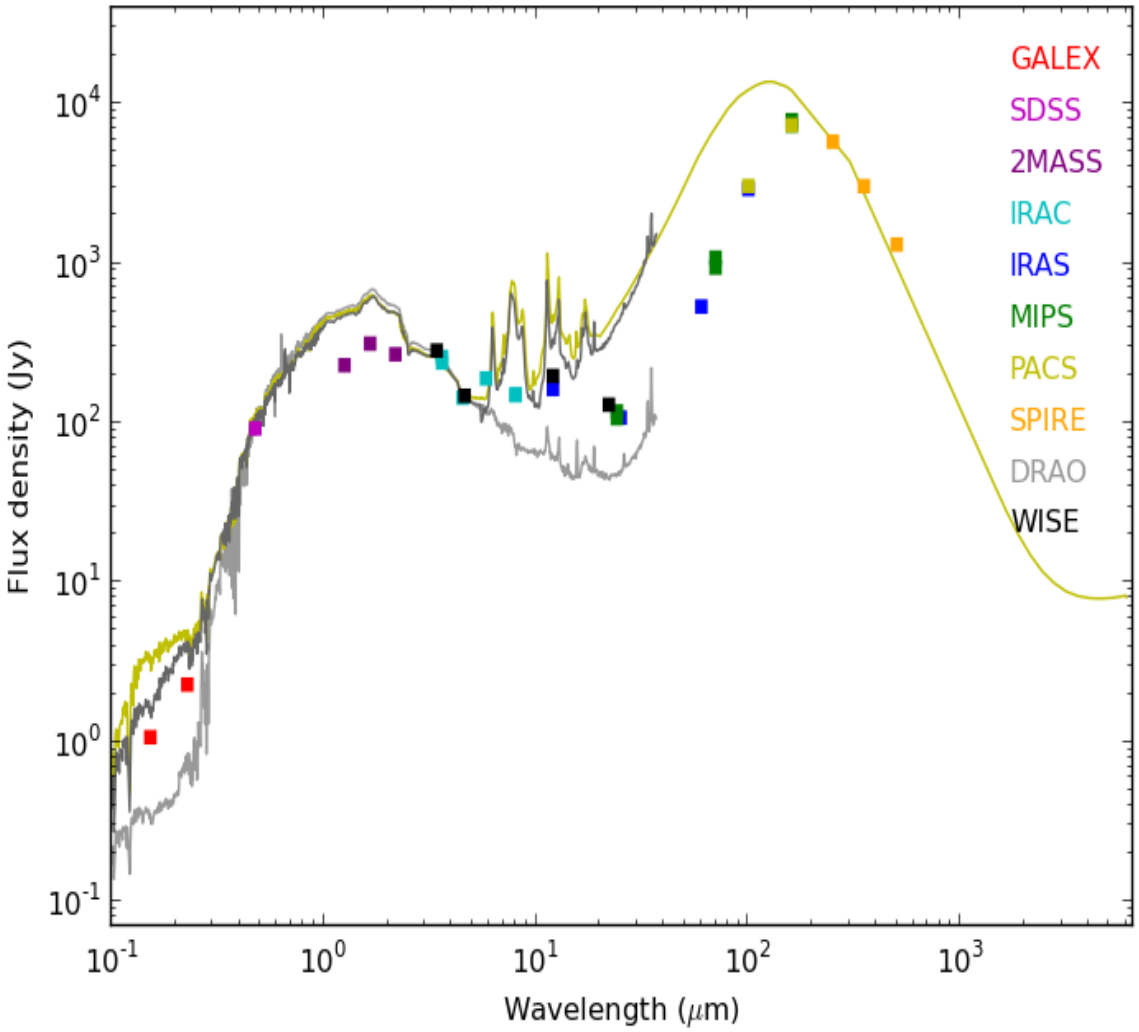

Figure 4.6: Spectral Energy distribution of M 31 using this work and work from the literature. Note that the apertures have not been matched (see Table 5.1), hence, scatter is expected from this. The yellow continuous line represents the template for an Sb galaxy from GRASIL models (Silva et al., 2011), the grey line represents the SED for SA(s)a type galaxy NGC 4594 and the dark-grey line represents the SED for SA(rs)ab type galaxy NGC 4826 (Brown et al., 2013).

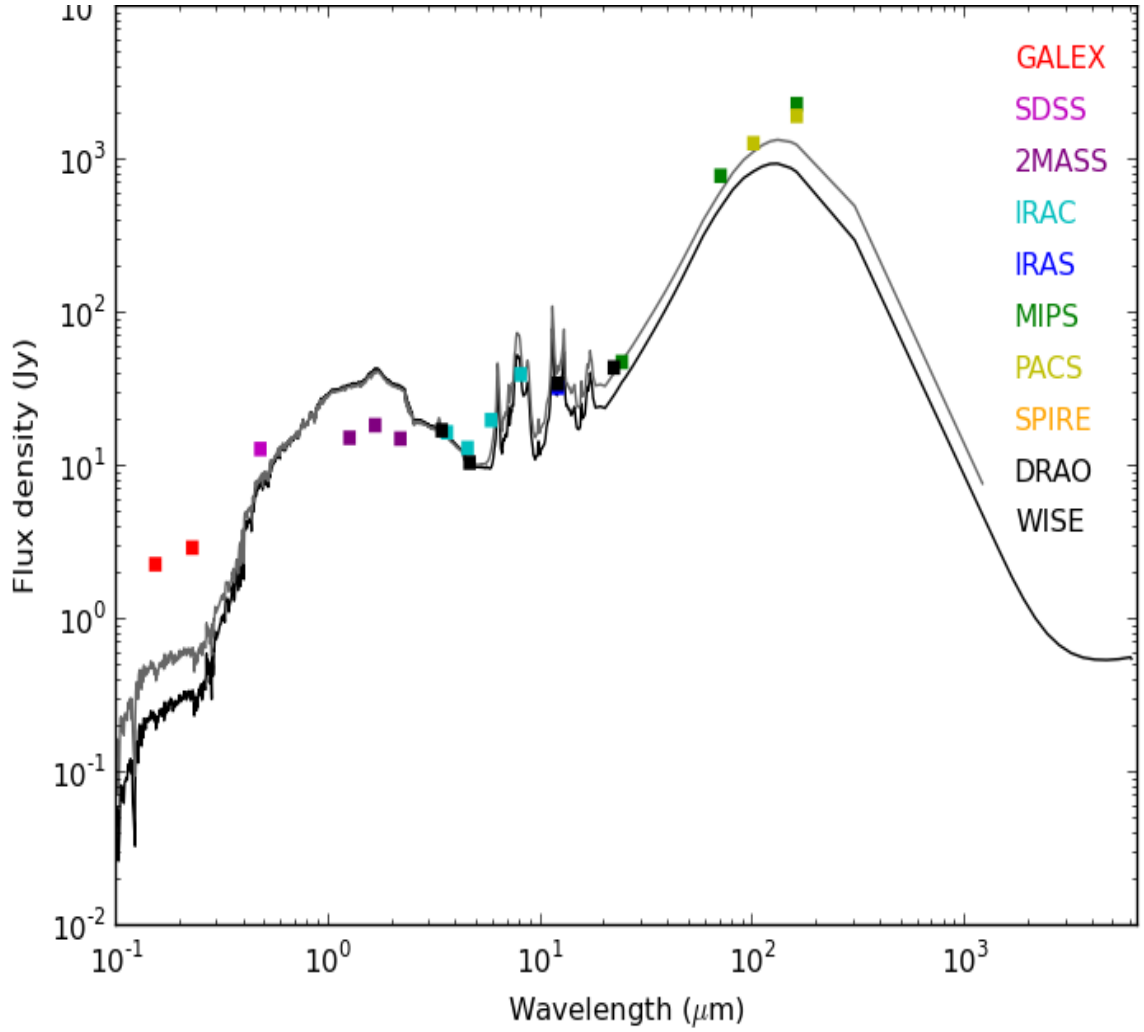

Figure 4.7: Spectral Energy distribution of M 33 using this work and previous measurements (obtained from NED). Note that the apertures have not been matched, hence, scatter is expected from this. The black continuous line represents the template for an Sb galaxy and the grey line represents the template for an Sc galaxy from GRASIL models (Silva et al., 2011)

4.2.3 Stellar Mass

3.4 and 4.6 μm bands of WISE are effective measures of the stellar mass as they are sensitive to light from evolved stars which make up most of the stellar content in galaxies. A combination of the two bands gives a good estimation of the stellar mass because, in addition to being relatively extinction free, they have a constant W1-W2 colour for local galaxies that is independent of the age of the stellar population and its mass function (Jarrett et al., 2011). The stellar mass is estimated using the WISE mass-to-light ratio developed by Jarrett et al. (2013) and Cluver et al. (2014; Eq. 1.1 in Sect. 1.1). This was done using corrected W1 absolute magnitudes of -24.4 and -21.6 mag for M 31 and M 33, respectively.

The M 31 stellar mass estimation of $8.7 \times 10^{10} M_{\odot}$ is about 40% more massive than $(5.5 \pm 0.01) \times 10^{10} M_{\odot}$, an estimation recently obtained from the HELGA survey using *Herschel* data together with previous data from UV to sub-millimeter wavelengths and modeling panchromatic SEDs (Viaene et al., 2014). If the stellar mass is estimated using the relation derived by Jarrett et al. (2013), the result is $5.3 \times 10^{10} M_{\odot}$, which is comparable to the HELGA result. The difference between this result and the Cluver et al. (2014) result demonstrates the high uncertainties that are involved in the stellar mass estimate. The MW is estimated to have a total stellar mass of $4.6^{+2.0}_{-1.3} \times 10^{10} M_{\odot}$ using model fits to SDSS photometry (Licquia & Newman, 2013). Therefore, according to the results in this work, M 31 is more massive than the MW, although uncertainties in stellar mass estimations are comparable to the differences in the masses (Jarrett et al., 2013). Previous estimates for M 33's stellar mass include an estimate of $3 - 6 \times 10^{9} M_{\odot}$, made by Corbelli (2003) using rotational curves from the CO J= 1 - 0 line, which were complemented with previous 21 cm data. This estimate is comparable to the measurement obtained in this study.

Table 4.7: Stellar Mass

Name	$\log_{10} M_{stellar}/L_{W1}$	L_{W1} [a] $[L_{\odot}]$	$M_{stellar}$ $[M_{\odot}]$
M 31	-0.095	1.1×10^{11}	8.7×10^{10}
M 33	-0.173	9.0×10^{9}	6.1×10^{9}

Notes. [a] The distances used to obtain the luminosities were 785 kpc (McConnachie et al., 2005) and 880 kpc (Tully et al., 2009) for M 31 and M 33, respectively.

4.2.4 Star-formation Rates

Young (10-15 Myr) massive stars emit UV photons which are primarily absorbed by surrounding gas and dust, and re-emitted at longer (mid-IR to far-IR) wavelengths. Star formation is traced by PAH emission arising from the PDRs located at the boundaries

of HII regions and molecular clouds, as well as emission from warm dust arising in the vicinity of hot HII regions. Therefore, the W3 and W4 bands (12 μm and 22 μm) can be used to measure the global star formation rates (SFRs), however, they are only sensitive to the star formation obscured by dust, and thus only represent a lower limit to the total SFR which would include far-infrared and UV emission. The UV radiation from hot young stars that escapes absorption from dust allows the FUV and NUV bands to be quantifiers of unobscured star formation in galaxies. Therefore, to effectively trace star formation and provide a more complete estimation of the SFR, results from IR and UV (obscured and unobscured SFR) observations should be combined.

The WISE star formation rates for M 31 and M 33 are estimated by the 12 μm and 22 μm fluxes using both the relations derived by Jarrett et al. (2013, Eq. 1.2 and 1.3) and Cluver et al. (2014, Eq. 1.4 and 1.5). These WISE results are shown in Table 4.8. For comparison, the estimations from the 24 μm (MIPS), and the 1516 Å and 2267 Å (GALEX) fluxes, are included. The 24 μm, 1516 Å and 2267 Å SFRs, based on their respective luminosities (see Table 5.1 for M 31 measurements; the M 33 24 μm, 1516 Å and 2267 Å measurements were obtained from NED), are derived here using relations from Rieke et al. (2009, Eq. 1.6), Buat et al. (2008, Eq. 1.7), and Schiminovich et al. (2007, Eq. 1.8), respectively.

Table 4.8: IR and UV Global Star Formation Rates using Different Prescriptions.

Name		IR (12 μm)		IR (22 μm)		IR (24 μm)	FUV (0.15 μm)	NUV (0.23 μm)
		a	*b*	*a*	*b*	*c*	*d*	*e*
M 31	$\log(\nu L_\nu/L_\odot)$	8.937	8.937	8.525	8.525	8.459	8.802	8.986
	SFR $[M_\odot \mathrm{yr}^{-1}]$	0.4	0.7	0.3	0.5	0.2	0.1	0.2
M 33	$\log(\nu L_\nu/L_\odot)$	8.214	8.214	8.120	8.120	8.069	8.942	8.874
	SFR $[M_\odot \mathrm{yr}^{-1}]$	0.1	0.1	0.1	0.2	0.1	0.2	0.1

Notes. The νL_ν luminosity (normalized by the total solar luminosity) is derived from the integrated flux density (Table 5.1 for M 31 measurements; the M 33 24 μm, 1516 Å and 2267 Å measurements were obtained from NED) and the distance 785 kpc (McConnachie et al., 2005) and 880 kpc (Tully et al., 2009) for M 31 and M 33, respectively. The 12 and 22 μm SFRs are derived using relations from both Jarrett et al. (2013, a) and Cluver et al. (2014, b). The 24 μm, 1516 Å and 2267 Å SFRs are derived using relations from Rieke et al. (2009, c), Buat et al. (2011, d) and Schiminovich et al. (2007, e), respectively.

The differences between the IR and the UV SFR estimates for M 31 verifies the need to account for unobscured star formation. For M 33, the IR and UV estimates are comparable suggesting that obscuration isn't as large for M33 as it is for M31. The relatively low SFR estimations for M 31, compared to its size, suggest passive evolution. M 33 estimates are 1-7 times lower than M 31 estimates, although M 33 is much smaller than M 31. Previous estimates for M 33 agree with those measured in this work. This includes the measurement from Massey et al. (2007) of 0.1 $M_\odot \mathrm{yr}^{-1}$, using the H_α emission line.

Compared to the SFR estimation of $0.25^{+0.06}_{-0.04}$ $M_{\odot}\mathrm{yr}^{-1}$ made by Ford et al. (2013) using *Herschel* data and 24 μm emission for calibration, and that of $\sim$ 0.3 $M_{\odot}\mathrm{yr}^{-1}$, in the area 6 kpc $< R <$ 17 kpc, by Tabatabaei & Berkhuijsen (2010) using *Spitzer* data and de-reddened H_{α} emission, the 12 μm and 22 μm estimates are higher and the 24 μm, 1516 Å and 2267 Å estimates are comparable. SFRs of 0.75 $M_{\odot}\mathrm{yr}^{-1}$, estimated by fitting a simple stellar population-plus-dust grain model to MIPS data (Gordon et al., 2006), and 0.4 $M_{\odot}\mathrm{yr}^{-1}$, using the 8 μm non-stellar luminosity (Barmby et al., 2006), compare well with the 12 μm value from the Cluver et al. (2014) and Jarrett et al. (2013) relation, respectively.

Previous SFR estimates for the MW include 1.9 ± 0.4 $M_{\odot}\mathrm{yr}^{-1}$ by Chomiuk & Povich (2011), using a common IMF from available estimates and stellar models applied to measured free-free emission rates, and 0.9-2.2 $M_{\odot}\mathrm{yr}^{-1}$ by Murray & Rahman (2010), using the Lyman continuum luminosity from HII regions free-free radio continuum and a range of IMF slopes. These measurements are $\sim$1-11 times larger than M 31 estimates and $\sim$9-22 times larger than M 33 estimates made here, indicating that the MW is actively forming stars faster than M 31 and M 33, which are seemingly experiencing more passive star formation.

4.2.5 Specific Star-formation Rates

The global SFR and stellar mass, parameters important for galaxy evolution studies, are combined to investigate the specific star formation rate (sSFR) in order to gauge the present-to-past star formation history of M 31 and M 33. The sSFR for M 31 and M 33 are over plotted on the GAMA data from Cluver et al. (2014) showing the specific star formation derived from the $L_{12_{\mu m}}$ as a function of stellar mass, colour-coded by redshift (Fig. 4.8). The sample reveals trends of lower mass galaxies actively building disks and higher mass galaxies exhibiting passive evolution. The over plotted positions of M 31 and M 33 on the sSFR show that they both behave according to these trends. M 33 has a lower mass and is thus still actively building its disk, while M 31, with a significantly higher mass, shows relatively quiescent evolution. The magnitude-limited, optically-selected GAMA sample is sensitive to lower mass systems only at low redshifts, and more active and massive galaxies at higher redshift. The over plotted positions of M31 and M33 show them to appear typical within the local population i.e. their SFR in relation to their stellar mass is not unusual, albeit at the low (relatively quiescent) end. In general, M31 and M33 have somewhat lower activity compared to other galaxies with similar stellar mass at low-redshift. GAMA has a larger sample volume at higher redshift and is therefore sensitive to more active (luminous) galaxies typical at higher redshift.

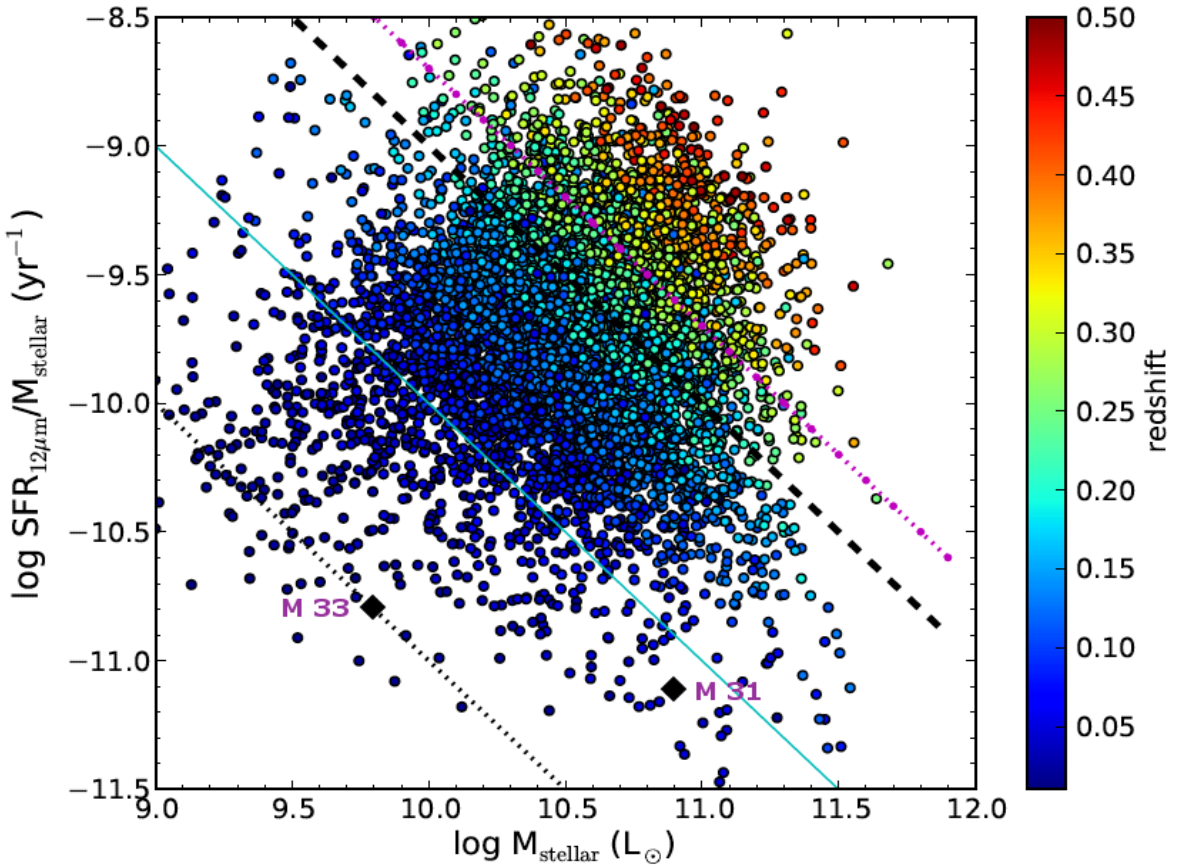

Figure 4.8: Specific star formation colour-coded with redshift derived by Cluver et al. (2014). The positions for M 31 and M 33 are over plotted in black for comparison. Lines of constant SFR (0.1, 1, 10 and 20 $M_\odot yr^{-1}$) are shown as dotted, solid, dashed and dash-dot lines, respectively.

Chapter 5

M 31 Local environment

In this chapter, the local environment is investigated. In particular, the distribution of globular clusters across the region is studied in Sect. 5.1, and that of the satellite galaxies in Sect. 5.2.

5.1 Globular Clusters

The Revised Bologna Catalogue (RBC, V.5, August 2012) has a comprehensive dataset of confirmed and candidate M 31 globular clusters obtained from near-IR photometry, with an average astrometric accuracy within $1''$. This catalogue is used to search for WISE counterparts of these confirmed and candidate clusters, using the AllWISE Source Catalog from IRSA[1], in order to study their photometric properties. Using a search radius of $4''$, 217 out of 377 RBC confirmed globular clusters and 252 out of 331 RBC candidate clusters were detected by WISE. The RBC confirmed GC's are studied here in order to inspect whether they are observed by WISE, and to investigate the mid-IR properties of these GC's. For RBC candidate clusters, their distribution is investigated, including the colour-colour distribution, in order to determine whether their properties align with those of RBC confirmed GC's as observed by WISE. Non-detections were not used in these analyses, therefore, biases could exist when interpreting the global photometric measurements. Images of some of the RBC confirmed and candidate clusters are shown in Fig. 5.1 and Fig. 5.2, respectively. At the resolution of WISE, the clusters are observed as single unresolved sources ($\sim 2''$).

[1] http://irsa.ipac.caltech.edu/applications/Gator/

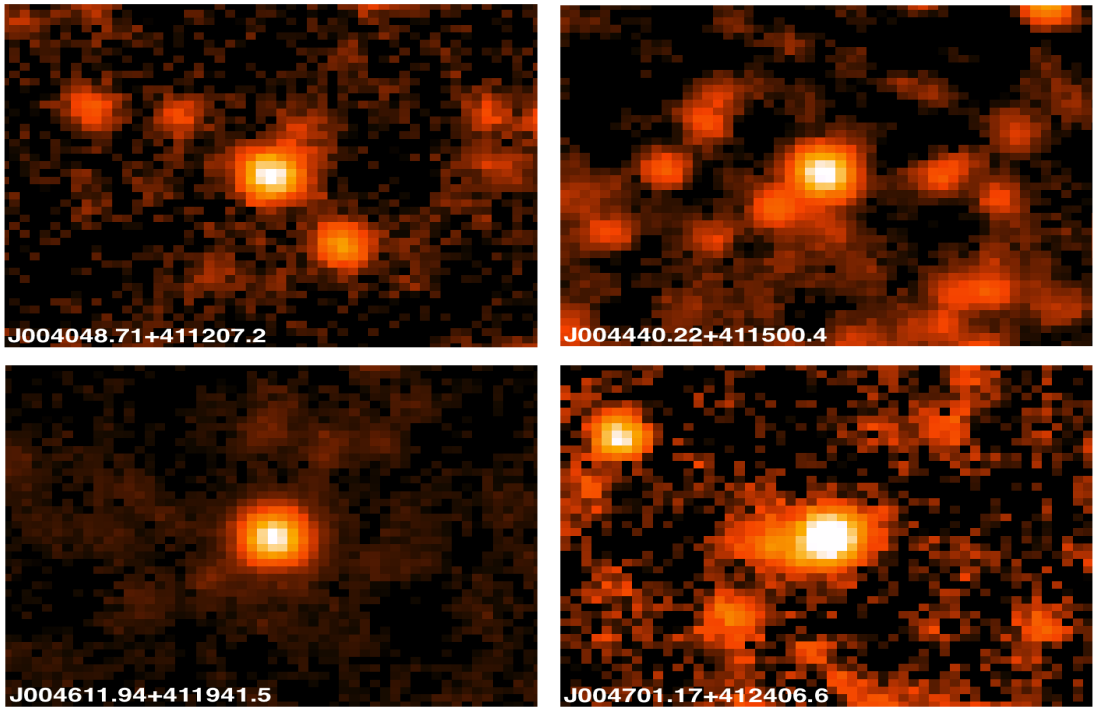

Figure 5.1: Examples of RBC confirmed GC's observed by WISE in the M 31 region. The images are 70″ across.

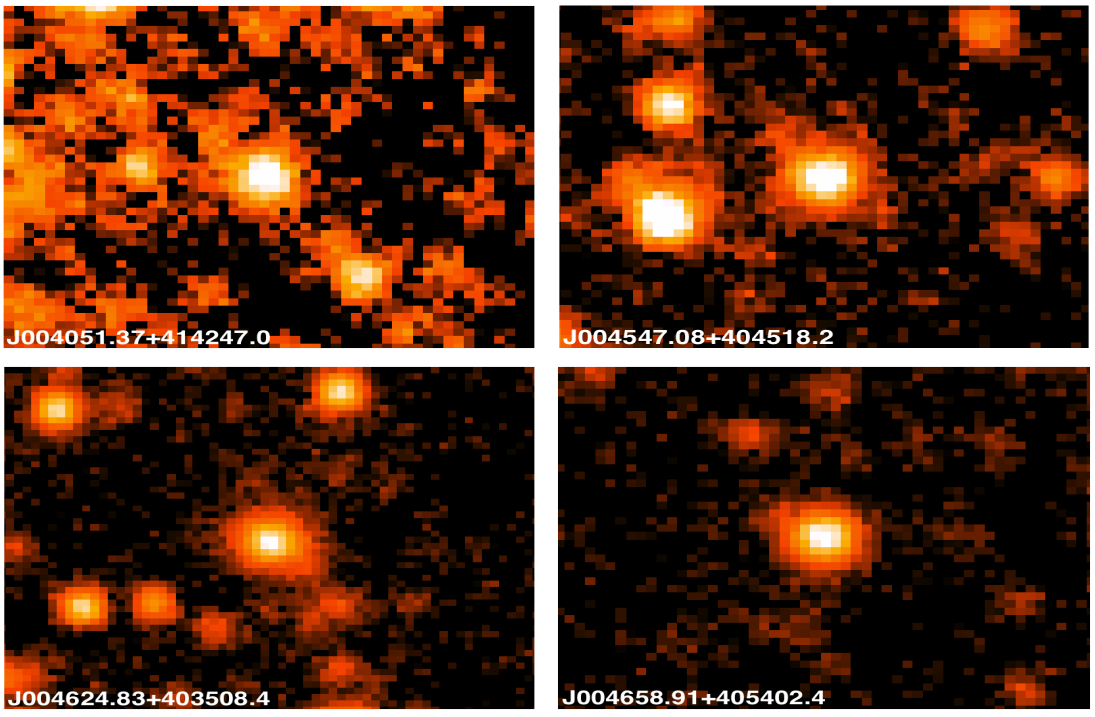

Figure 5.2: Examples of RBC candidate GC's observed by WISE in the M 31 region. The images are 70″ across.

Table 5.1: Globular Cluster Data

	RBC	WISE
Confirmed GC's	377	217
Candidate GC's	331	252

5.1.1 RBC Confirmed Clusters

Fig. 5.3 shows the spatial distribution of RBC confirmed GC's observed by WISE across the M 31 region. They are concentrated towards the center of the region (core and disk). The peak W1 magnitude value of these GC's is 14.7 mag (Fig. 5.4). The corresponding absolute magnitude, using a distance of 785 kpc (McConnachie et al., 2005), is -9.8 mag (Fig. 5.5). The absolute 2MASS distributions are shown in Fig. 5.6 for comparison. Using the full RBC catalogue of confirmed clusters (377 GC's) , the B, NUV and FUV peak absolute magnitudes are -6.4, -3.1 and -2.9 mag, respectively. The metallicity, has a mean value of -0.89 ± 0.61 (metal-poor), indicating that on average, the M 31 GC's contain old stars (Population II).

The W1-W2 colour distribution (with errors $< 15\%$) and W1 luminosity distribution (νL_ν for W1) of the clusters were also plotted (Fig. 5.7). The distributions have mean values of -0.06 ± 0.13 mag and $(4.5 \pm 10) \times 10^4 L_\odot$ for the W1-W2 colour and W1 luminosity respectively. However, the luminosity distribution has an outlier with $\nu L_\nu > 8 \times 10^5 L_\odot$, considerably higher than the other GC's. This source could be a background galaxy and is discussed in the following paragraph. When this source is removed from the analysis, the mean value is $(1.5 \pm 5.1) \times 10^4 L_\odot$. This is almost 10 times larger than the B luminosity of about $2 \times 10^3 L_\odot$. The W1-W2 colour compares well with IRAC colour [3.6]-[4.5]= -0.04 mag, measured by Barmby & Jalilian (2012). The stellar mass of the clusters was calculated using relations developed by Jarrett et al. (2013) and Cluver et al. (2014; Eq. 1.1, Sect. 1.1). The mean value was found to be $5.0 \times 10^5 M_\odot$. This is about twice the average mass of $1.9 \times 10^5 M_\odot$ for Galactic GCs which was measured by Mandushev et al. (1991). However, this may be a consequence of the WISE stellar mass calibration developed for galaxies, not GCs.

To investigate the colour distribution of the RBC confirmed M 31 GC's, a colour-colour diagram of the GC's, with errors $\leq 15\%$, was plotted and also overlaid on the WISE colour-colour plot (Fig. 5.8; Wright et al., 2010). The distribution shows that the GC's have W2-W3 colours < 1.5 mag; with the exception of one with a W2-W3 colour of 2.776 ± 0.094 mag (W1-W2= -0.004 ± 0.098 mag). This may, in fact, be a background galaxy as it lies in the spiral galaxy range of the WISE colour-colour plot. The source has a WISE identification of J004118.72+405715.5 (Fig. 5.9), with RA = 10.3280075°, Dec = 40.9543207°, and a W1 magnitude of 13.269 ± 0.038. The distance between the input GC (RBC) and the potential WISE counterpart is $0.09''$; considering WISE's

resolution, the two are, therefore, a good position match. A further check is to examine whether the source may be contaminated by a background object, i.e. the W1 profile-fit photometry reduced chi^2 value for the source. The reduced chi^2 for this source is 1.6, indicating that the source is point-like (< 2), and hence, not contaminated by a background object. Therefore, this source could be a background galaxy that has been mis-identified as a GC by the RBC. Otherwise, the GC colours plotted lie within the stars (and ellipticals) range of the colour-colour plot as expected ($-0.1 \leq$ W1-W2 ≤ 0.2, $-0.5 \leq$ W2-W3 ≤ 1.5).

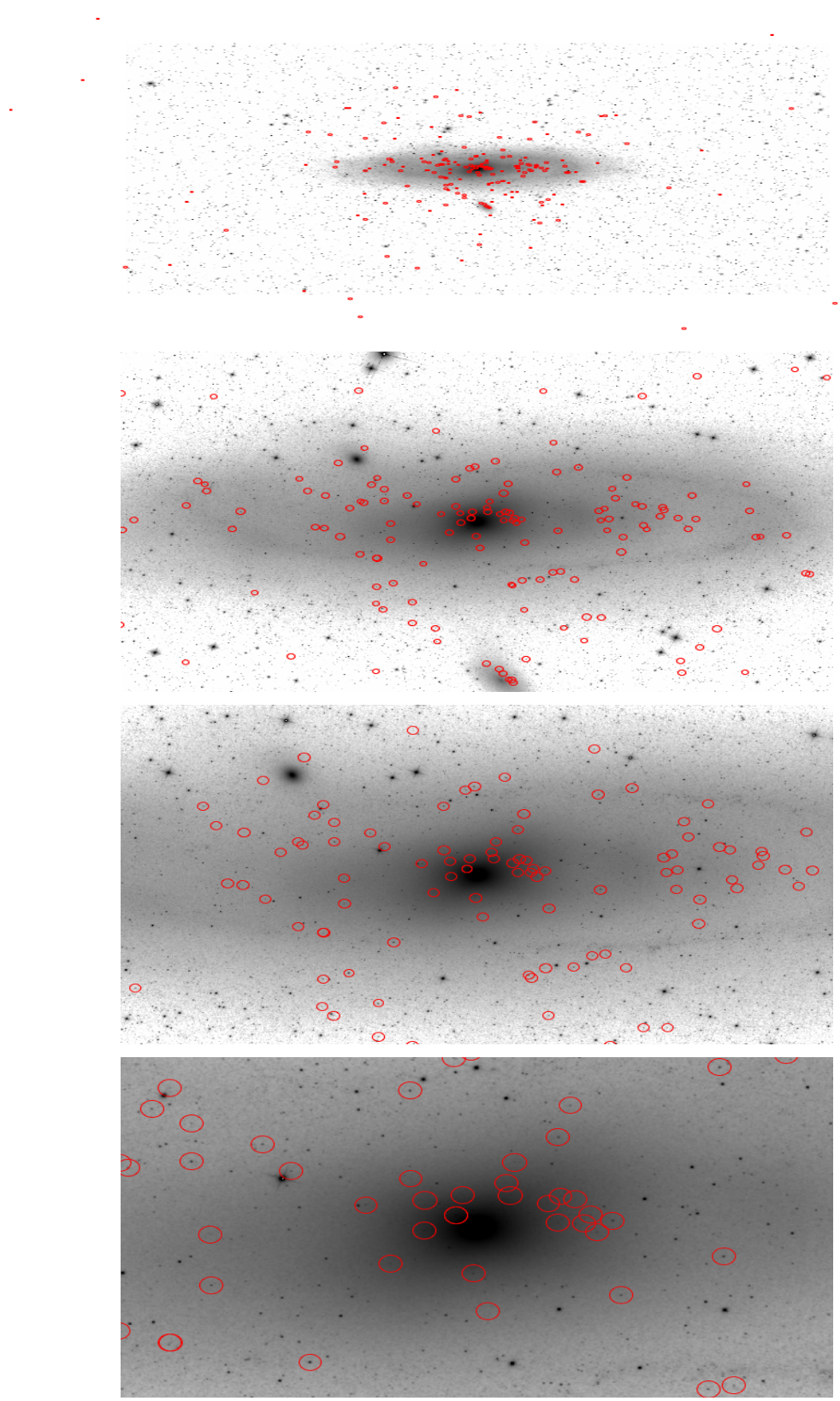

Figure 5.3: The top panel shows RBC confirmed M 31 GC's (red) observed by WISE overlaid on the W1 WISE image of M 31. Subsequent panels show zoomed-in versions of the image.

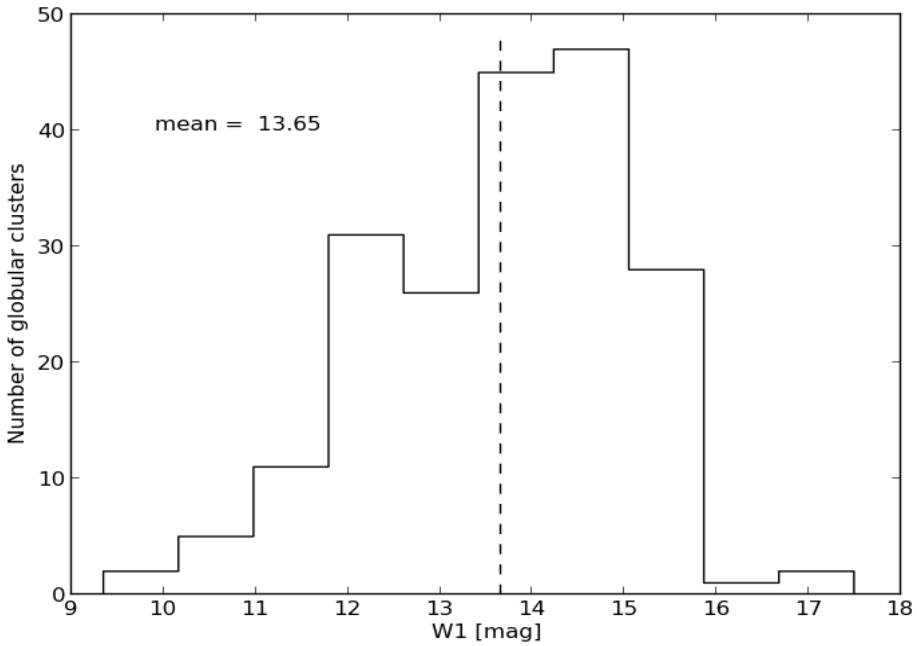

Figure 5.4: W1 magnitude distribution of RBC confirmed M 31 clusters. The mean value of 13.85 mag is marked by the vertical line.

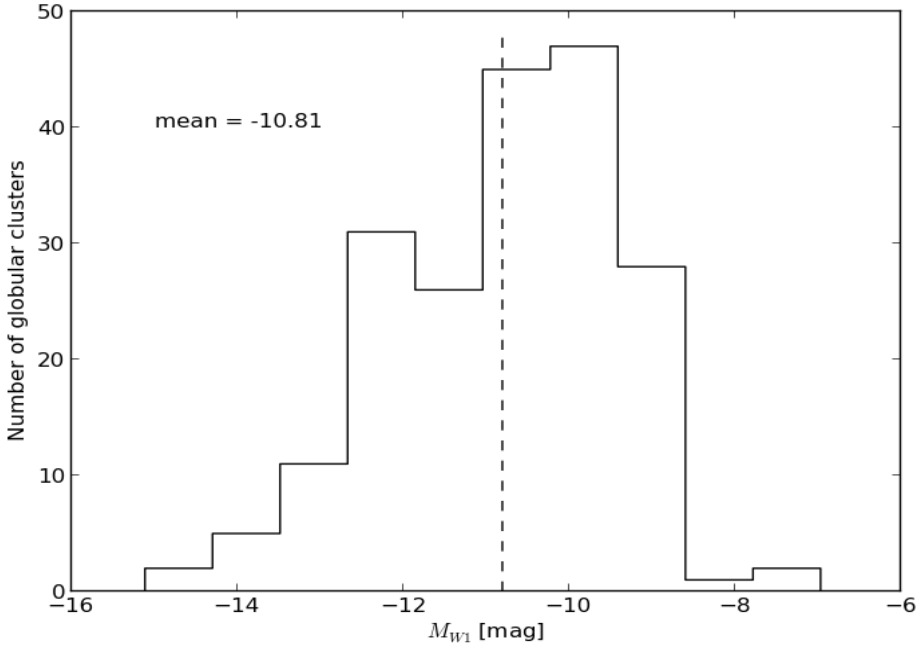

Figure 5.5: W1 absolute magnitude distribution of RBC confirmed M 31 clusters with a mean value of -10.61 mag.

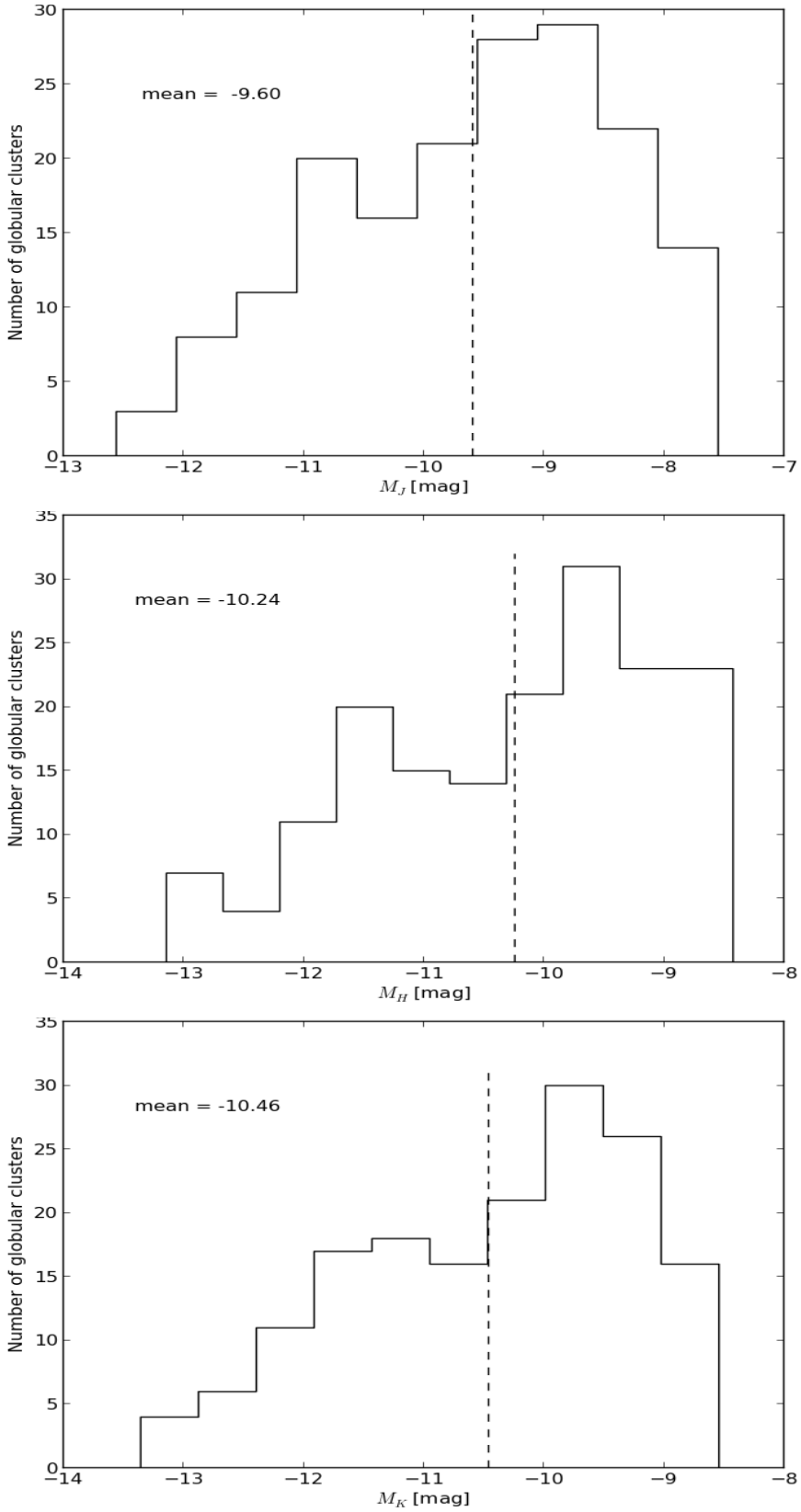

Figure 5.6: The absolute 2MASS magnitude distribution of RBC confirmed M 31 clusters. The top, middle, and bottom panels show the J, H and K-magnitude distributions respectively.

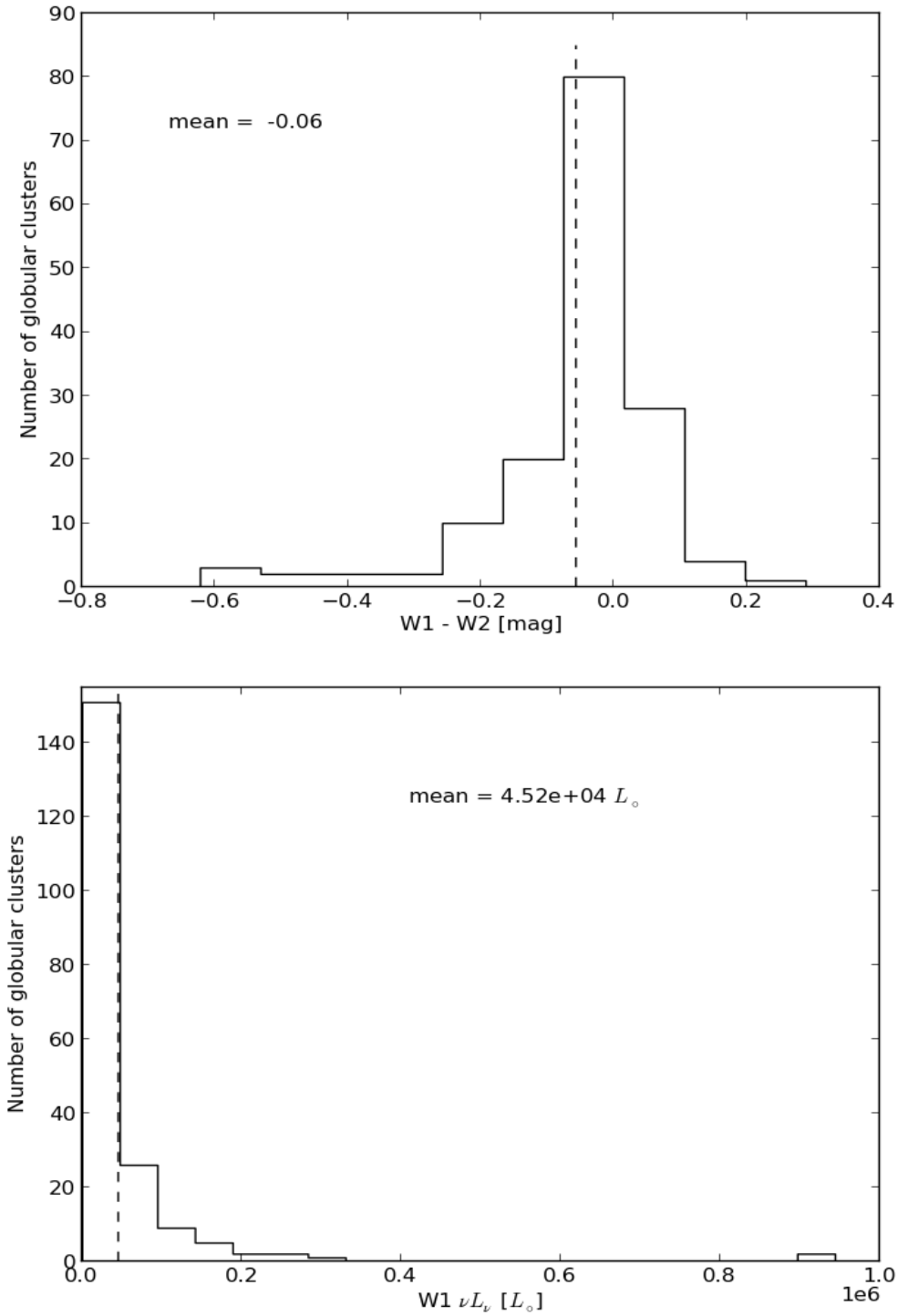

Figure 5.7: The W1-W2 colour distribution (top panel) and W1 luminosity distribution (bottom panel) of RBC confirmed globular clusters. The vertical lines mark the mean values of -0.04 mag and $1.48 \times 10^4 L_\odot$ for the W1-W2 colour and W1 luminosity respectively.

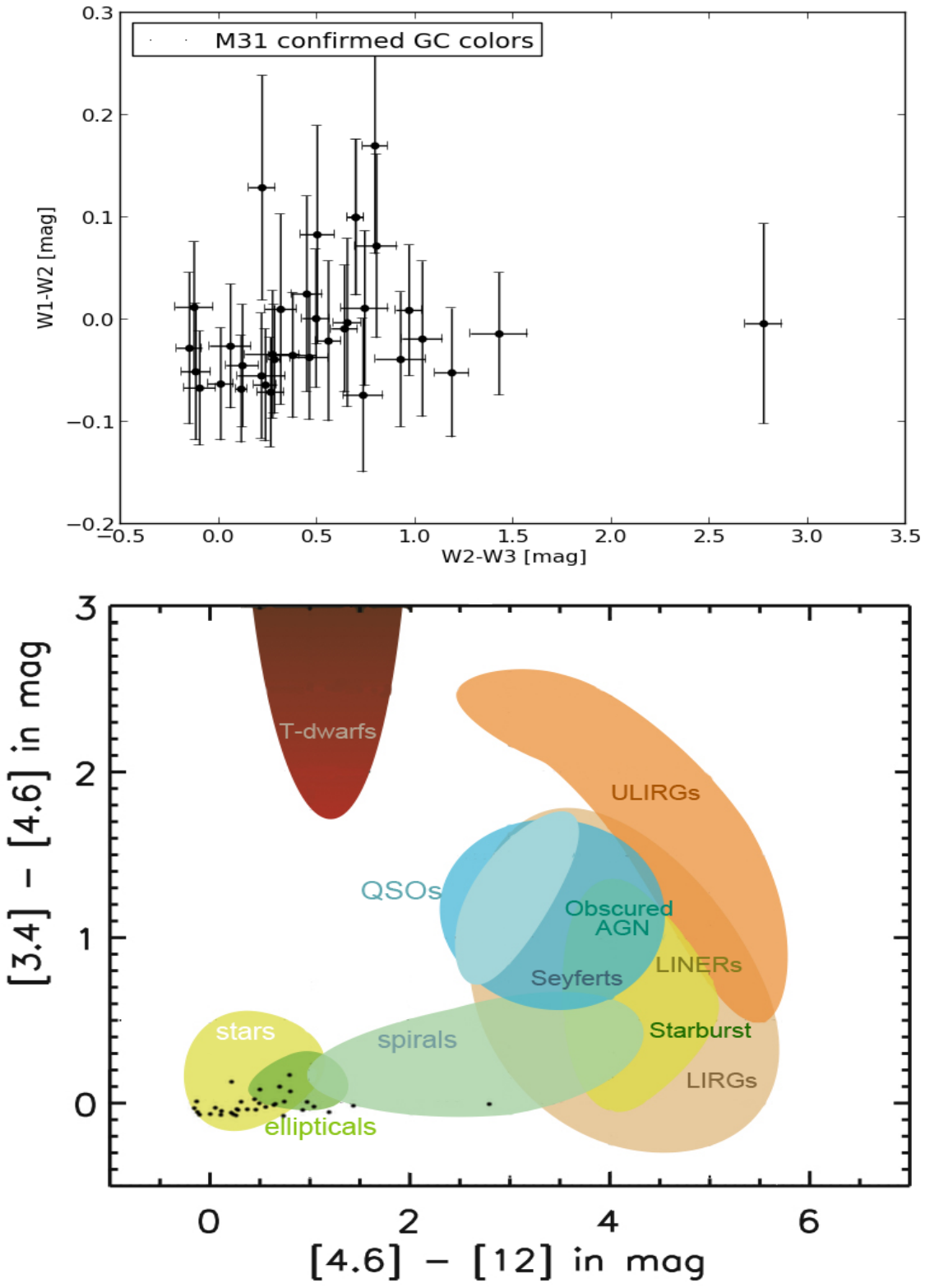

Figure 5.8: The colour-colour distribution of RBC confirmed M 31 GCs with errors $\leq 15\%$. The bottom panel shows the distribution overlaid on the WISE colour-colour plot (Wright et al., 2010).

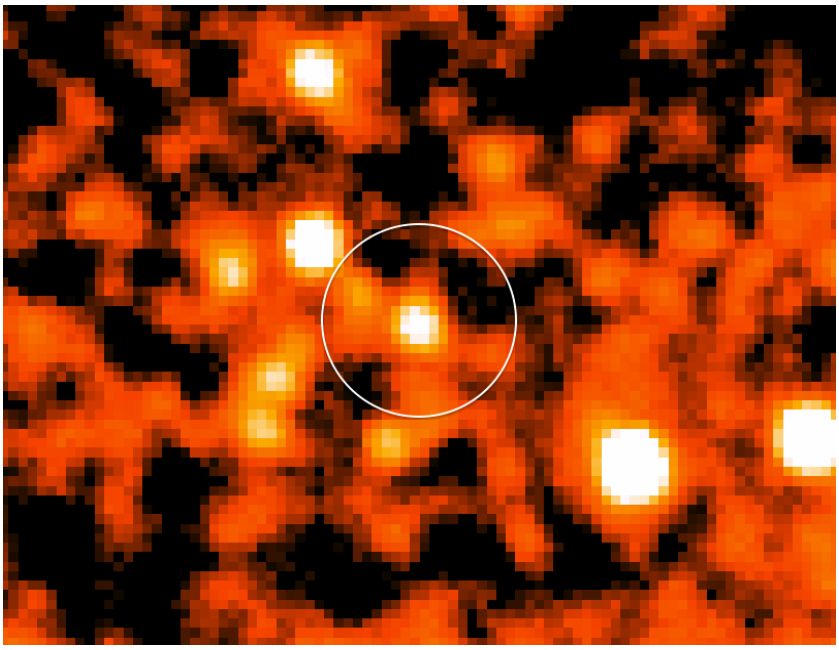

Figure 5.9: W1 image of RBC confirmed GC J004118.72+405715.5, with WISE colours corresponding to a background galaxy. The source could possibly have been misidentified by the RBC as a GC. It has a W1 magnitude of 13.269 mag and a reduced chi^2 of 1.6, indicating a point-like source. The image is 70″ across.

5.1.2 RBC Candidate Clusters

The colour-colour distribution of RBC candidate GC's with errors $\leq 15\%$ was plotted (Fig. 5.11) to see whether their distribution is similar to those of confirmed GC's. The distribution overlaid on the WISE colour-colour plot (Wright et al., 2010) shows that all but one of the candidate GC's have red W2-W3 colours (> 0.3 mag). These are likely background galaxies as they lie in the spiral (and starburst) galaxy range of the WISE colour-colour plot. The only source with colours W1-W2$= 0.118 \pm 0.078$ and W2-W3$= 0.65 \pm 0.15$ mag in the range of those of GC's is WISE source J004934.90+400029.1 (Fig. 5.12); with RA $= 12.3954562°$, Dec $= 40.0080843°$, and a W1 magnitude of 13.265 ± 0.024. The distance between this candidate GC and the potential WISE counterpart is 0.17″, a good position match. The W1 profile-fit photometry reduced chi^2 for the source is 4.0, which indicates an extended source. This suggests that the source is either a background galaxy or a large GC, however, the source's colour may be contaminated by a nearby source. The source is considered to be a good M 31 GC candidate.

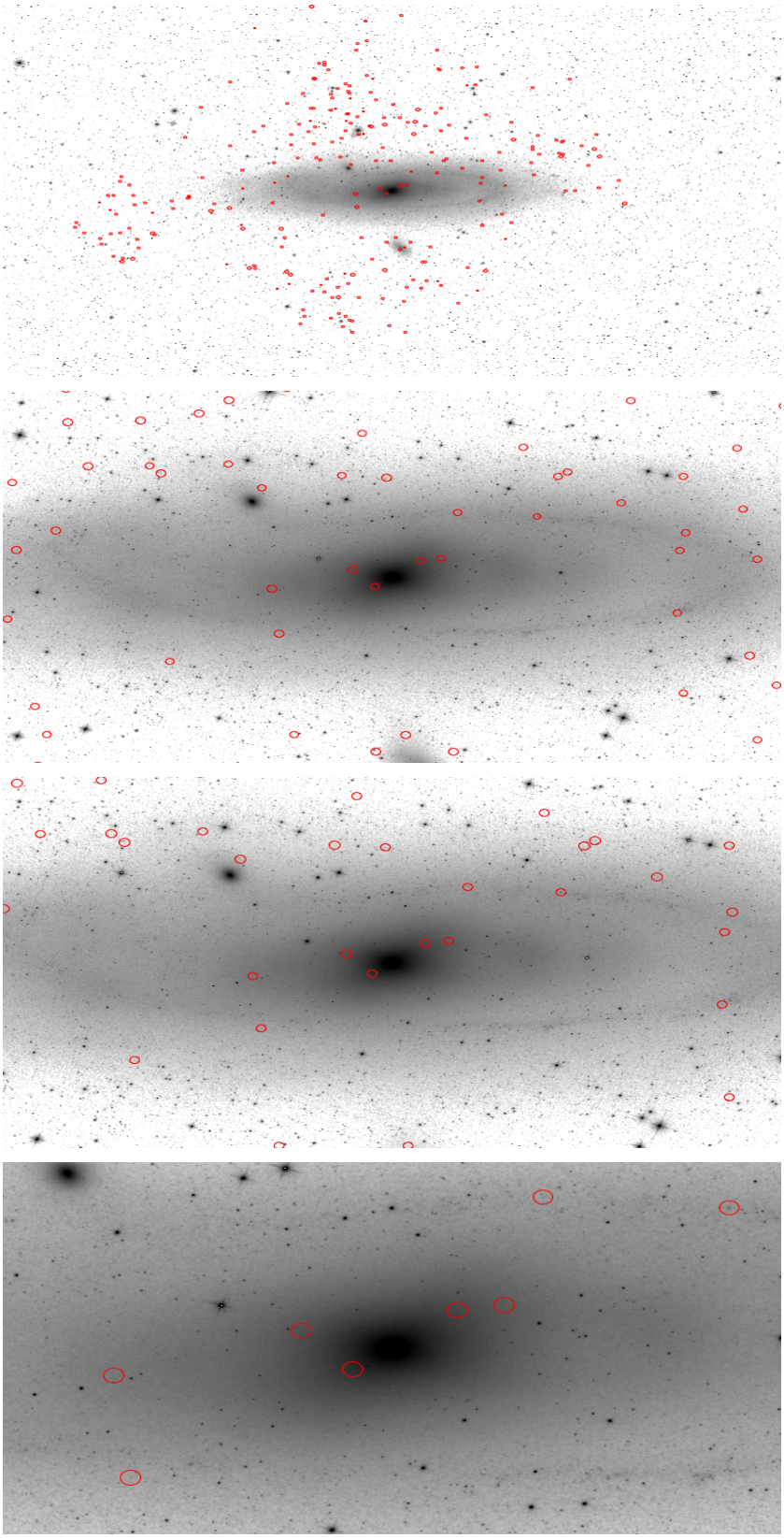

Figure 5.10: The top panel shows RBC candidate M 31 GC's (red) observed by WISE overlaid on the W1 WISE image of M 31. Subsequent panels show zoomed-in versions of the image.

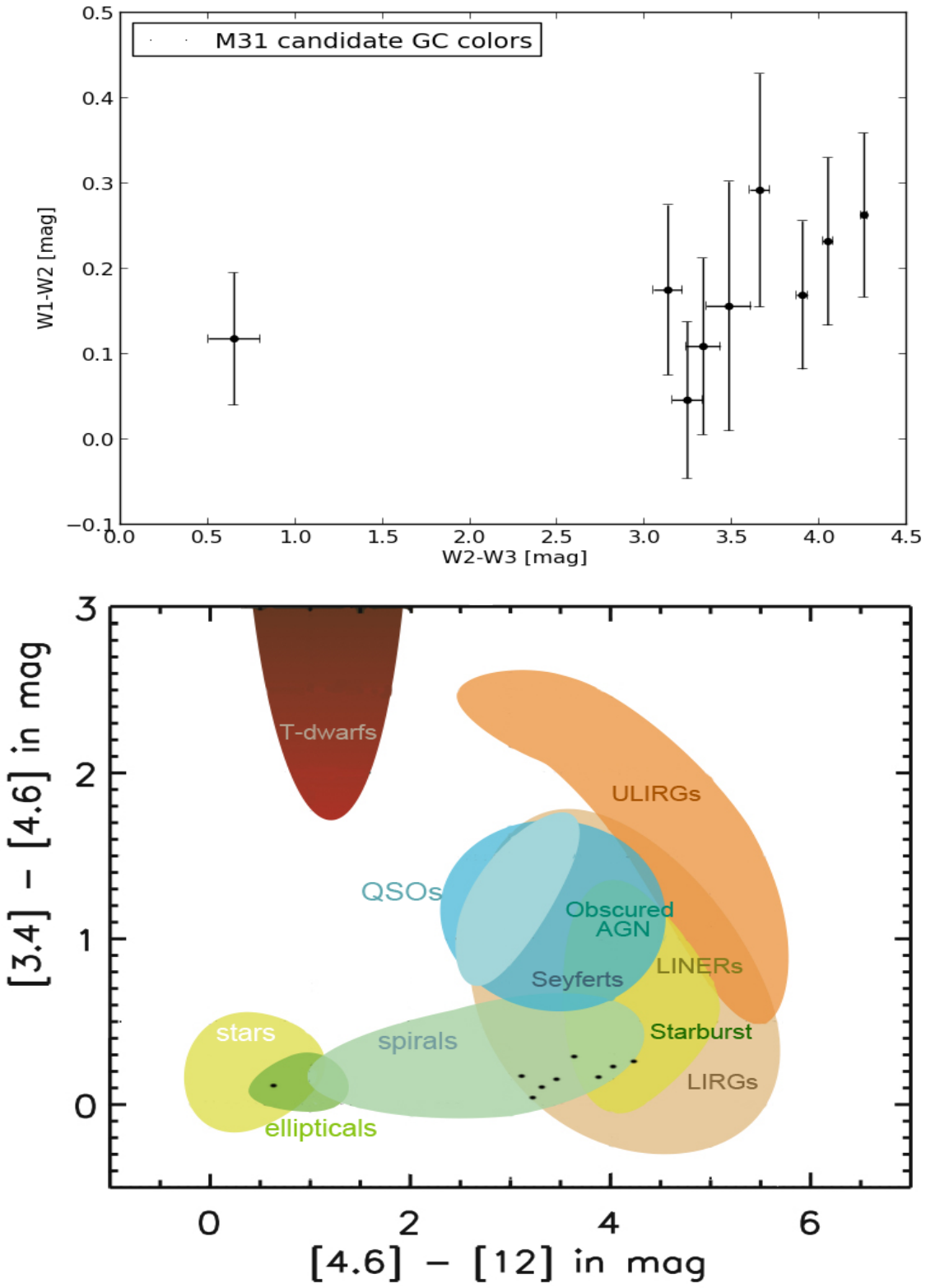

Figure 5.11: The colour-colour distribution of RBC candidate M 31 GCs with errors $\leq 15\%$. The bottom panel shows the distribution overlaid on the WISE colour-colour plot (Wright et al., 2010).

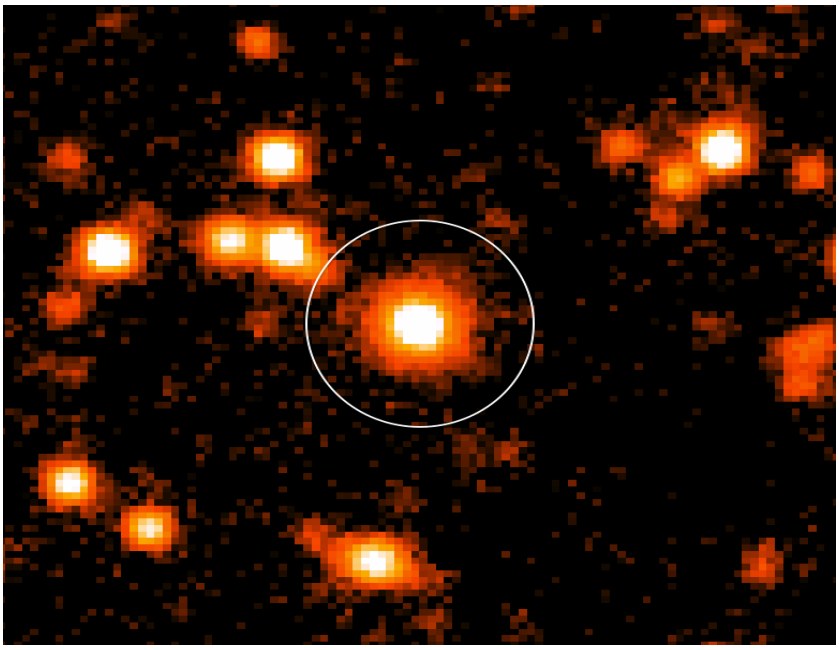

Figure 5.12: W1 image of RBC candidate GC J004934.90+400029.1, with WISE colours that correspond to GCs. It is considered to be a good M 31 GC candidate. The source has a W1 magnitude of 13.265 mag and a reduced chi^2 of 4, indicating a background galaxy, or a large GC. The image is 70″ across.

5.2 Satellite Galaxies

Data for the satellite galaxies was obtained from PAndAS. Only 3 of the 30 satellite galaxies (M 32, M 110 and And IX) are within the boundaries of the WISE M 31 mosaic image (Fig. 5.14). Of the three, only M 32 and M 110, the larger of satellites, are detected with WISE. And IX, at an absolute V-magnitude of -8.3 mag, is one of the faintest galaxies (barely visible in SDSS images)and is seemingly too faint to be detected by WISE (Fig. 5.13). Only the brighter (and larger) of the satellite galaxies, M 32 and M 110 with V-magnitudes -16.5 and -16.4 respectively, are resolved and clearly detected by WISE. The other large M 31 satellites, NGC 0185 and NGC 0147 ($\sim 0.1°$) with V-magnitudes -15.6 and -15.1 mag respectively, are also resolved by WISE and measured here using dedicated mosaics; details below.

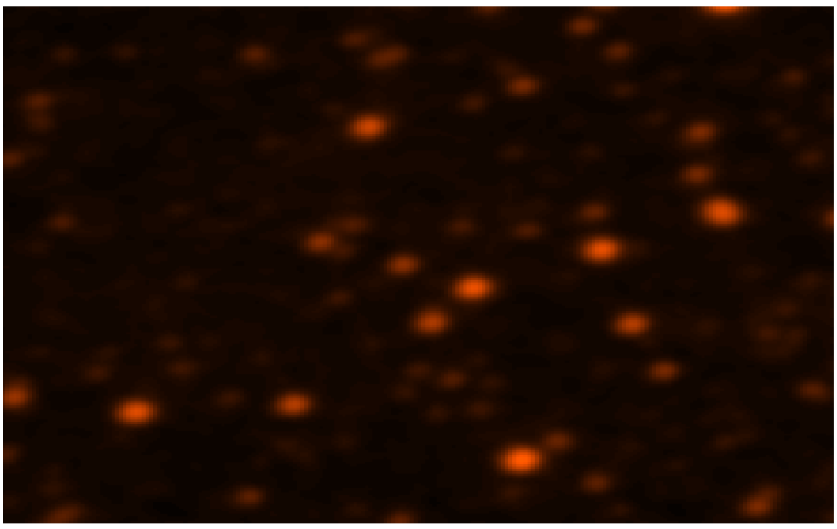

Figure 5.13: W1 image of And IX.

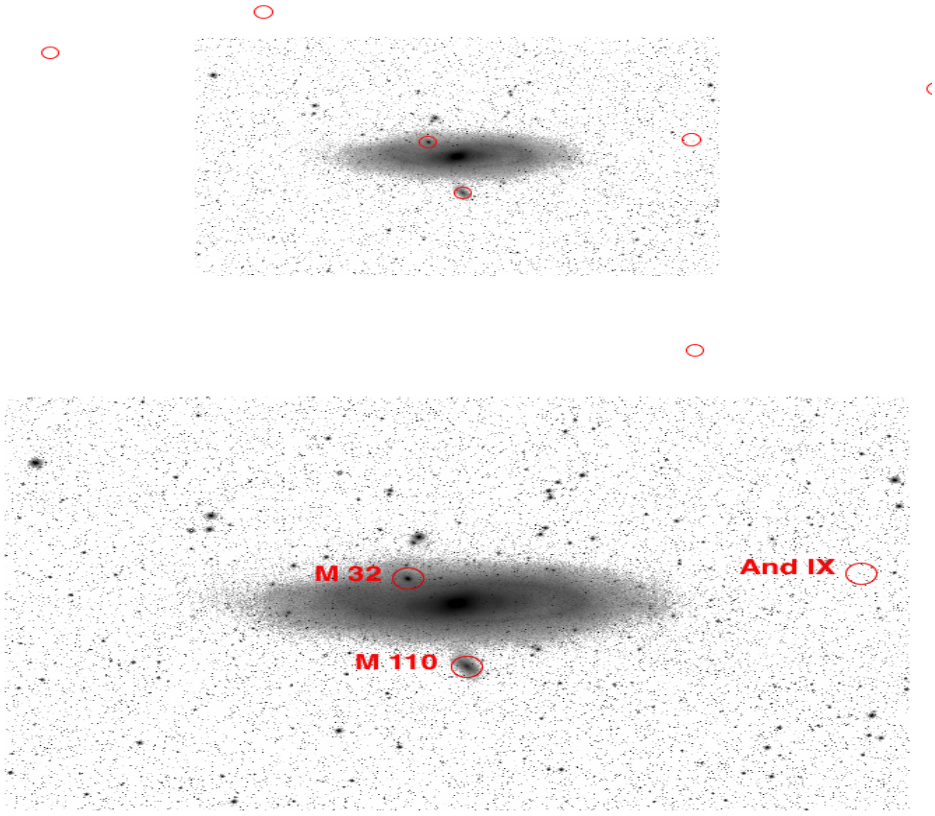

Figure 5.14: The spatial distribution of M 31 satellite galaxies (showing 7 of the 30 here) overlaid on the W1 WISE image. Of the 3 satellites in the image, only the brighter galaxies, M 32 and M 110 are observed.

Images of four of the bright satellites observable with WISE, viz. M 32, M 110, NGC 0147 an d NGC 0185, are shown in Fig. 5.15, 5.16, 5.17 and 5.18 respectively. The top panels in each figure (left to right) show the 3-color WISE image, and the W1, W2, W3 and W4 images of the satellites. The bottom panels show the images cleaned of contaminant foreground stars.

The images were cleaned using an interactive system developed by Jarrett et al. (2013) that identifies foreground stars and assists in shape characterization, surface brightness, and integrated flux measurements. The system identifies the foreground sources using colours (yellow circles, these are masked from the analysis); the images are further inspected by eye and other foreground sources are masked (green circles); then the local background (yellow annulus, placed well outside the influence of the galaxies) is estimated by the most common binned histogram value in the pixel value distribution in the annulus. For the case of M 32 and M 110, the background light from M 31 was first subtracted, rendering a relatively flat and clean background. The blue ellipses represent the 1-σ isophotal radii of the satellite galaxies.

The photometry and characterization measurements for the satellites are shown in Table 5.2 (fiducial isophotal photometry), Table 5.3 (extrapolated fluxes) and Table 5.4 (half-light and concentration indices). The fiducial aperture for each band is based on its 1σ isophotal radius, not just R1 (as presented for M 31 and M 33), since the light observed from long-wavelength bands (W3 and W4) of early-type galaxies (satellites) is too faint to obtain fluxes in the large W1 aperture that are reliable. The flux uncertainties shown include contributions from both the Poisson errors and background estimation errors. M 32 and NGC 0147 have very low W4 SNR which is expected for early-type galaxies and their W4 fluxes are not measurable. Photometry of M 110 was performed by Marleau et al. (2006) using IRAC and MIPS data. The 3.6, 4.5 and 24 μm flux densities were measured to be 438, 266 and 141 mJy, respectively, in a 4.36$'$ area. These are 70-80% fainter the measurements obtained here, however, the 1-σ isophotal areas used in this study were 153$'$ for W1, and 93$'$ for W2 and W3. These are 95-97% larger than the Marleau et al. (2006) area.

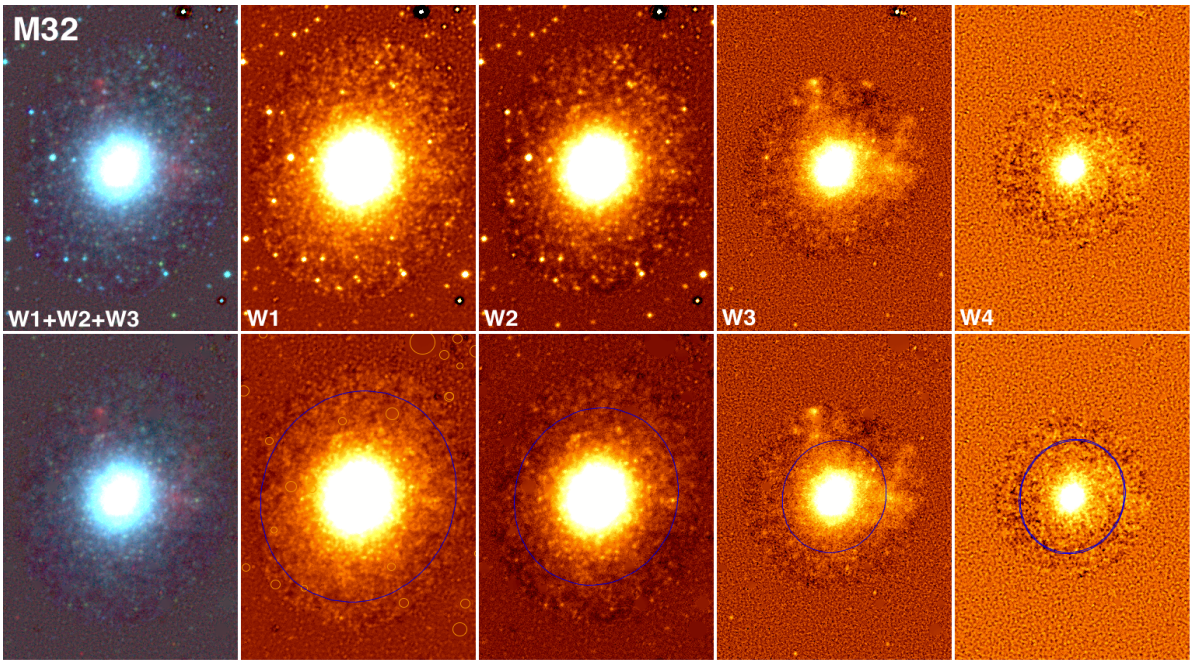

Figure 5.15: The top panel (left to right) shows the 3-color WISE image, and the W1, W2, W3 and W4 images of M 32 with the light from M 31 removed from the images. The bottom panel shows the images cleaned of foreground sources. Images are 11′ across the N-S axis.

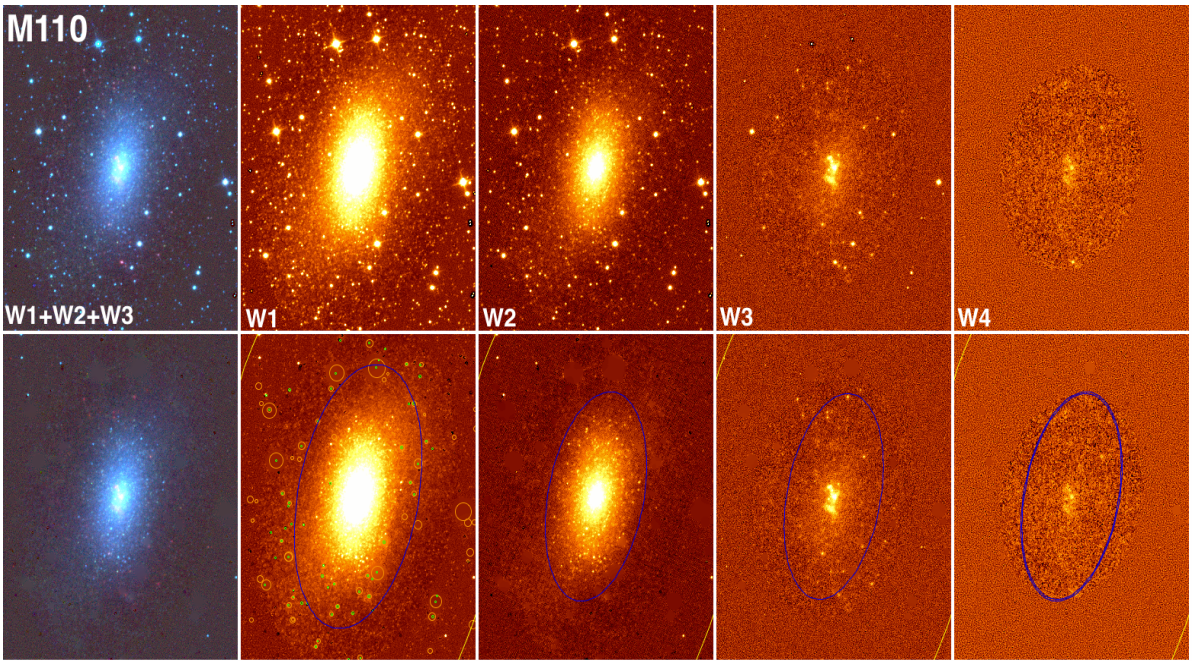

Figure 5.16: The top panel (left to right) shows the 3-color WISE image, and the W1, W2, W3 and W4 images of M 110 with the light from M 31 removed from the images. The bottom panel shows the images cleaned of foreground sources. Images are 23′ across the N-S axis.

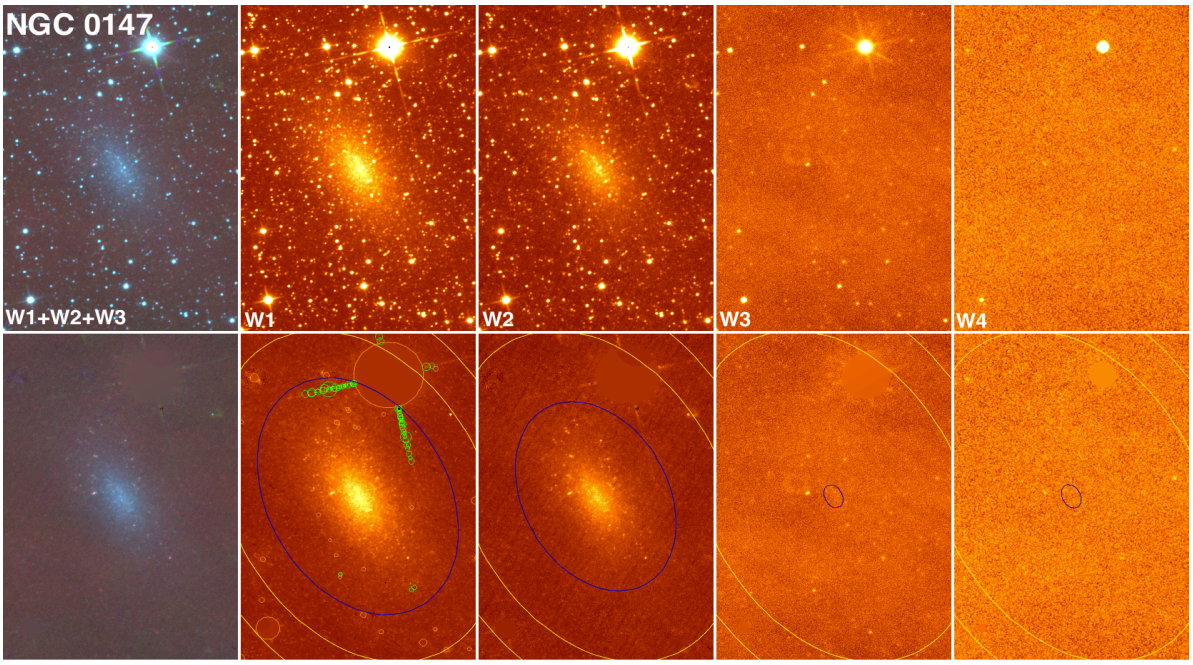

Figure 5.17: The top panel (left to right) shows the 3-color WISE image, and the W1, W2, W3 and W4 images of NGC 0147. The bottom panel shows the images cleaned of foreground sources. Images are 24′ across the N-S axis.

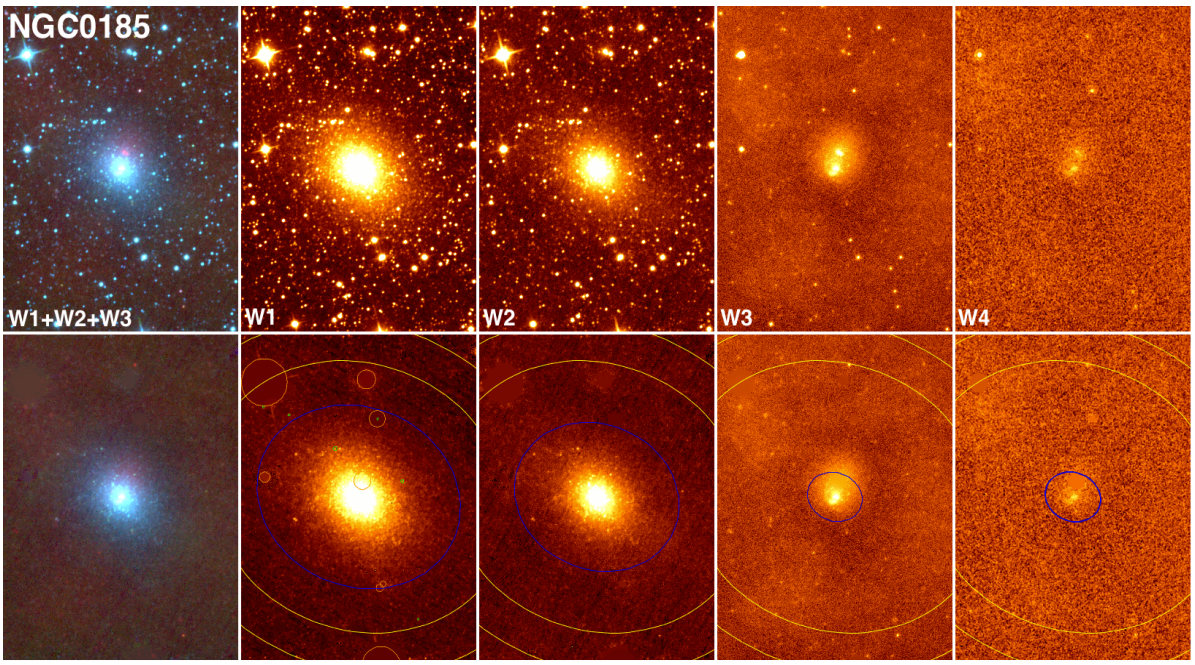

Figure 5.18: The top panel (left to right) shows the 3-color WISE image, and the W1, W2, W3 and W4 images of NGC 0185. The bottom panel shows the images cleaned of foreground sources. A bright-star persistence artifact is seen in the W3 image, and appears as a red cloud just north of the nucleus in the 3-color image. The artifact has been largely mitigated (lower panel). Images are 21′ across the N-S axis.

Table 5.2: WISE Isophotal-aperture Photometry of Bright M 31 Satellites.

Name	R.A. (°)	Decl. (°)	Axis Ratio	P.A. (°)	$R1_{iso}$ (″)	$R2_{iso}$ (″)	$R3_{iso}$ (″)	$R4_{iso}$ (″)	W1 (mJy)	W2 (mJy)	W3 (mJy)	W4 (mJy)	W1-W2 [mag]	W2-W3 [mag]	W1-W3 [mag]	W3-W4 [mag]
M 32	10.67439	40.86511	0.862	165.8	216.6	178.1	115.3	115.3	3008.0	1592.3	467.5	-	-0.038	0.592	0.554	-
									±31.5	±16.7	±4.9	-	±0.016	±0.016	±0.016	-
M 110	10.09201	41.68550	0.497	168.2	594.3	462.2	462.2	462.2	2065.1	978.6	277.6	154.1	-0.040	0.555	0.515	0.723
									±49.5	±38.5	±3.2	±7.0	±0.050	±0.045	±0.028	±0.051
NGC 0147	8.30052	48.50901	0.690	26.3	555.1	435.0	53.3	0.0	779.6	381.1	9.1	0.0	-0.006	-2.127	-2.133	0.866
									±8.2	±4.0	±0.3	±0.0	0.016	0.033	0.033	0.0245
NGC 0185	9.74029	48.33795	0.838	70.0	425.1	337.7	114.3	114.3	987.7	502.0	179.2	114.6	-0.028	0.805	0.777	0.876
									±10.3	±5.3	±2.0	±3.7	±0.016	±0.017	±0.017	±0.037

Notes. The fiducial aperture for each band is based on its 1σ isophotal radius. The colour measurements are derived from matched aperture photometry.

Table 5.3: WISE Extrapolated Photometry.

Name	$R1_{ext}$ ($''$)	$W1_{ext}$ (Jy)	$R2_{ext}$ ($''$)	$W2_{ext}$ (Jy)	$R3_{ext}$ ($''$)	$W3_{ext}$ (Jy)	$R4_{ext}$ ($''$)	$W4_{ext}$ (Jy)
M 32	325.0	3035±32	347.0	1594±17	339.5	495±5	0.0	0.0
M 110	891.5	2178±50	891.5	1049±39	887.0	290±4	693.4	159±7
NGC 0147	1446.1	861±9	1342.4	436±4	0.0	0.0	0.0	0.0
NGC 0185	637.6	1040±11	1233.2	554±6	245.0	213±2	210.4	121±4

Notes. The extrapolated photometry is the sum of the isophotal photometry in Table 5.2 and the integrated double-Sersic fit to the elliptical-radial surface brightness carried out to R_{ext}.

Table 5.4: WISE Half-light Surface Brightness and Concentration.

Name	$R1_e$ ($''$)	$W1_e$ (Jy)	C1	$R1_e$ ($''$)	$W1_e$ (Jy)	C1	$R1_e$ ($''$)	$W1_e$ (Jy)	C1	$R1_e$ ($''$)	$W1_e$ (Jy)	C1
M32	28.65	14.131	4.92	27.15	14.080	4.62	30.30	13.665	4.35	0.00	-	0.00
M 110	235.05	18.465	3.21	202.35	18.296	3.03	152.55	17.157	3.36	119.40	15.915	2.97
NGC 0147	231.30	19.793	3.10	211.30	19.700	2.91	0.00	-	0.00	0.00	-	0.00
NGC 0185	128.00	18.514	3.59	119.10	18.405	3.60	66.10	16.244	2.73	54.60	15.075	2.58

Notes. The half light is relative to the extrapolated integrated flux shown in Table 5.3, and the concentration index is the ratio of the 3/4 light-radius to the 1/4 light-radius.

Chapter 6

Summary and Future Work

6.1 Summary

In this dissertation, the global properties of the M 31 system have been addressed using WISE mid-IR photometry combined with ancillary near-IR data. The infrared photometric properties of the galaxy were measured and contrasted across the electromagnetic spectrum to create a multi-wavelength catalogue of the galaxy's global properties.

- A statistical classification scheme was developed to distinguish the foreground MW population from the M 31 population in the WISE images, using WISE and 2MASS fluxes and colors. This was done to remove the foreground contaminating light, thereby obtaining a clean measurement of M 31 and its system. The scheme was found to be effective, requiring only minor ($< 1\%$) completeness corrections for the total flux densities due to WISE incompleteness from blending and confusion.

- Basic measurements of the cleaned M 31 system were made. The WISE 1-σ isophotal integrated flux densities were measured to be 276 ± 3 Jy, 146 ± 2 Jy, 180 ± 2 Jy and 128 ± 2 Jy for the W1, W2, W3 and W4 bands, respectively. The values are comparable with measurements from previous *Spitzer* studies but are on average higher than their *Spitzer* counterparts. This was not surprising since WISE covers the entire region of M 31 including the extended disk and halo, therefore, the local background could be adequately calculated, and the total flux extracted accordingly. For M 33, the 1-σ isophotal flux measurements of 17.2 ± 0.2 Jy, 10.2 ± 0.1 Jy, 34.8 ± 0.4 Jy and 44.3 ± 0.5 Jy for the W1, W2, W3 and W4 bands, respectively, compared well with their *Spitzer* counterparts, validating the source classification scheme.

- The aggregate stellar mass, derived from the W1 (3.4 μm) and W2 (4.6 μm) bands, was estimated to be 8.7×10^{10} $M_{\odot}$, which is 40% larger than the measurement

recently derived using multi-wavelength data (*Herschel*, *Spitzer*, etc.). M 31 was found to be more massive than the Milky Way based on previous results, however, it should be noted that uncertainties in stellar mass estimates are comparable to the difference between the measurements.

- The global dust-obscured SFRs derived from the W3 (12 μm) and W4 (22 μm) bands, respectively, which ranged from 0.3 to 0.7 $M_{\odot}yr^{-1}$, were comparable to some previous estimations but were higher than the SFR derived from the recent HELGA survey. The specific SFR estimations for M 31 range between 0.003 and 0.008 Gyr^{-1}. This suggests a quiescent evolution for the galaxy, M 31 is nearing the end of its bulge building phase.

- The average W1 luminosity of GCs in M 31 is 10 times the average blue luminosity, showing that GCs emit more radiation in the infrared compared to the optical bands. It was found that M 31 GCs are twice as massive as Galactic GCs. A study of the colour photometry (with errors $< 15\%$) of the GCs revealed two sources of interest. The first, catalogued cluster J004118.72+405715.5 ($RA = 10.3280075°$, $DEC = 40.9543207°$), from the Revised Bologna Catalogue. This source has WISE colours that correspond to a background galaxy, therefore, it could have been mis-identified as a GC. The second, candidate cluster J004934.90+400029.1 ($RA = 12.3954562°$, $DEC = 40.0080843°$), which has WISE colours which correspond to those of stars and ellipticals. This is a good GC candidate and should be investigated further.

- The mid-infrared properties of satellite galaxies M 32, M110, NGC 0147 and NGC 0185, which are large and bright enough to be resolved by WISE, were measured. The integrated flux measurements were found to be comparable to *Spitzer* measurements that are available for these galaxies.

6.2 Future Prospects

The statistical classification scheme developed, in this study, to separate the MW population from the M 31 system can be extended to other nearby galaxies. It will especially be useful in the WISE High Resolution Galaxy Atlas (WHRGA) Project which involves constructing a mid-infrared source catalogue and high-resolution image Atlas of the largest nearby galaxies (Jarrett et al. 2012, 2013). Accurate global mid-infrared properties of these galaxies can be obtained by adequately identifying and removing the contaminant Milky Way population.

The mid-infrared bands of WISE reveal the older stellar content in M 31, as well as its dusty regions where stars are forming. GALEX's ultraviolet bands, on the other hand, detect the young massive stellar population located in the spiral arms of the galaxy. WISE and GALEX are complementary. Therefore, they will be used in unison

towards the comprehension of the fundamental processes of formation and evolution in Andromeda, and spiral galaxies in general.

WISE is a good instrument to investigate GC photometric properties of galaxies. As shown in this study, it can be used to discover GC candidates for further investigation. WISE can also be used to characterize the photometric and surface brightness mid-infrared properties of bright (V-magnitudes < -14 mag) and large (> 0.1 deg) satellite galaxies. In 2017, there will be additional epochs available from the ongoing NEOWISE mission, which will allow more GCs and satellites to be detected by WISE[1].

[1] http://neowise.ipac.caltech.edu/

Appendix A

Source Number Density Plots for the M 31 Shells

In this appendix, the LogN-LogS differential source counts (W1, W2, W3 and W4) and the color distributions (W1-W2, W2-W3, W3-W4 and J-K_s) are shown for all 32 elliptical shells.

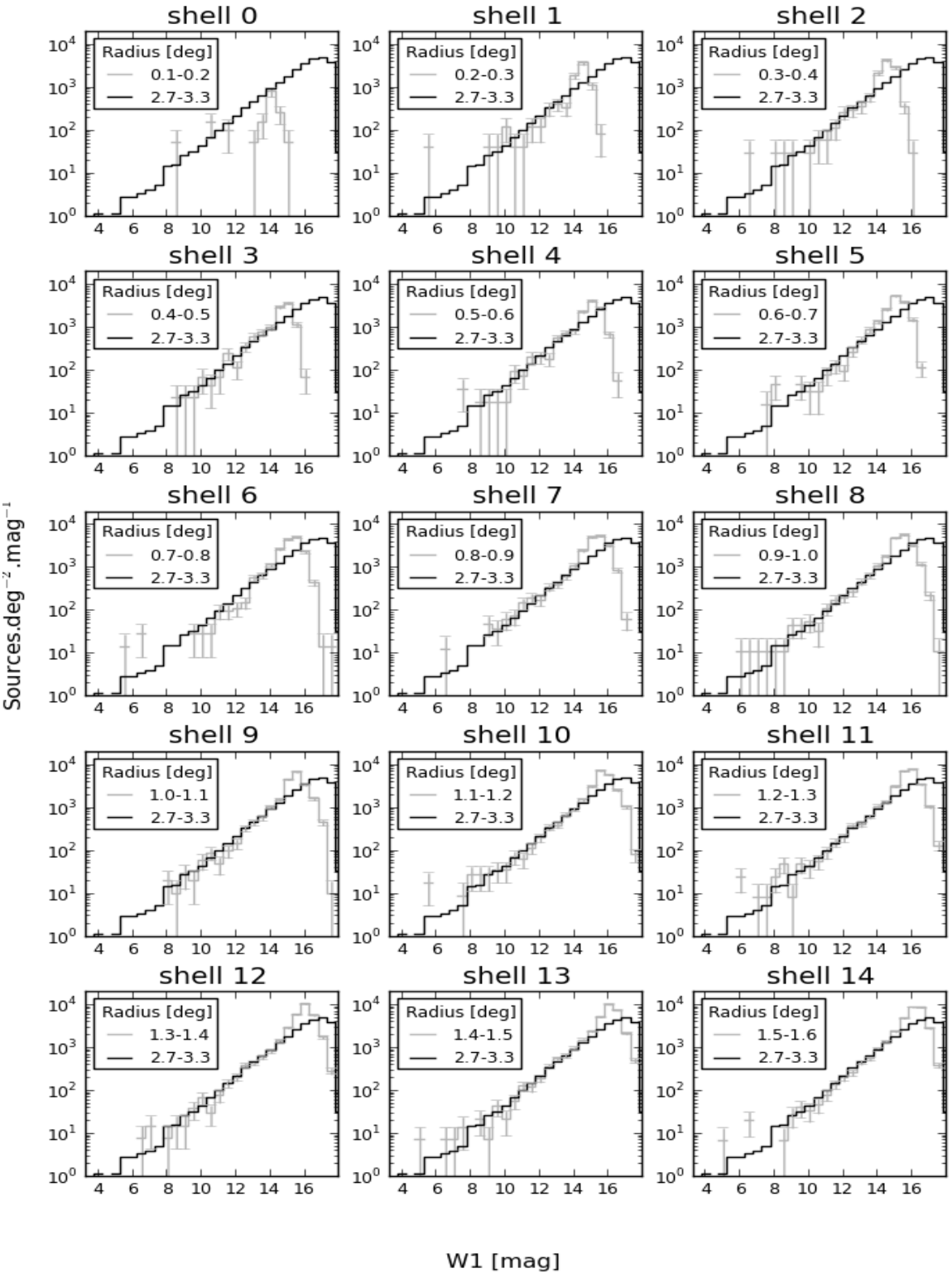

Figure A.1: W1 source number density for the different shells (see Figure 2.1) with errors shown.

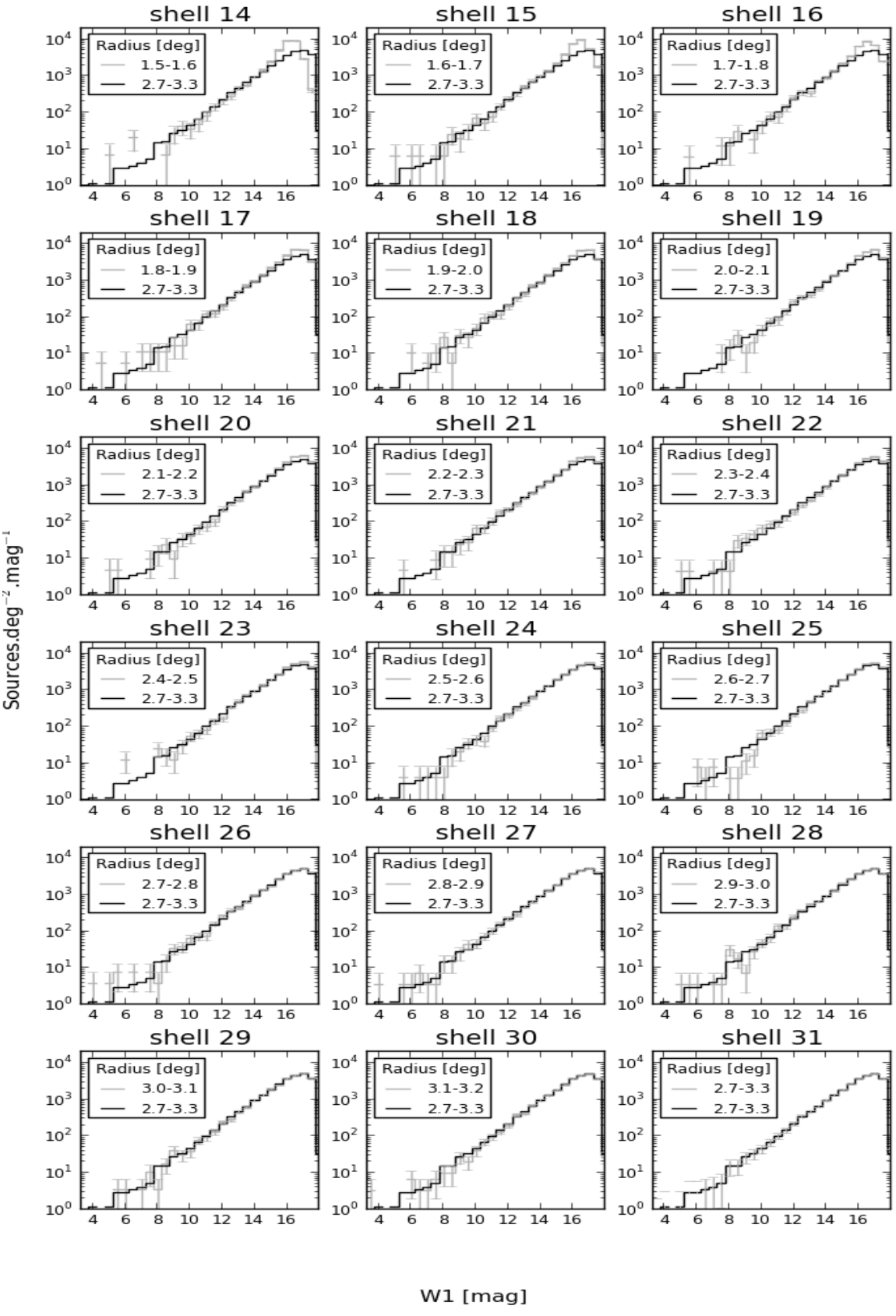

Figure A.1: Continued

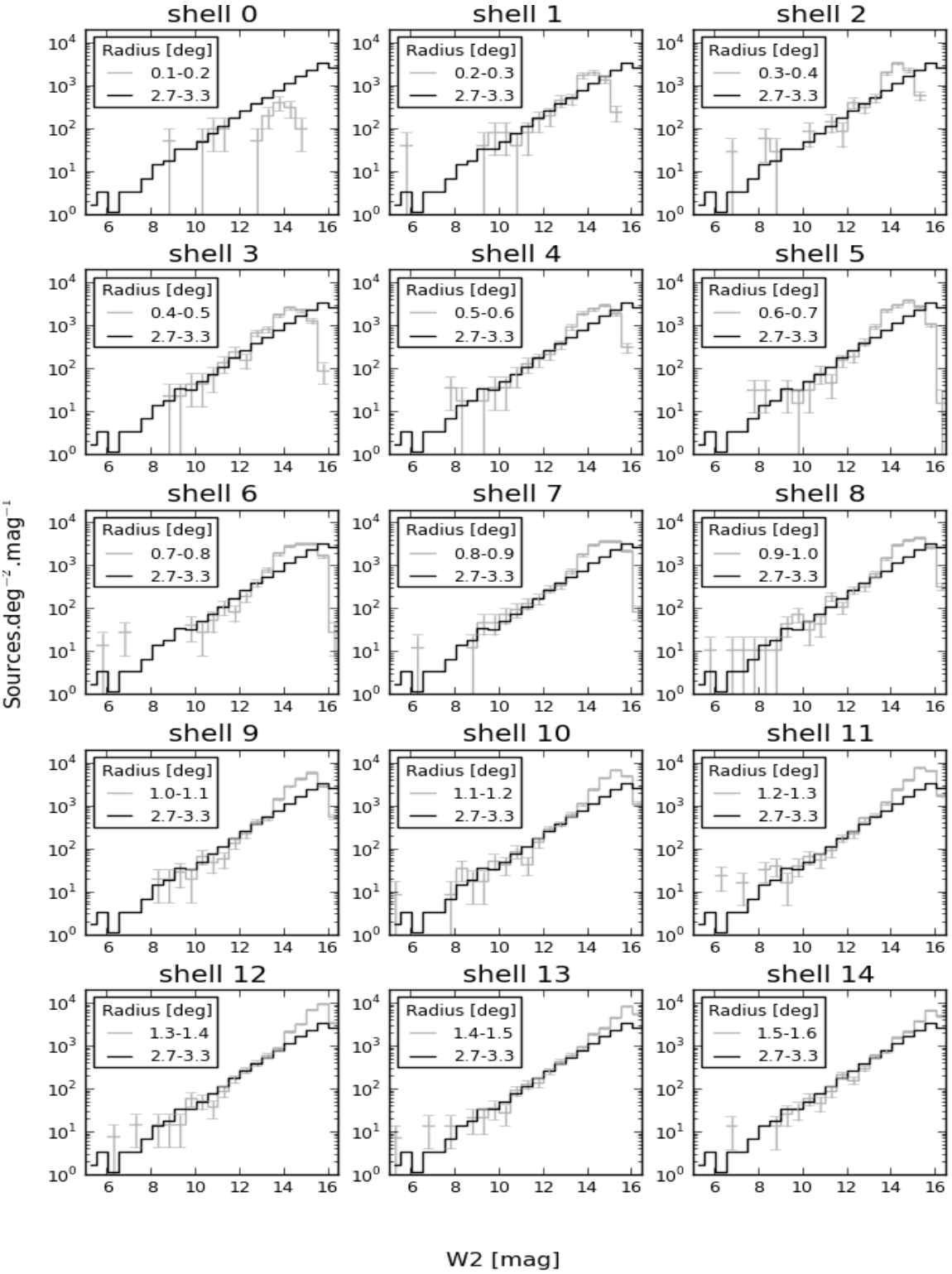

Figure A.2: W2 source number density for the different shells (see Figure 2.1) with errors shown.

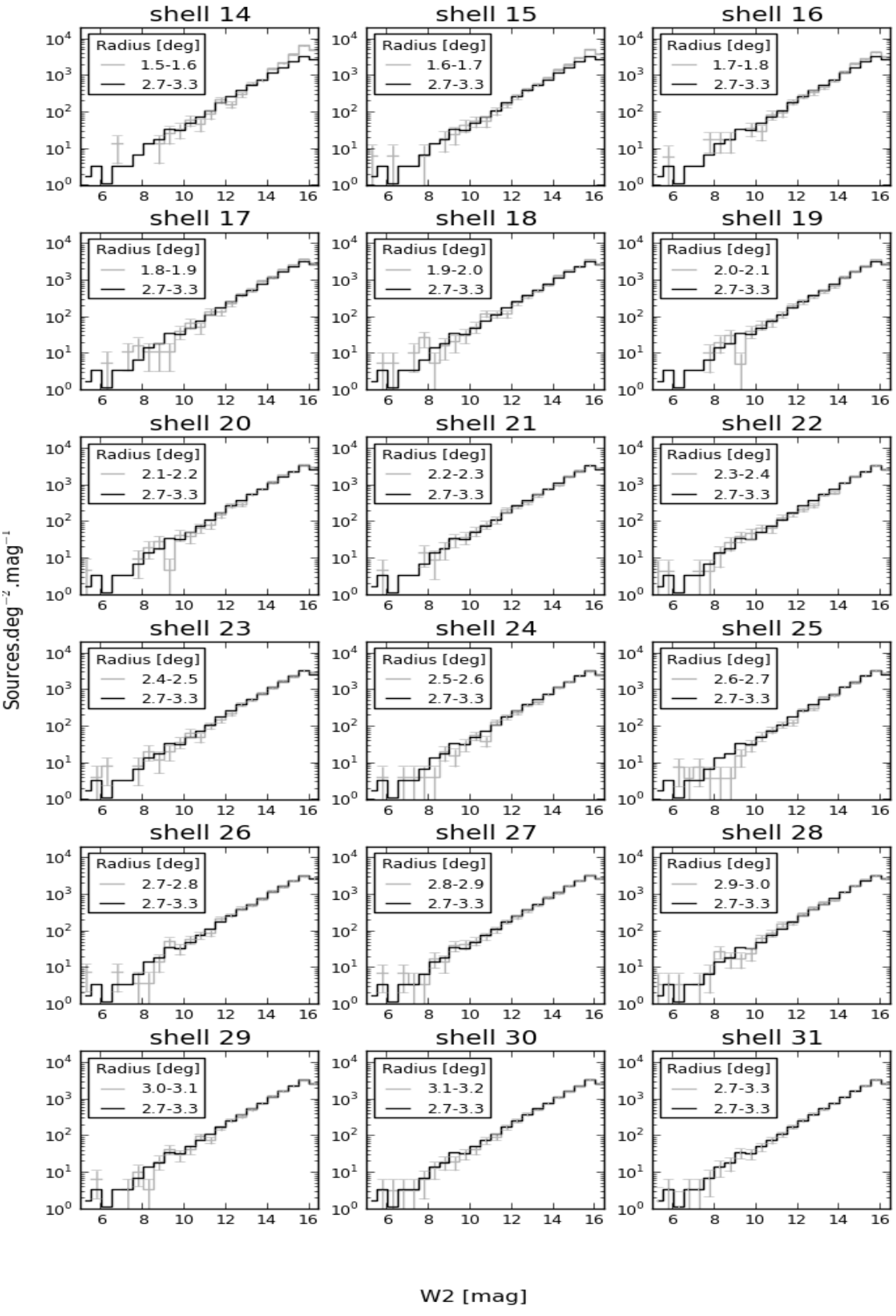

Figure A.2: Continued

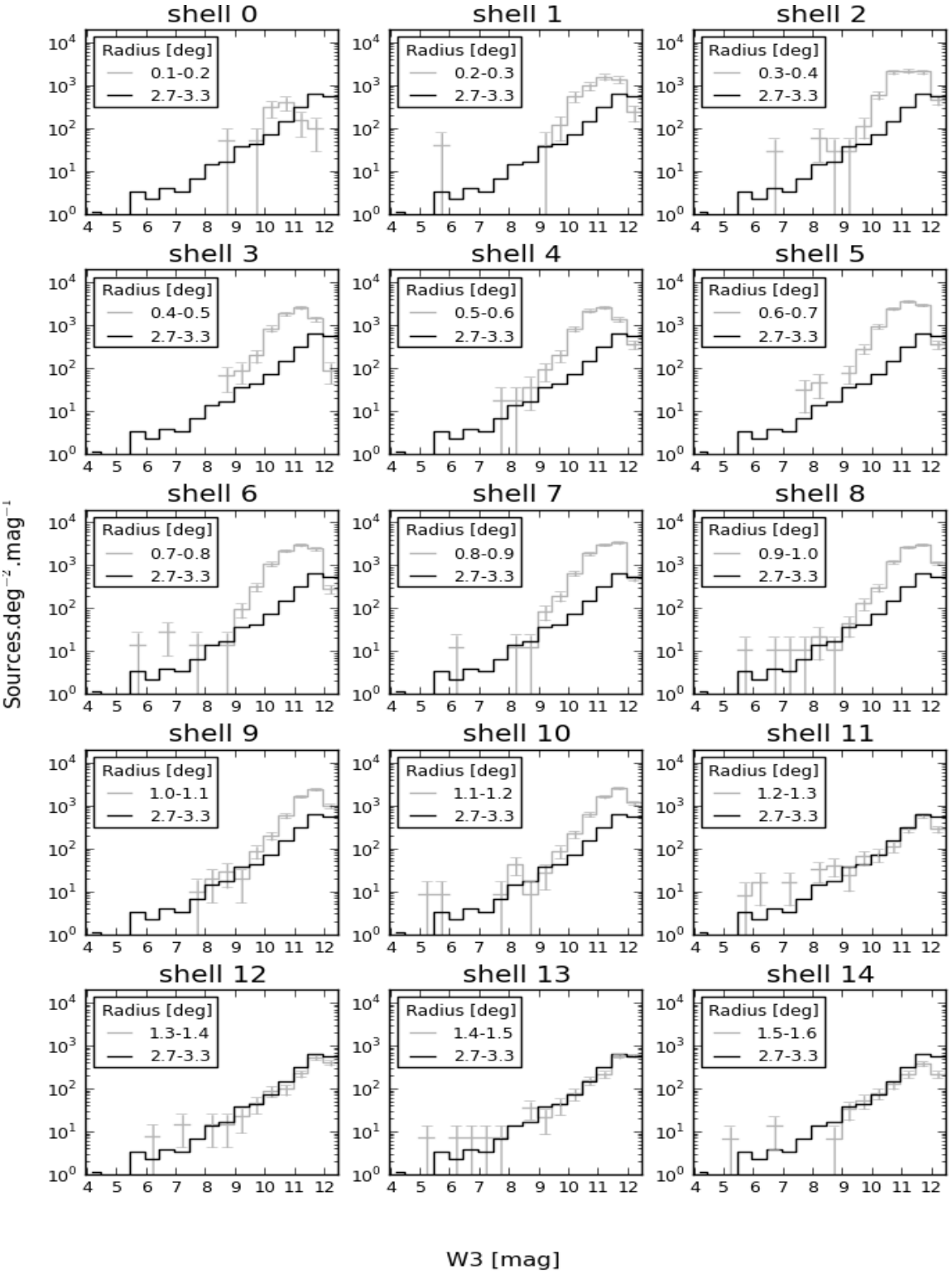

Figure A.3: W3 source number density for the different shells (see Figure 2.1) with errors shown.

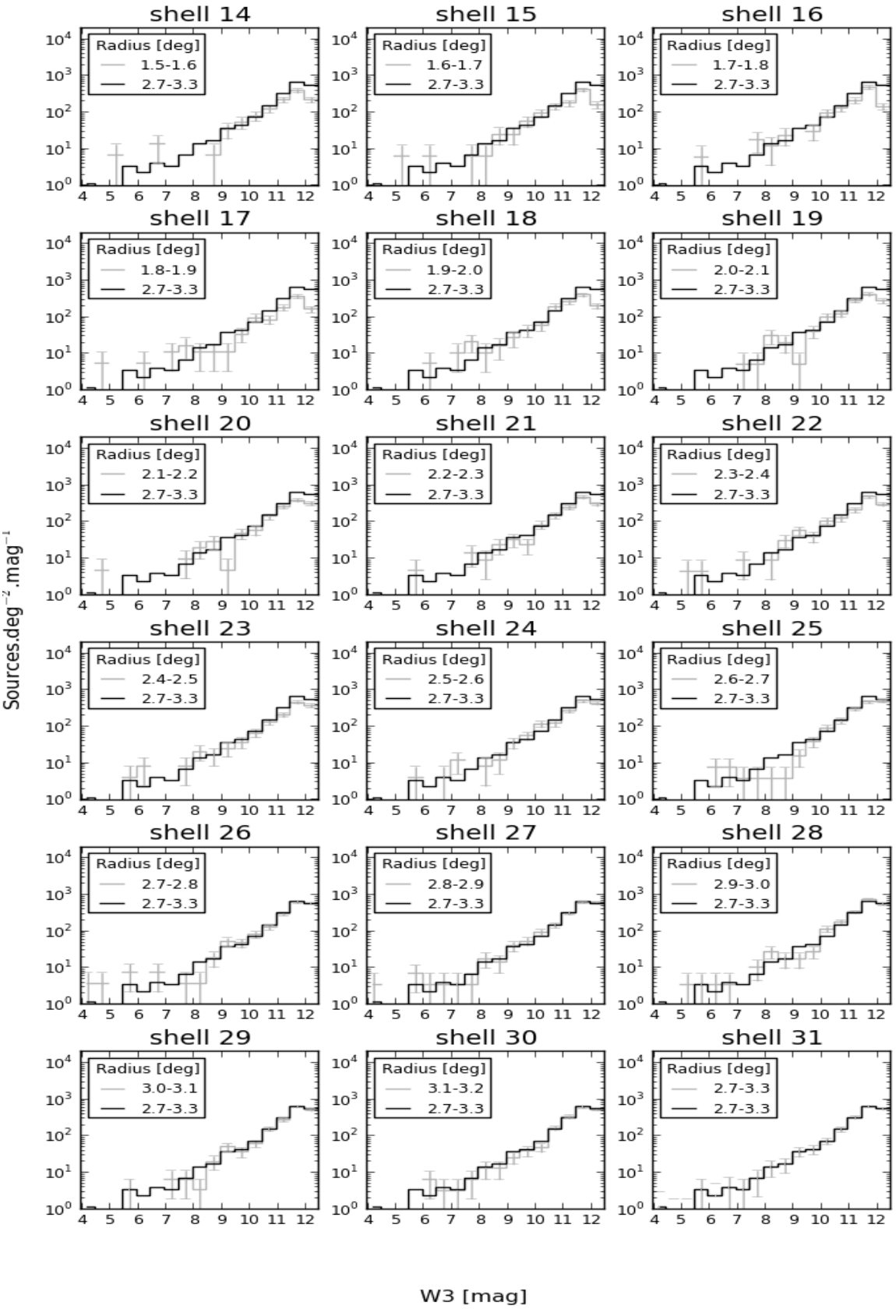

Figure A.3: Continued

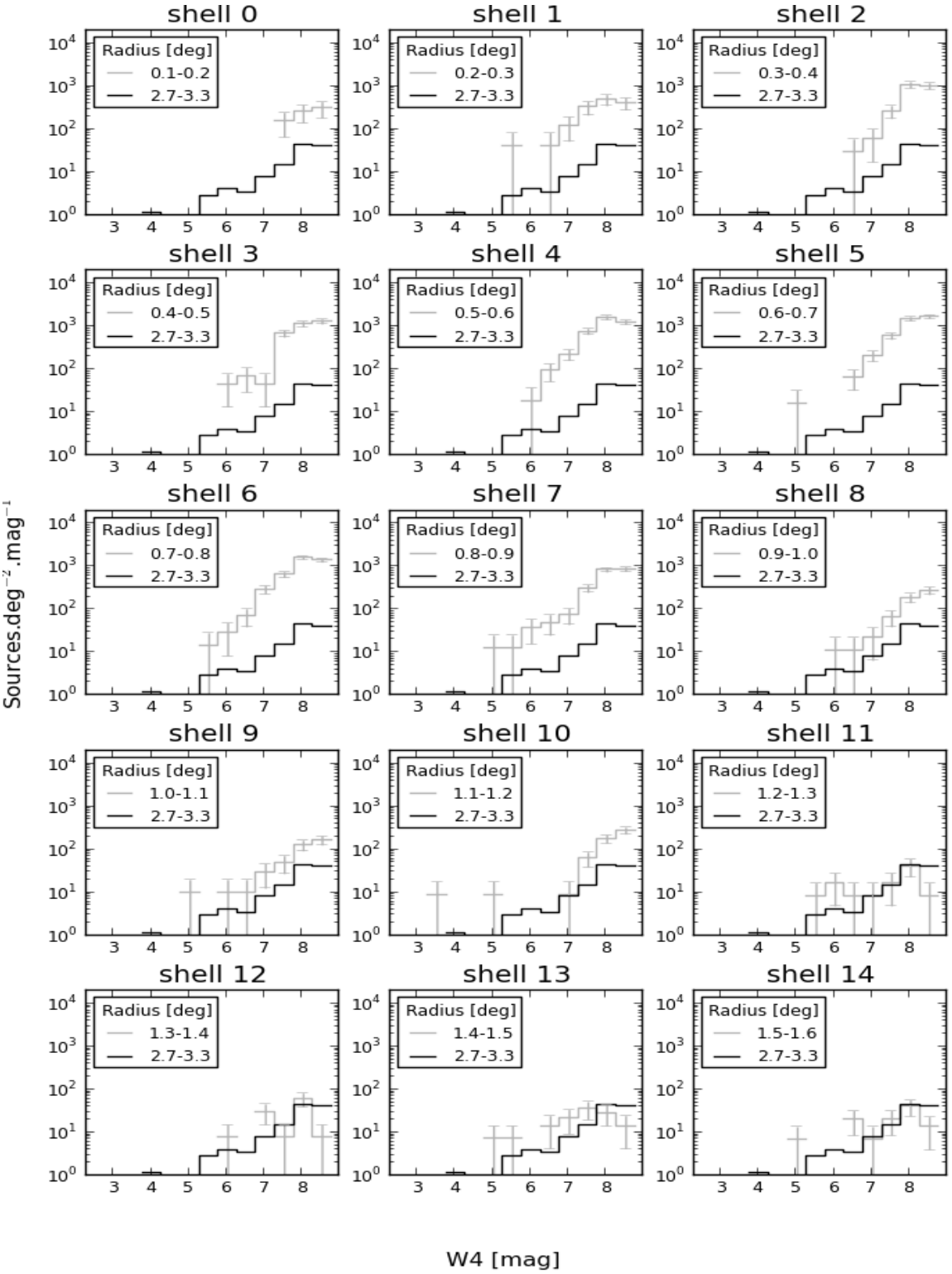

Figure A.4: W4 source number density for the different shells (see Figure 2.1) with errors shown.

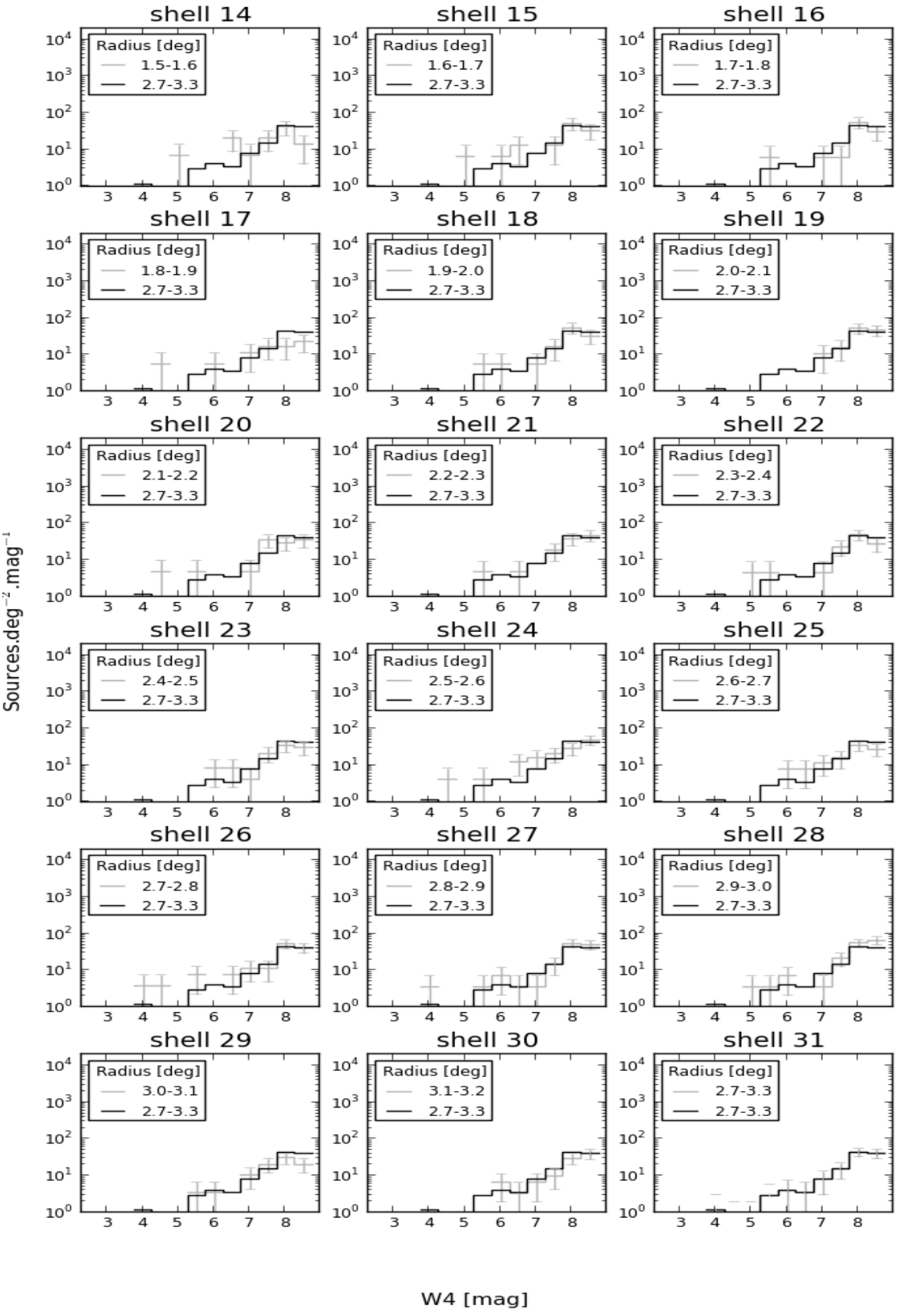

Figure A.4: Continued

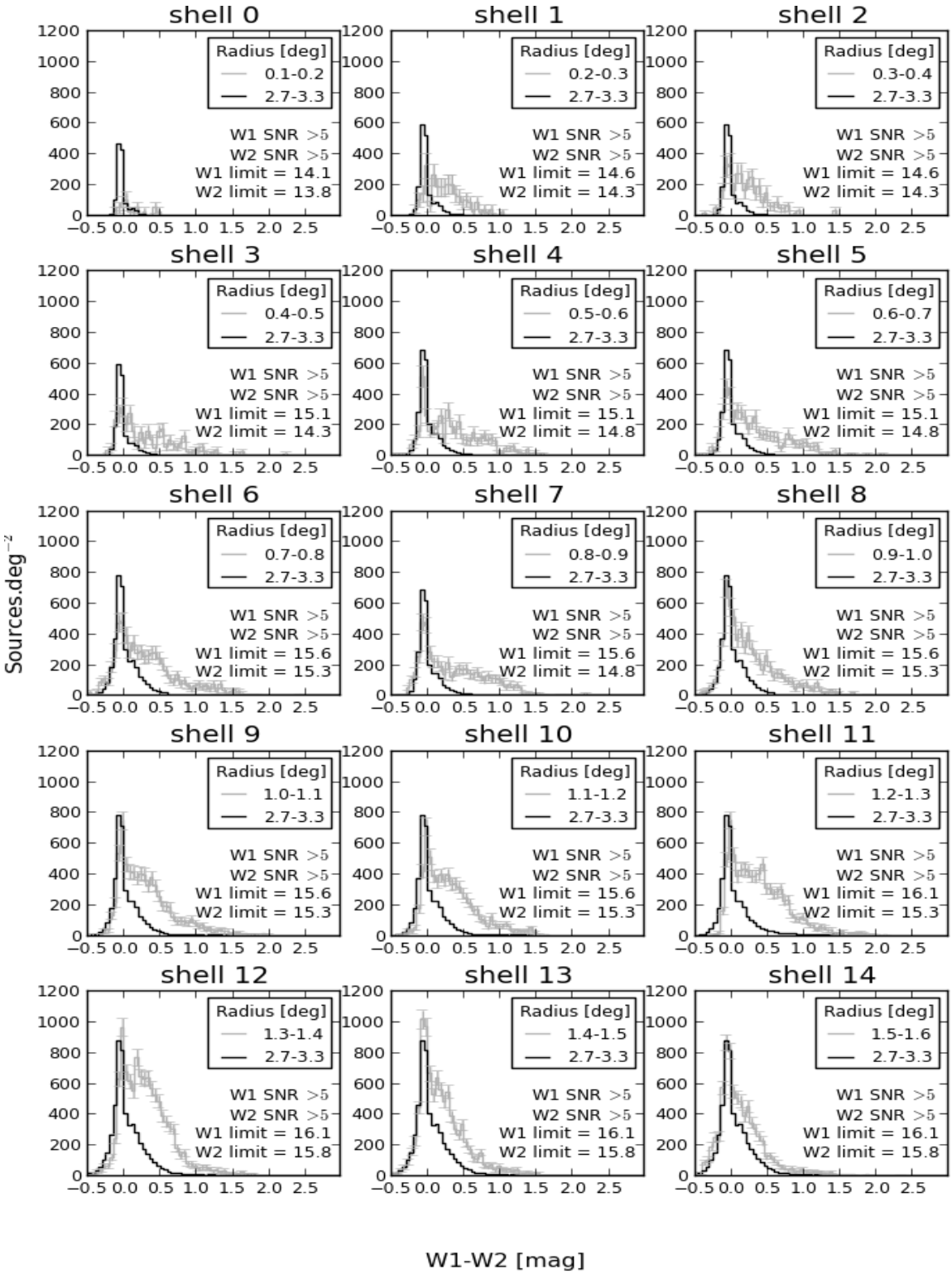

Figure A.5: W1-W2 color histograms for the different shells.

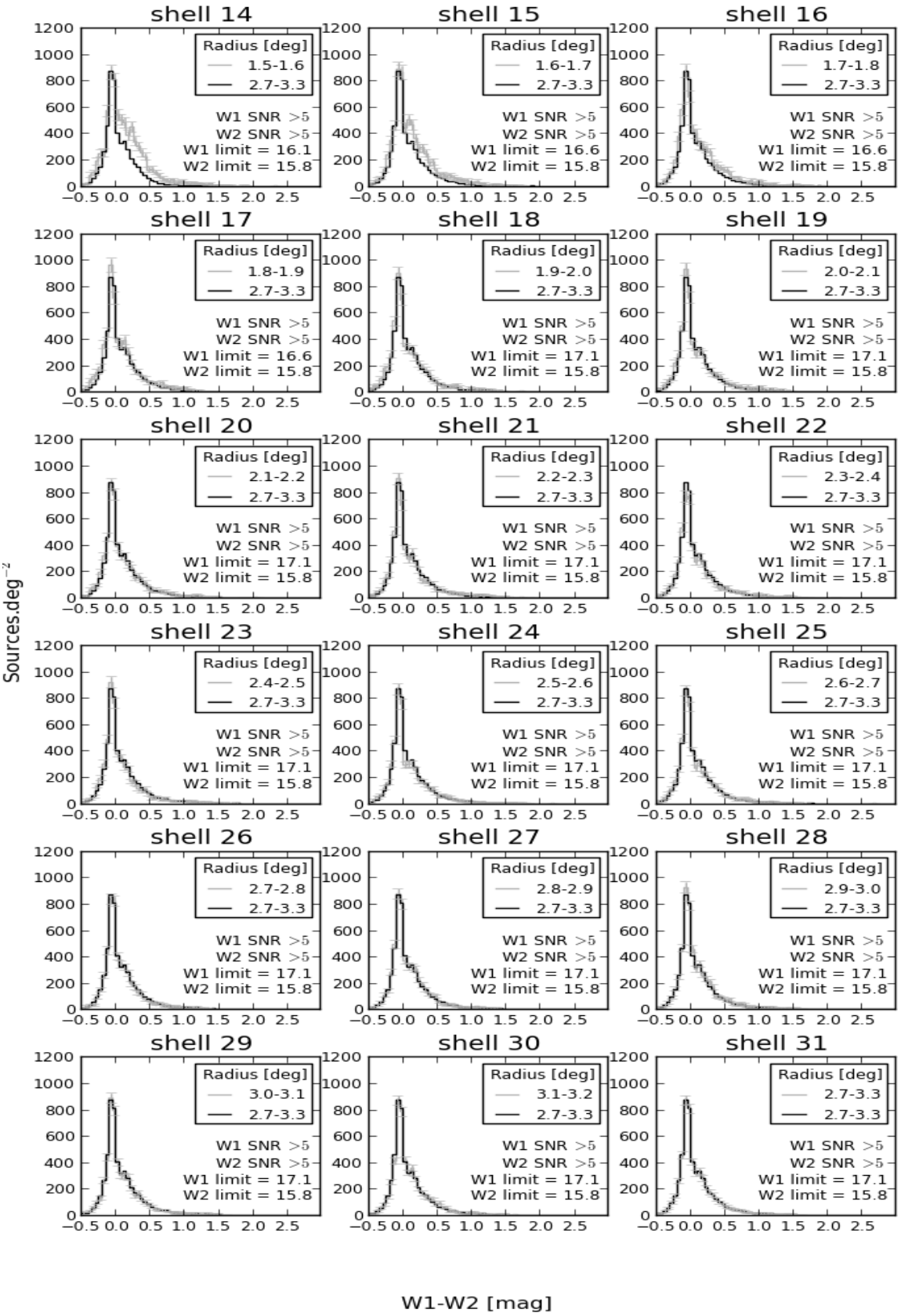

Figure A.5: Continued

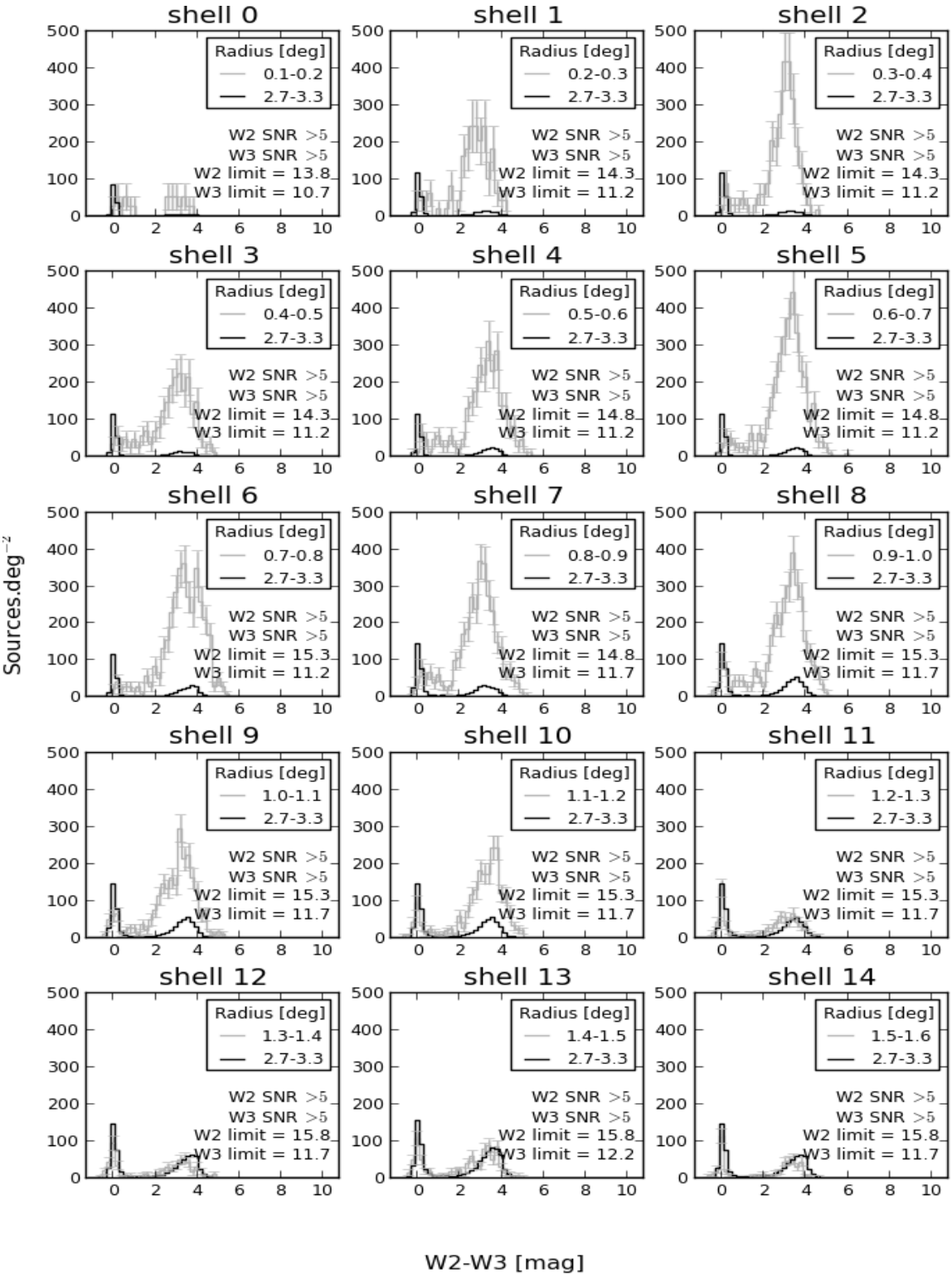

Figure A.6: W2-W3 color histograms for the different shells.

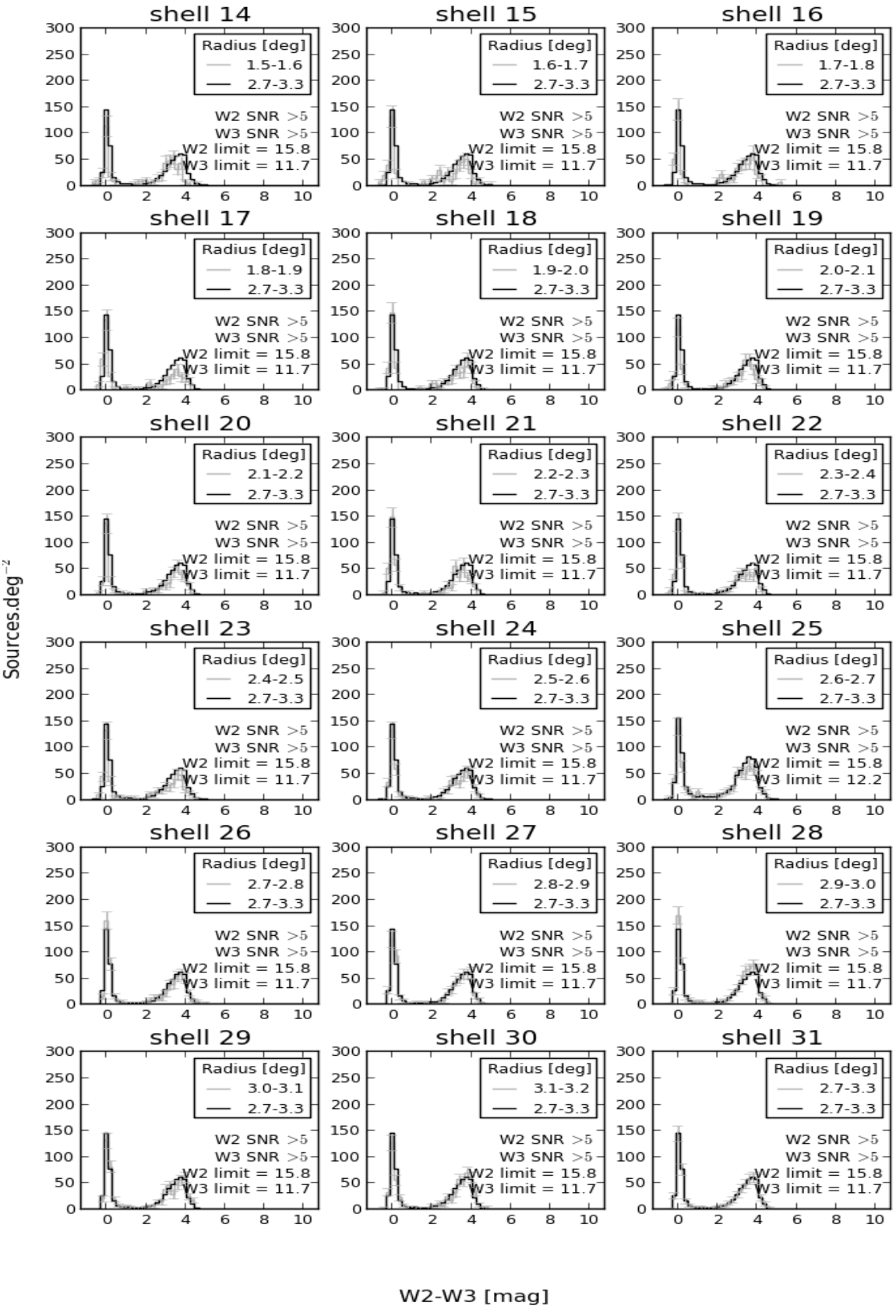

Figure A.6: Continued

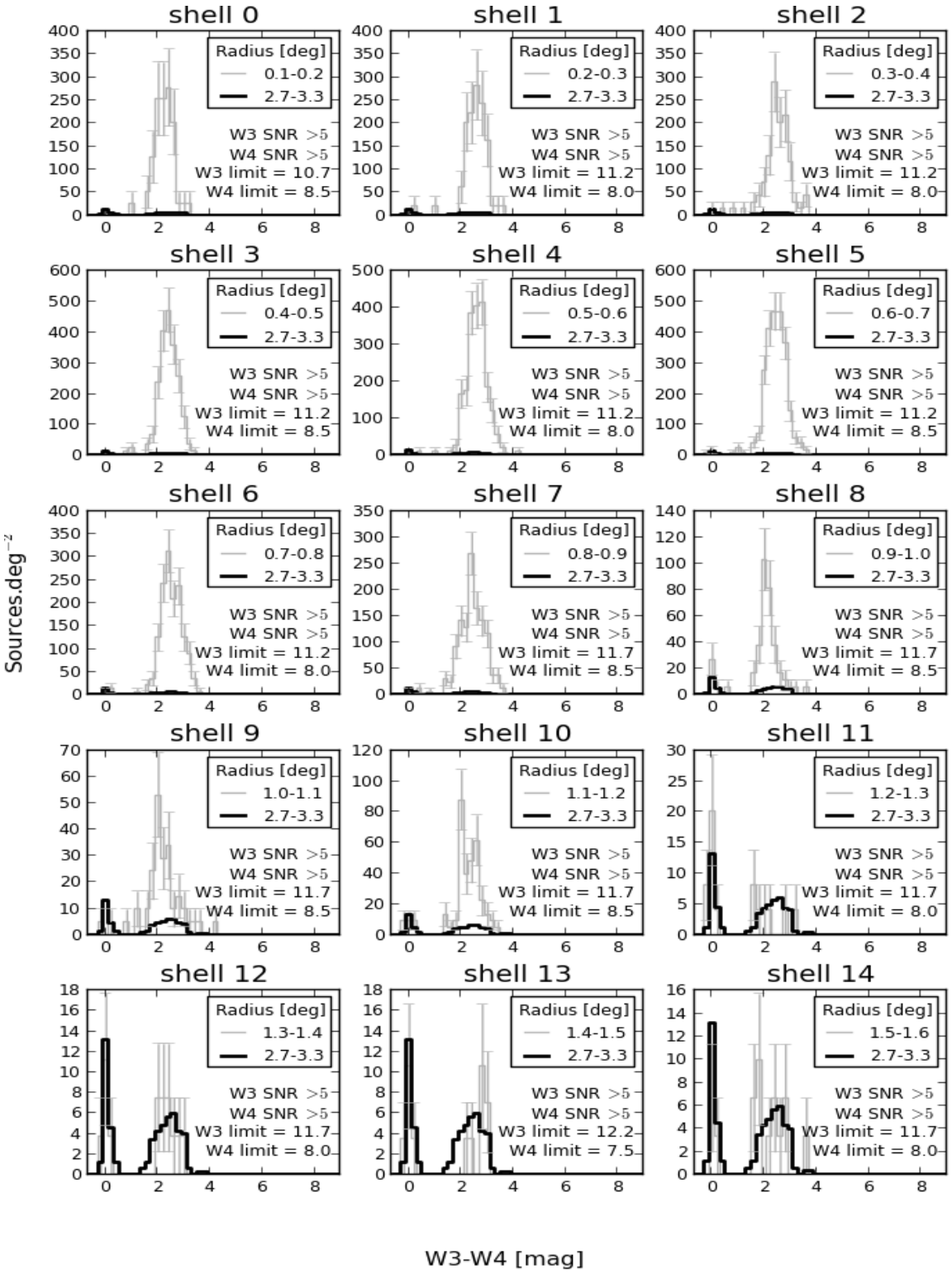

Figure A.7: W3-W4 color histograms for the different shells.

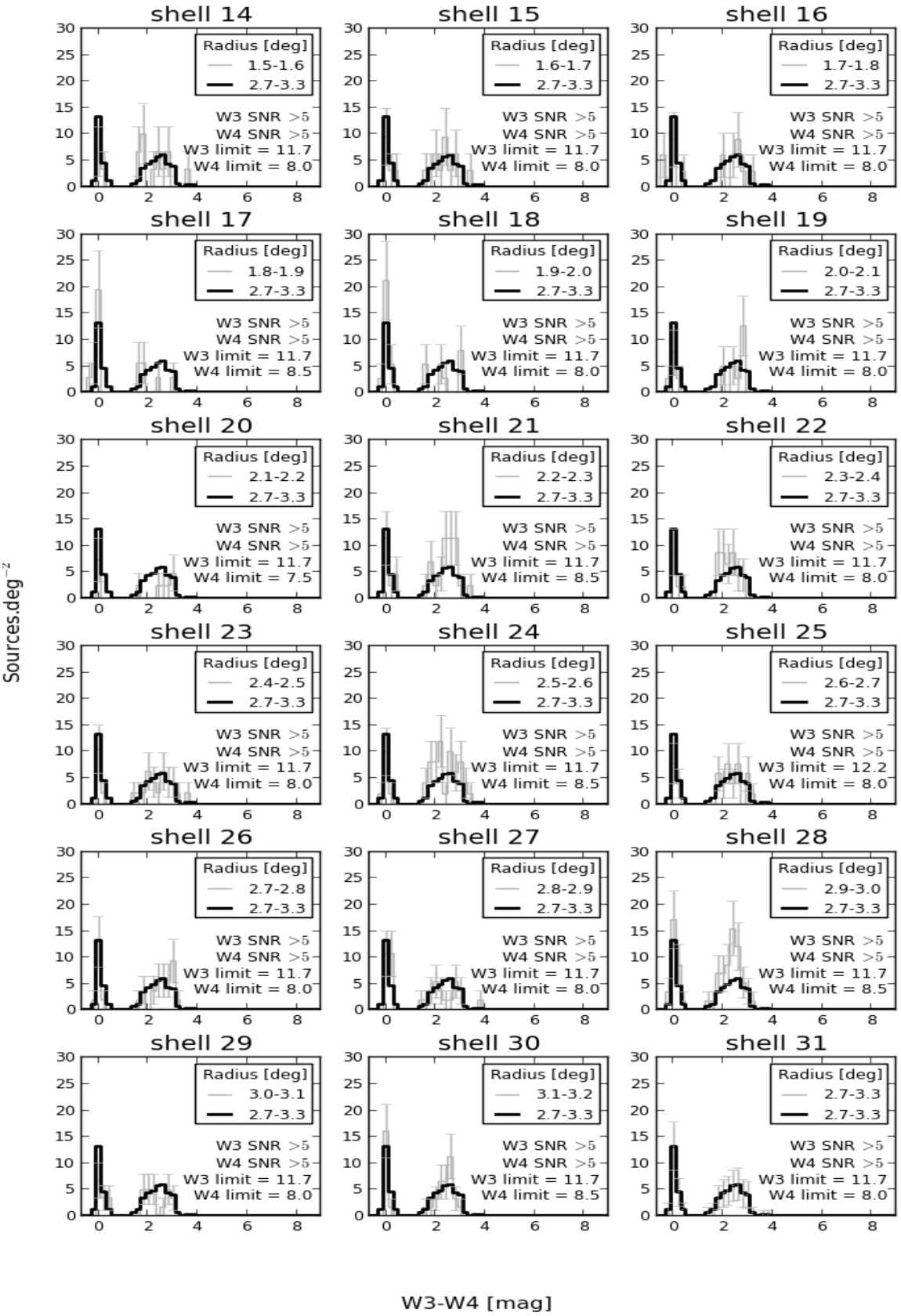

Figure A.7: Continued

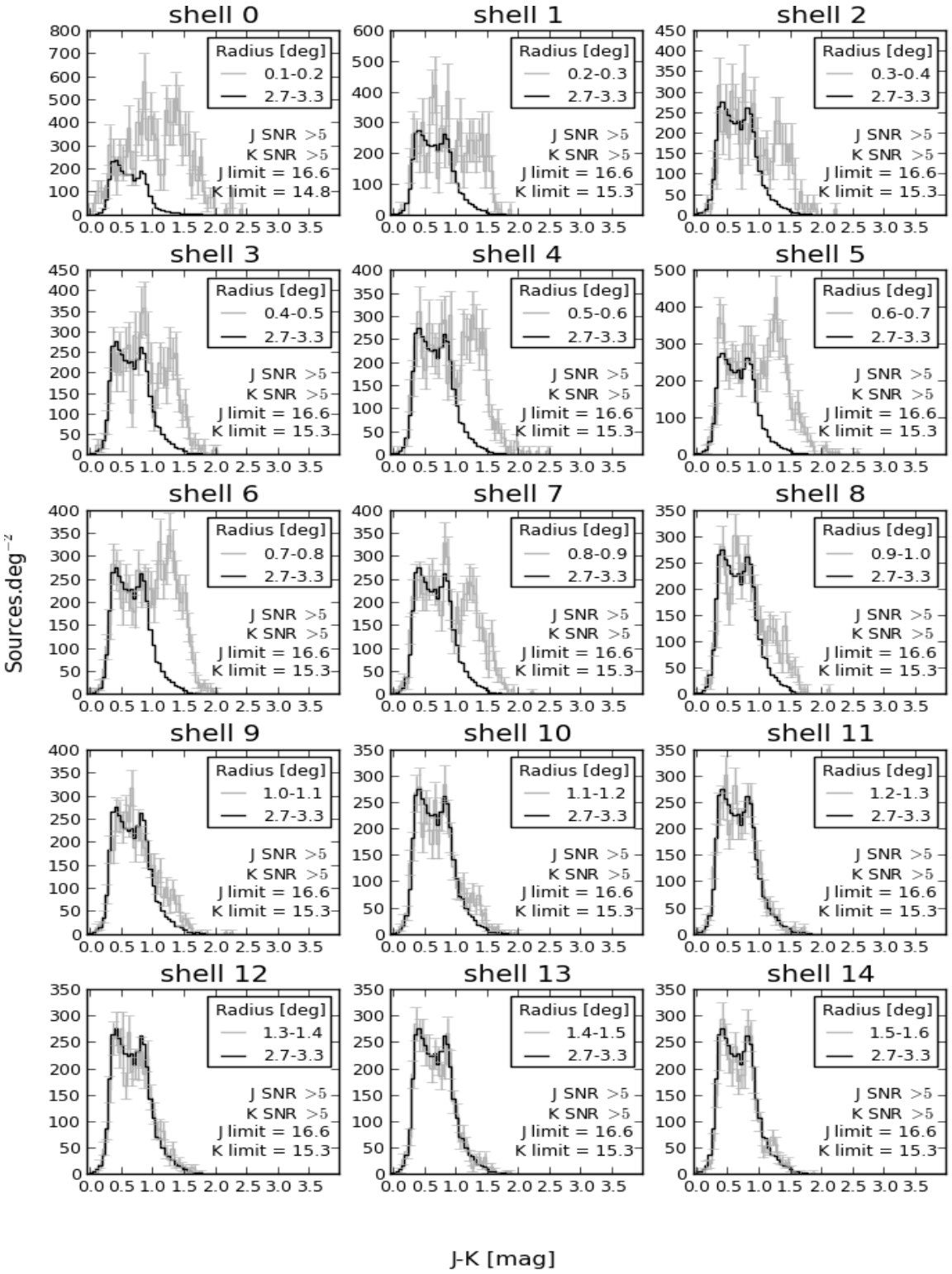

Figure A.8: J-K$_s$ color histograms for the different shells.

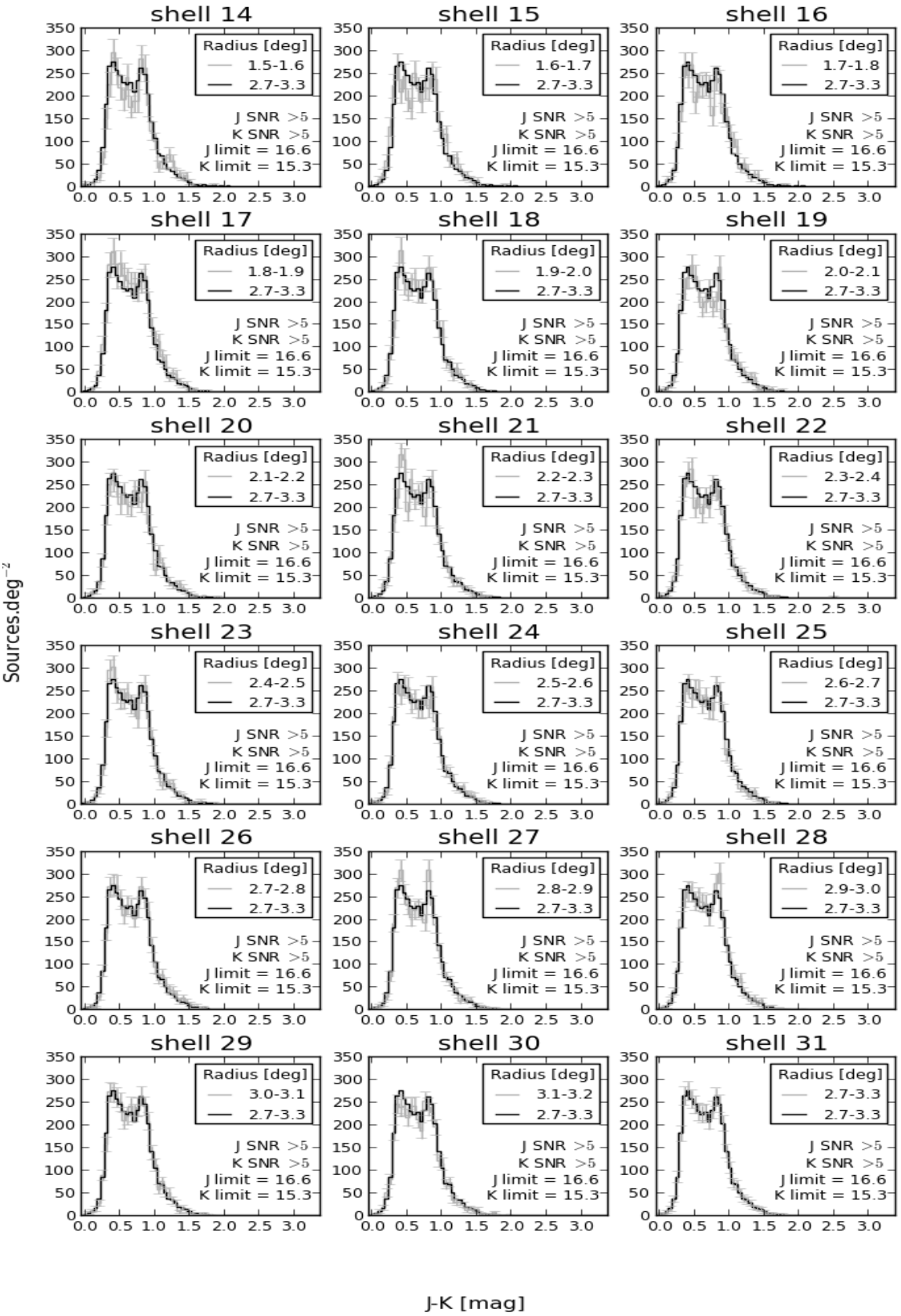

Figure A.8: Continued

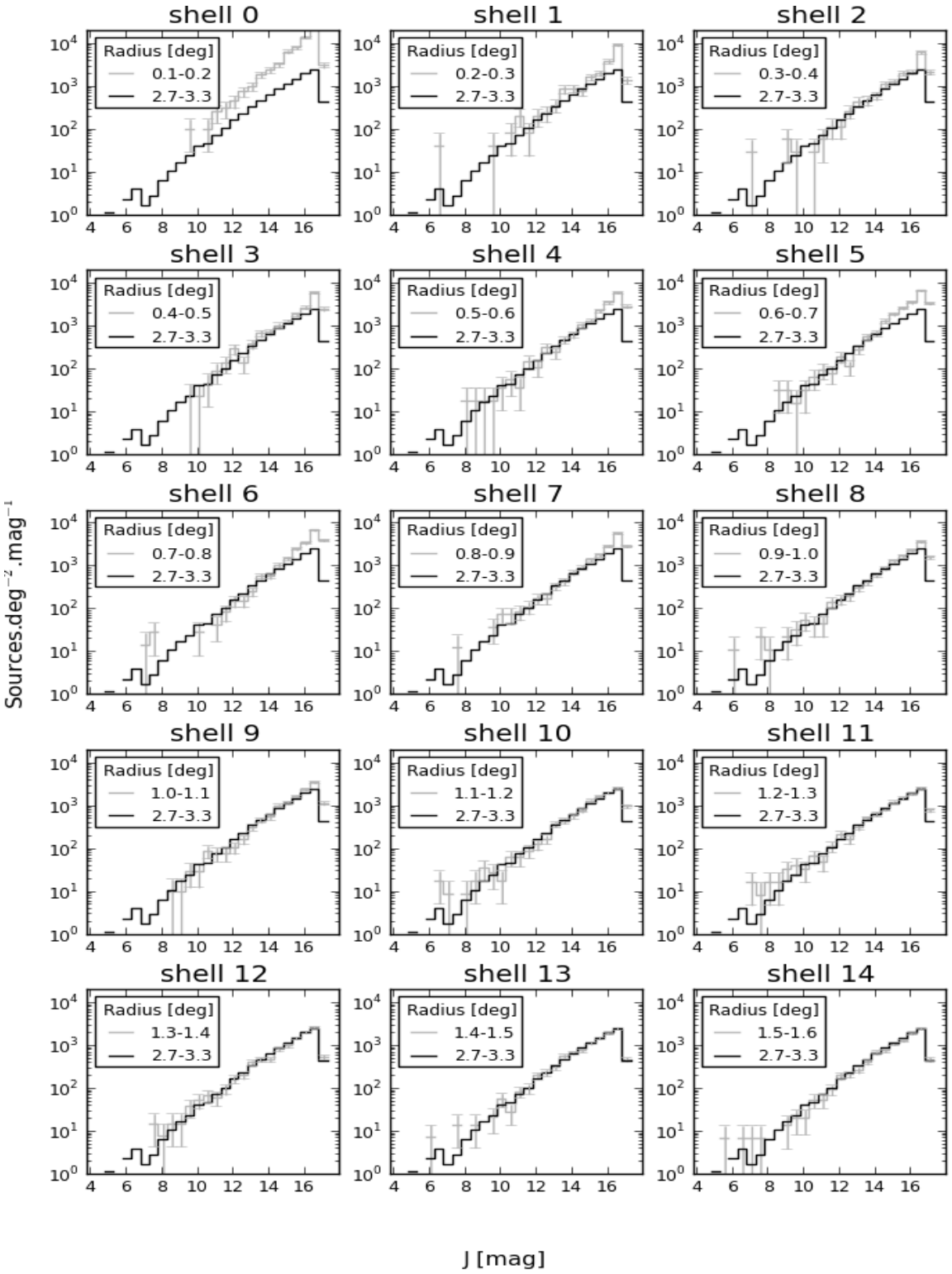

Figure A.9: 2MASS J source number density for the different shells.

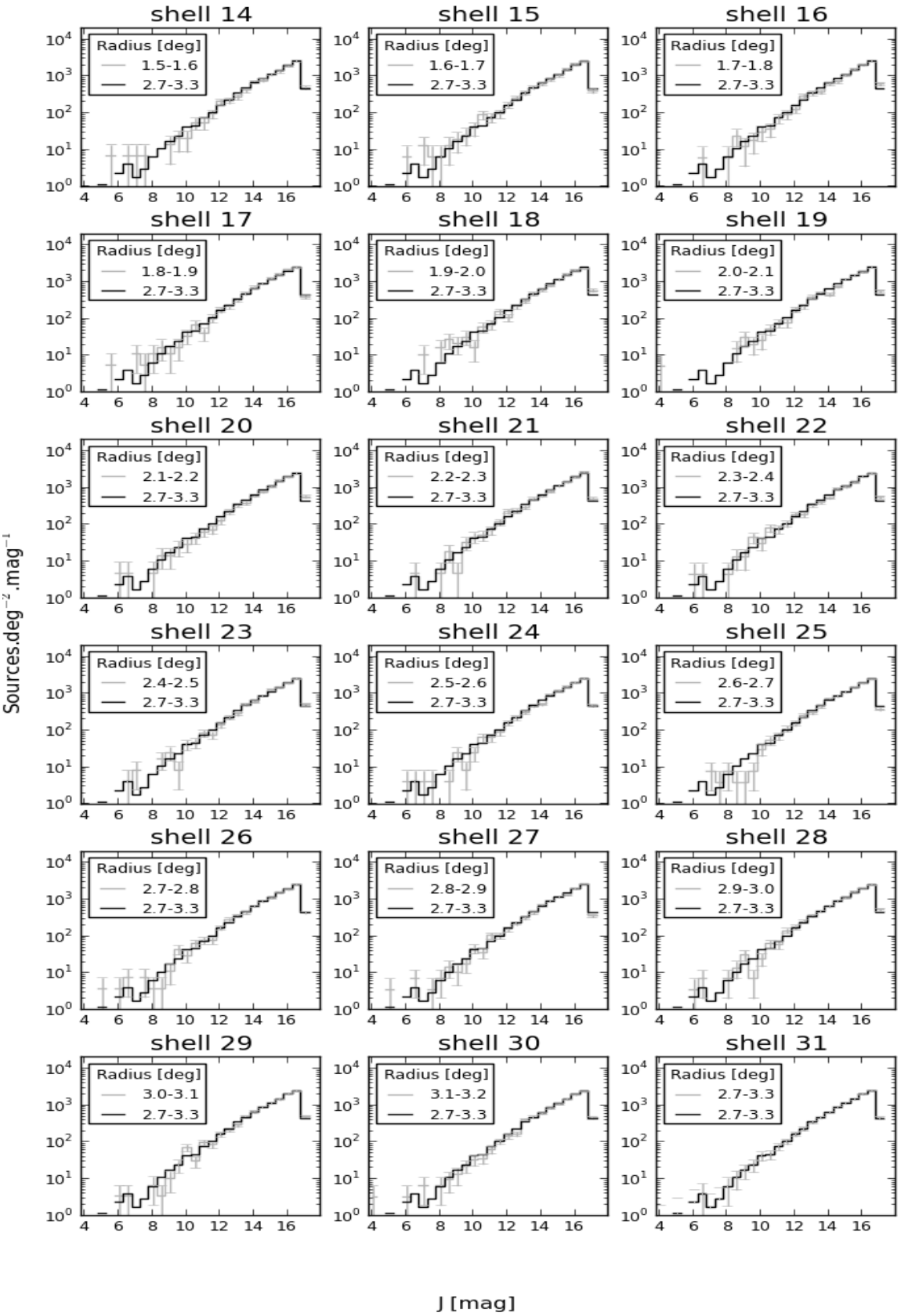

Figure A.9: Continued

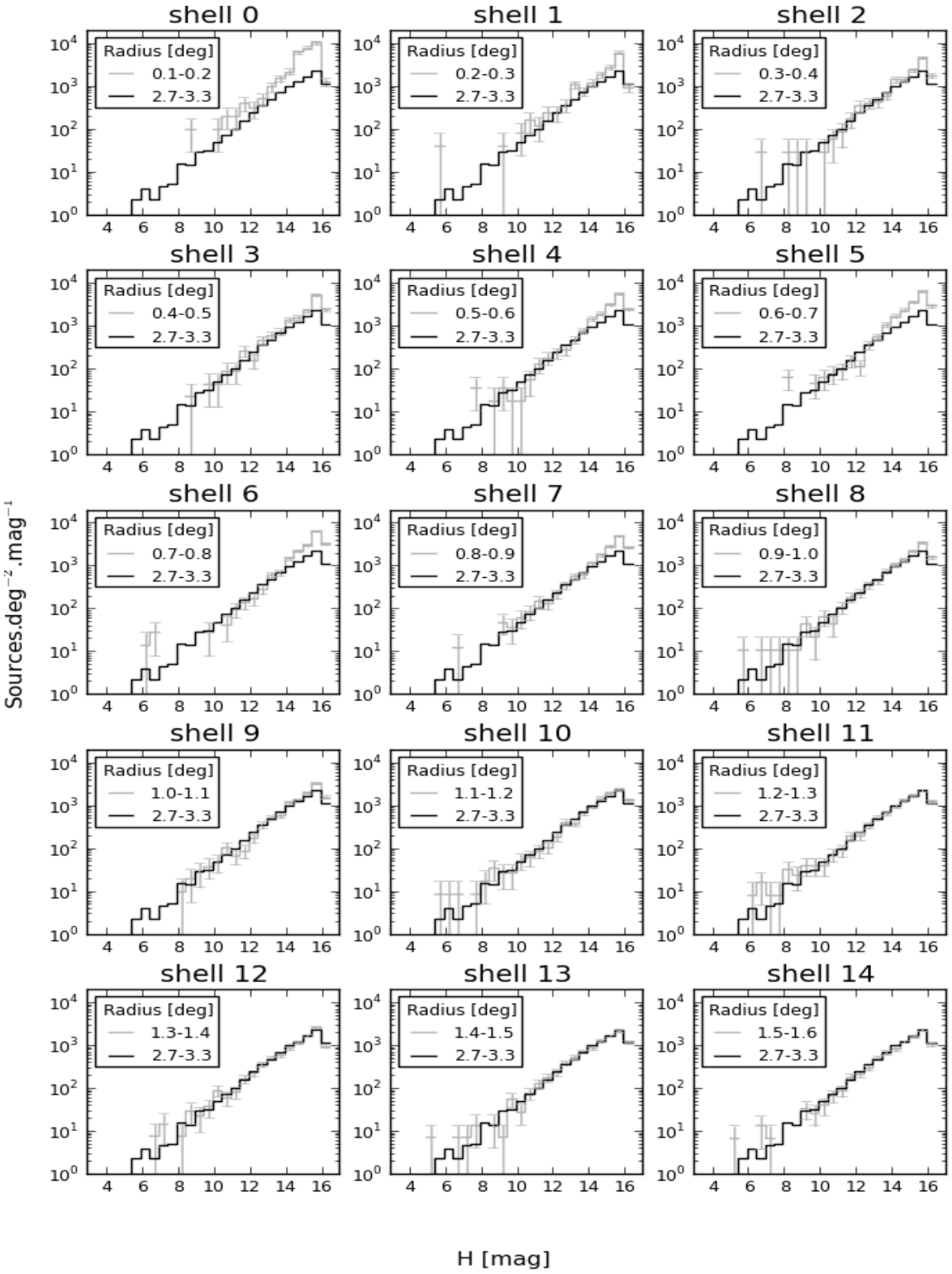

Figure A.10: 2MASS H source number density for the different shells.

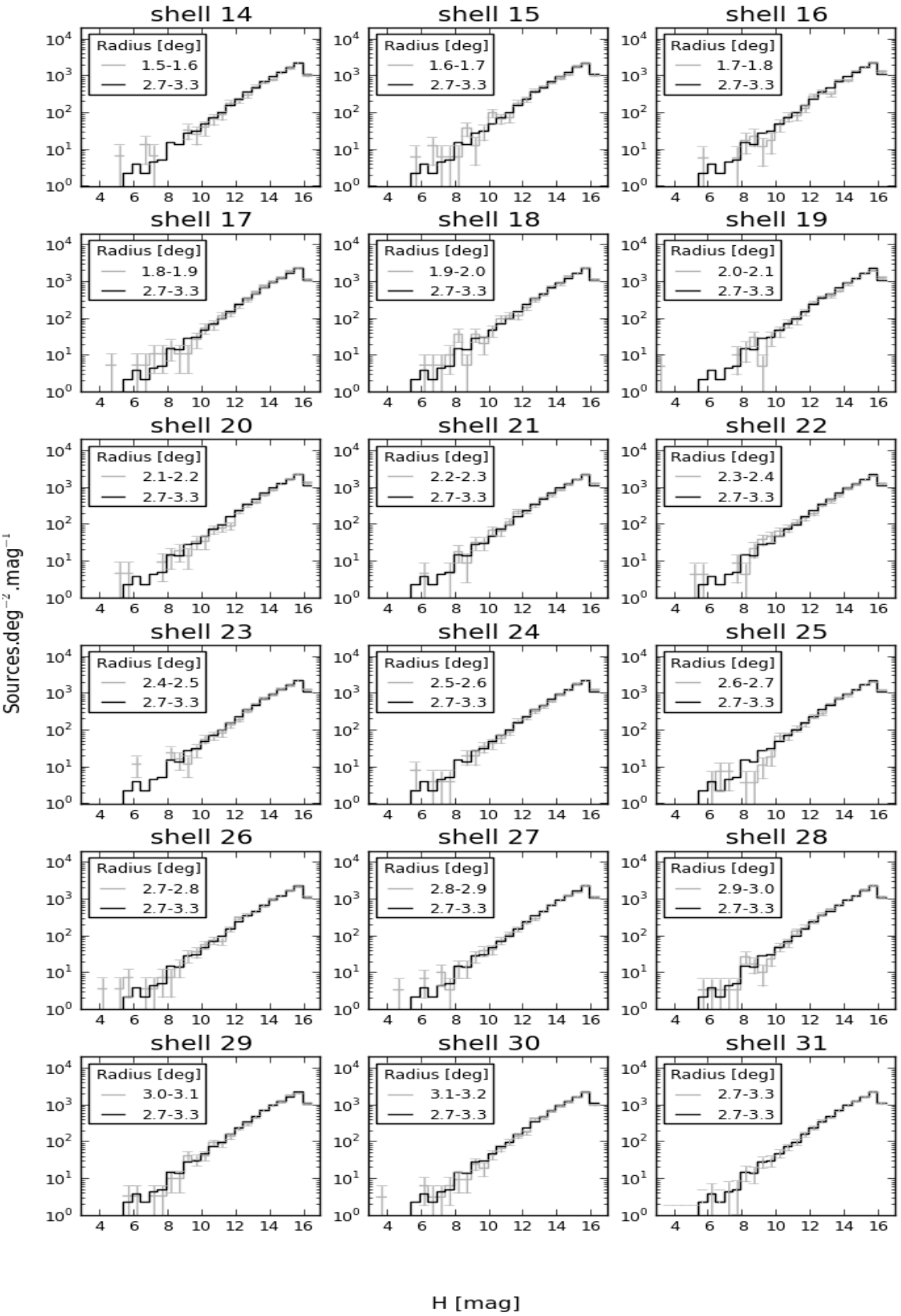

Figure A.10: Continued

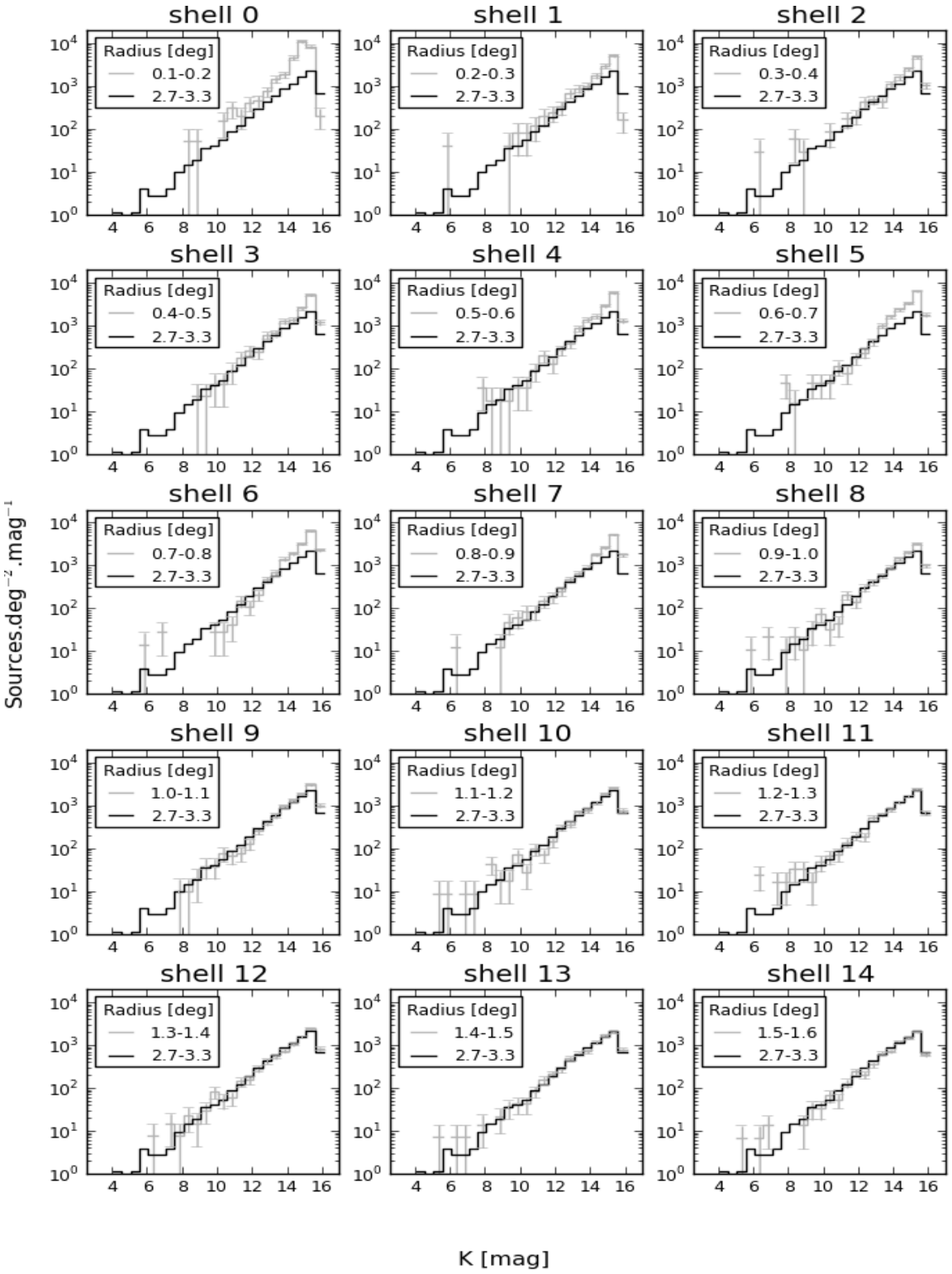

Figure A.11: 2MASS K_s source number density for the different shells.

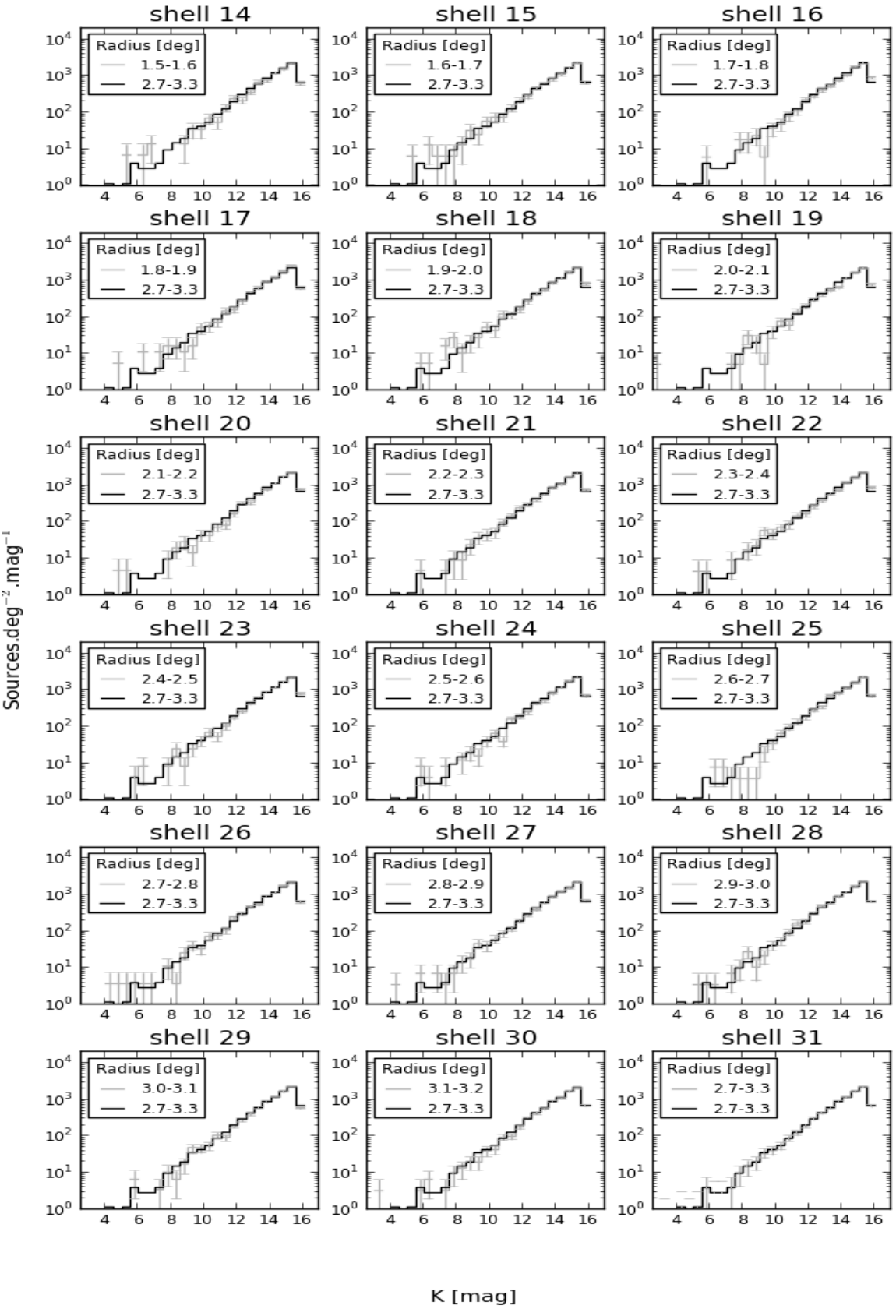

Figure A.11: Continued

Bibliography

Ashman, K.M., Zepf, S.E., The Observatory, 118, 387

Barmby, P., Ashby , M.L.N., Bianchi, L., Engelbracht, C.W., Gehrz, R.D., Gordon, K.D., Hinz, J.L., Huchra, J.P., Humphreys, R.M., Pahre, M.A., Perez-Gonzalez, P.G., Polomski, E.F., Rieke, G.H., Thilker, D.A., Willner, S.P., Woodward, C.E., 2006, ApJ, 650, L45

Barmby, P., Huchry, J., 2001, AJ, 122, 2458

Barmby, P., Huchra, J.P., Brodie, J.P., Forbes, D.A., Schroder, L.L., Grillmair, C.J., 2000, AJ, 119, 727

Barmby, P., Jalilian, F.F.., 2012, AJ, 143, 87

Bell, E.F., Slater, C.T., Martin, N.F., 2011, ApJ, 742, L15

Block, D.L., Combes, F., Puerari, I., Freeman, K.C., Stockton, A., Canalizo, G., Jarrett, T.H., Groess, R., Worthey, G., Gehrz, R.D., Woodward, C.E., Polomski, E.F., Fazio, G.G., 2008, A&A, aa5908

Block, D.L., Freeman, K.C., Jarrett, T.H., Puerari, I., Worthey, G., Combes, F., Groess, R., 2004, A&A, 425, L37

Block, K.M., 2011, Fulgurite classification, petrology, and implications for planetary processes, AAT 1494536, Available from: ProQuest Dissertations and Theses.

Brown, M.J.I., Moustakas, J., Smith, J.D.T., da Cunha, Elisabete, Jarrett, T.H., Imanishi, M., Armus, L., Brandl, B.R., Peek, J.E.G., 2013, Manuscript submitted for publication to AJS

Buat, V., Boissier, S., Burgarella, D., Takeuchi, T.T., Le Floc′h, E., Marcillac, D., Huang, J., Nagashima, M., Enoki, M., 2008, A&A, 483, 107

Buat, V., Giovannoli, E., Heinis, S., 2011, A&A, 529, A22

Chapman, S.C., Ibata, R., Lewis, G.F., Ferguson, A.M.N., Irwin, M., McConnachie, A., Tanvir, N., 2006, ApJ, 653, 255

Chemin, L., Carignan, C., Foster, T., 2009, AJ, 705,1395-1415

Cluver, M.E., Jarrett, T.H., Hopkins, A.M., Driver, S.P., Liske, J., Gunawardhana, M.L.P., Taylor, E.N., Robotham, A.S.G., Alpaslan, M., Baldry, I., Brown, M.J.I., Peacock, J.A., Popescu, C.C., Tuffs, R.J., Bauer, A.E., Bland-Hawthorn, J., Colless, M., Holwerda, B.W., Lara-López, M.A., Leschinski, K., López-Sánchez, A.R., Norberg, P., Owers, M.S., Wang, L., Wilkins, S.M., 2014, ApJ, 782, 90

Conn, A.R., Ibata, R.A., Lewis, G.F., Parker, Q.A., Zucker, D.B., Martin, N.F., McConnachie, A.W., Irwin, M.J., Tanvir, N., Fardal, M.A., Ferguson, A.M.N., Chapman, S.C., Valls-Gabaud, D., 2012, ApJ, 758, 11

Conn, A.R., Lewis, G.F., Ibata, R.A., Parker, Q.A., Zucker, D.B., McConnachie, A.W., Martin, N.F., Valls-Gabaud, D., Tanvir, N., Irwin, M.J., Ferguson, A.M.N., Chapman, S.C., 2013, ApJ, 766, 120

Corbelli, E., 2003, MNRAS, 342, 199

Crampton, D., Cowley, A.P., Schade, D., Chayer, P., 1985, ApJ, 288, 494

Cutri, R.M., Wright, E.L., Conrow, T., Bauer, J., Benford, D., Brandenburg, H., Dailey, J., Eisenhardt, P.R. M., Evans, T., Fajardo-Acosta, S., Fowler, J., Gelino, C., Grillmair, C., Harbut, M., Homan, D., Jarrett, T.H., Kirkpatrick, J.D., Leisawitz, D., Liu, W., Mainzer, A., Marsh, K., Masci, F., McCallon, H., Padgett, D., Ressler, M. E., Royer, D., Skrutskie, M.F., Stanford, S.A., Wyatt, P.L., Tholen, D., Tsai, C.W., Wachter, S., Wheelock, S.L., Yan, L., Alles, R., Beck, R., Grav, T., Masiero, J., McCollum, B., McGehee, P., Papin, M., Wittman, M., 2012, Explanatory Supplement to the WISE All-Sky Data Release Products, Tech. rep.

de Vaucouleurs, G., 1959, ApJ, 130, 728

Di Stefano, R., Kong, A.K.H., Garcia, M.R., Barmby, P., Greiner, J., Murray, S.S., Primini, F.A., 2002, ApJ, 570, 618

Draine, B.T., Dale, D.A., Bendo, G., Gordon, K.D., Smith, J.D.T., Armus, L., Engelbracht, C.W., Helou, G., Kennicutt, R.C., Jr., Li, A., Roussel, H., Walter, F., Calzetti, D., Moustakas, J., Murphy, E.J., Rieke, G.H., Bot, C., Hollenbach, D.J., Sheth, K., Teplitz, H.I., 2007, 663, 866

Elbaz, D., Daddi, E., Le Borgne, D., Dickinson, M., Alexander, D.M., Chary, R.R., Starck, J.L., Brandt, W.N., Kitzbichler, M., MacDonald, E., Nonino, M., Popesso, P., Stern, D., Vanzella, E., 2007, A%A, 468, 33

Evans, I.N., Primini, F.A., Glotfelty, K.J., Anderson, C.S., Bonaventura, N.R., Chen, J.C., Davis, J.E., Doe, S.M., Evans, J.D., Fabbiano, G., Galle, E.C., Gibbs, D.G., II, Grier, J.D., Hain, R.M., Hall, D.M., Harbo, P.N., Xiangqun H.H., Houck, J.C., Karovska, M., Kashyap, V.L., Lauer, J., McCollough, M.L., McDowell, J.C., Miller, J.B., Mitschang, A.W., Morgan, D.L., Mossman, A.E., Nichols, J.S., Nowak, M.A., Plummer, D.A., Refsdal, B.L., Rots, A.H., Siemiginowska, A., Sundheim, B.A., Tibbetts, M.S., Van Stone, D.W., Winkelman, S.L., Zografou, P., 2010, ApJS, 189, 37

Ford, G.P., Gear, W.K., Smith, M.W.L., Eales, S.A., Baes, M., Bendo, G.J., Boquien, M., Boselli, A., Cooray, A.R., De Looze, I., Fritz, J., Gentile, G., Gomez, H.L., Gordon, K.D., Kirk, J., Lebouteiller, V., O′Halloran, B., Spinoglio, L., Verstappen, J., Wilson, C.D., 2013, ApJ, 769, 55

Fritz, J., Gentile, G., Smith, M.W.L., Gear, W.K., Braun, R., Duval, J.R., Bendo, G.J., Baes, M., Eales, S.A., Verstappen, J., Blommaert, J.A.D.L., Boquien, M., Boselli, A., Clements, D., Cooray, A.R., Cortese, L., De Looze, I., Ford, G.P., Galliano, F., Gomez, H.L., Gordon, K.D., Lebouteiller, V., OHalloran, B., Kirk, J., Madden, S.C., Page, M.J., Remy, A., Roussel, H., Spinoglio, L., Thilker, D., Vaccari, M., Wilson, C.D., Waelkens, C., 2012, A&A, 546, A34

Fuchs, B., Jahreib, H., Flynn, C., 2009, AJ, 137, 226

Galleti, S., Bellazzini, M., Buzzoni, A., Federici, L., Fusi Pecci, F., 2009, A&A, 508, 1285-1299

Galleti, S., Federici, L., Bellazzini, M., Fusi Pecci, F., Macrina, S., 2004, A&A, 416, 917-924 (G04)

Gil de Paz, A., Boissier, S., Madore, B.F., Seibert, M., Joe, Y.H., Boselli, A., Wyder, T.K., Thilker, D., Bianchi, L., Rey, S., Rich, R.M., Barlow, T.A., Conrow, T., Forster, K., Friedman, P.G., Martin, D.C, Morrissey, P., Neff, S.G., Schiminovich, D., Small, T., Donas, J., Heckman, T.M., Lee, Y., Milliard, B., Szalay, A.S., Yi, S., 2007, ApJS, 173, 185

Gordon, K. D., Bailin, J., Engelbracht , C. W., Rieke, G. H., Misselt, K. A., Latter, W. B., Young, E. T., Ashby, M. L. N., Barmby, P., Gibson, B. K., Hines, D. C., Hinz, J., Krause, O., Levine, D. A., Marleau, F. R., Noriega-Crespo, A., Stolovy, S., Thilker, D.A., Werner, M. W., 2006, AJ, 638, L87

Gottesman, S.T., Hunter, J.H., Boonyasait, V., 2002, MNRAS, 337, 34

Hammer, F., Puech, M., Chemin, L., Flores, H., Lehnert, M. D., 2007, ApJ, 662, 322

Hubble, E.P., 1932, ApJ, 76, 44

Ibata, R., Chapman, S., Ferguson, A.M.N., Irwin, M., Lewis, G., McConnachie, A., 2004, MNRAS, 351, 117

Jarrett, T. H., Chester, T., Cutri, R., Schneider, S., Huchra, J. 2003, AJ, 125, 525

Jarrett, T.H., Cohen, M., Masci, F., Wright, E., Stern, D., Benford, D., Blain, A., Carey, S., Cutri, R.M., Eisenhardt, P., Lonsdale, C., Mainzer, A., Marsh, K., Padgett, D., Petty, S., Ressler, M., Skrutskie, M., Stanford, S., Surace, J., Tsai, C. W., Wheelock, S., Yan, D. L., 2011, ApJ, 735, 112

Jarrett, T.H., Masci, F., Tsai, C.W., Petty, S., Cluver, M., Assef, R.J., Benford, D., Blain, A., Bridge, C., Donoso, E., Eisenhardt, P., Koribalski, B., Lake, S., Neill, James D., Seibert, M., Sheth, K., Stanford, S., Wright, E., 2012, AJ, 144, 68 (Paper I)

Jarrett, T.H., Masci, F., Tsai, C.W., Petty, S., Cluver, M., Assef, R.J., Benford, D., Blain, A., Bridge, C., Donoso, E., Eisenhardt, P., Koribalski, B., Lake, S., Neill, James D., Seibert, M., Sheth, K., Stanford, S., Wright, E., 2013, AJ, 145, 6 (Paper II)

Kang, Y., Bianchi, L., Rey, S., 2009, ApJ, 703, 614

Mandushev, G., Staneva, A., Spasova, N., 1991, A&A, 252, 94

Marleau, F.R., Noriega-Crespo, A., Misselt, K.A., Gordon, K.D., Engelbracht, C.W., Rieke, G.H., Barmby, P., Willner, S.P., Mould, J., Gehrz, R.D., Woodward, C.E., 2006, ApJ, 646, 929

Masci, F., astro-ph/1301.2718

Massey, P., McNeill, R.T., Olsen, K.A.G., Hodge, P.W., Blaha, C., Jacoby, G.H., Smith, R.C., Strong, S.B., 2007, AJ, 134, 2474

McConnachie, A. W., Irwin, M. J., 2006, MNRAS, 365, 902

McConnachie, A.W., Irwin, M.J., Ibata, R.A., Dubinski, J., Widrow, L.M., Martin, N.F., Côté, Patrick, D., Aaron L., Navarro, J.F., Ferguson, A.M.N., Puzia, T.H., Lewis, G.F., Babul, A., Barmby, P., Bienaymé, O., Chapman, S.C., Cockcroft, R., Collins, M.L.M., Fardal, M.A., Harris, W.E., Huxor, A., Mackey, A.D., Peñarrubia, J., Rich, R.M, Richer, H.B., Siebert, A., Tanvir, N., Valls-Gabaud, D., Venn, K.A., 2009, Nature, 461, 66

Montalto, M., Seitz, S., Riffeser, A., Hopp, U., Lee, C.H., Schonrich, R., 2009, A&A, 507, 283-300

Pietsch, W., Fliri, J., Freyberg, M.J., Greiner, J., Haberl, F., Riffeser, A., Sala, G., 2005, A&A, 442, 879

Regan, M.W., Vogel, S.N., 1994, ApJ, 434, 536

Revnivtsev, M.G., Sunyaev, R. A., Krivonos, R.A., Tsygankov, S.S., Molkov, S.V., 2014, AL, 40, 22

Rice, W., Lonsdale, C. J., Soifer, B. T., Neugebauer, G., Kopan, E. L., Lloyd, L. A., 1988, AJ, 68, 91-127

Richardson, J.C., Irwin, M.J., McConnachie, A.W., Martin, N.F., Dotter, A.L., Ferguson, A.M.N., Ibata, R.A., Chapman, S.C., Lewis, G.F., Tanvir, N.R., Rich, R.M., 2011, ApJ, 732, 76

Rieke, G.H., Alonso-Herrero, A., Weiner, B.J., Pérez-González, P.G., Blaylock, M., Donley, J.L., Marcillac, D., 2009, ApJ, 692, 556

Sargent, W.L.W., Kowal, C.T., Hartwick, F.D.A., van den Bergh, S., AJ, 82, 947

Schiminovich, D., Wyder, T.K., Martin, D.C., Johnson, B.D., Salim, S., Seibert, M., Treyer, M.A., Budavári, T., Hoopes, C., Zamojski, M., Barlow, T.A., Forster, K.G., Friedman, P.G., Morrissey, P., Neff, S.G., Small, T.A., Bianchi, L., Donas, J., Heckman, T.M., Lee, Y., Madore, B.F., Milliard, B., Rich, R.M., Szalay, A.S., Welsh, B.Y., Yi, S., 2007, ApJS, 173, 315

Sérsic, J.L., 1963, AAA, 6, 41

Silva, L., Schurer, A., Granato, G.L., Almeida, C., Baugh, C.M., Frenk, C.S., Lacey, C.G., Paoletti, L., Petrella, A., Selvestrel, D., 2011, MNRAS, 410, 2043

Slater, C.T., Bell, E.F., Martin, N.F., 2011, ApJ, 742, L14

Stiele, H., Pietsch, W., Haberl, F., Hatzidimitriou, D., Barnard, R., Williams, B.F., Kong, A.K.H., Kolb, U., 2011, A&A, A55

Tempel, E., Tamm, A., Tenjes, P., 2010, A&A, 509, A91

Tully, R.B., Rizzi, L., Shaya, E.J., Courtois, H.M., Makarov, D.I., Jacobs, B.A, 2009, AJ, 138, 323

van den Bergh, S., 2006, AJ, 132, 1571-1574

Viaene, S., Fritz, J., Baes, M., Bendo, G.J., Blommaert, J.A.D. L., Boquien, M., Boselli, A., Ciesla, L., Cortese, L., De Looze, I., Gear, W.K., Gentile, G., Hughes, T.M., Jarrett, T.H, Karczewski, O.Ł., Smith, M.W.L., Spinoglio, L., Tamm, A., Tempel, E., Thilker, D., Verstappen, J., 2014, A&A

Walterbos, R.A.M., Kennicutt, R.C., Jr., 1987, A&AS, 69, 311

Wright, E.L., Eisenhardt, P.R.M., Mainzer, A.K., Ressler, M.E., Cutri, R.M., Jarrett, T., Kirkpatrick, J.D., Padgett, D., McMillan, R.S., Skrutskie, M., Stanford, S.A., Cohen,

M., Walker, R.G., Mather, J.C., Leisawitz, D., Gautier, T.N., III, McLean, I., Benford, D., Lonsdale, C.J., Blain, A., Mendez, B., Irace, W.R., Duval, V., Liu, F., Royer, D., Heinrichsen, I., Howard, J., Shannon, M., Kendall, M., Walsh, A.L., Larsen, M., Cardon, J.G., Schick, S., Schwalm, M., Abid, M., Fabinsky, B., Naes, L., Tsai, C., AJ, 140, 1868

Wu, H., Cao, C., Hao, C., Liu, F., Wang, J., Xia, X., Deng, Z., Young, C.K., 2005, ApJ, 632, L79